Modeling the Prussian blue analogs from first principles for battery applications

Kevin Hurlbutt

St. Anne's College

University of Oxford

A thesis submitted for the degree of

Doctor of Philosophy

Trinity 2021

Acknowledgements

I gratefully acknowledge the high-performance computing resources afforded by ARCUS at Oxford; the UK's ARCHER cluster; and Beskow at KTH University in Sweden. I also thank the Partnership for Advanced Computing in Europe (PRACE) for awarding my proposals for some of the resources on those clusters.

I would like to thank my supervisors for all their teaching. Mauro Pasta's guidance on identifying important problems is as valuable as any science I have learned. Feliciano Giustino's insight into the details of electronic-structure theory is the only reason this work is robust. And George Volonakis was infinitely generous in teaching me my pseudopotentials from my functionals.

I would also like to thank Chris Grovenor at St. Anne's for the opportunity and support to tutor for the college. It has been one of the most rewarding parts of my degree. And, also, I thank my students for always challenging me to think clearly enough to explain well.

I am deeply indebted to my labmates Jack Fawdon, Sam Wheeler, Isaac Capone, Albert Xiao, Max Schart, and Michele Fiore. Their ideas, conversations, and assistance have been, at various times, the seeds, trunk, and flowers of the ideas in this work.

I am very grateful to my friends in Oxford who have made living and studying here as fun as it has been instructive. Jasper, Nicole, Joe, Giuliana, and Jack have all been unbelievably supportive of my throughout this doctorate.

This research was possible only because of my family's loving support. I thank them for everything they have done for me. And to my parents, Mo and Tom, in particular - this simply would not have happened without them.

Finally, I am beyond grateful to my partner, Elena. She is, by far, the most important and interesting future project.

Abstract

The Prussian blue analogs (PBAs) are a family of electrochemically reactive compounds with great promise as electrode materials in next-generation sodium- and potassium-ion batteries. They are also an excellent platform for the computational study of interesting phenomena within electronic-structure theory, including mixed valency, redox activity, photo-induced spin transition, and charge disproportionation. However, modeling the PBAs with density-functional theory (DFT) is difficult because the electrons in these compounds are strongly correlated. In this work, I demonstrate how important electrochemical properties of the PBAs are calculable from first principles, but advanced, DFT-based methods like non-local, hybrid functionals or DFT+U must be used to overcome the self-interaction error in these strongly correlated systems.

With these advanced, DFT-based methods, I am able to show with a hybrid functional that three metal hexacyanoferrates ($Na_xM[Fe(CN)_6]$), which are important cathode candidates, have very heavy effective masses for charge-carrying electrons and holes, and, thus, small-polaron hopping is an important mechanism for PBA electronic conductivity. Also with the use of a hybrid functional, I provide strong theoretical support to the hypothesis that the high specific capacity of sodium manganese hexacyanomanganate arises from the insertion of a third sodium ion per formula unit to form $Na_3Mn^{II}[Mn^{I}(CN)_6]$, answering a long-standing question from experiment. Finally, I use DFT+U to predict materials properties like reduction potential, ion-hopping activation energy, direct magnetic exchange-coupling coefficient, and infrared-spectroscopy absorption frequencies in four defect-free alkali-metal chromium hexacyanochromates, $A_xCr[Cr(CN)_6]$.

This work provides critical, new insight into the electronic structure and electrochemical properties of the PBAs. Technically, it contributes another example system

to the list of strongly correlated systems successfully simulated with hybrid functionals and DFT+U. And it is an important work in the ongoing, urgent, and global effort to make next-generation batteries better.

Contents

Publication list

Some of the work present here has contributed to items 1, 2, 4, 8, and 9 from the following list of scientific manuscripts. Item 2 is currently under peer review and item 1 is being prepared for submission for peer review.

1. **K. Hurlbutt**, S. Wheeler, M. Schart, and M. Pasta, "Electrochemical and magnetic properties of chromium hexacyanochromate: a high-capacity anode and room-temperature molecular magnet," *in preparation*

2. **K. Hurlbutt**, F. Giustino, G. Volonakis, and M. Pasta, "Origin of the high specific capacity in sodium manganese hexacyanomanganate," *under review*

3. P. Tang, H.J. Lee, **K. Hurlbutt**, P.Y. Huang, S. Narayanan, C. Wang, D. Gianolio, R. Arrigo, J. Chen, J. Warner, and M. Pasta, "Elucidating the formation and structural evolution of platinum single-site catalysts for hydrogen evolution reaction" *under review* preprint available at DOI: 10.33774/chemrxiv-2021-pmcfv

4. **K. Hurlbutt**, F. Giustino, M. Pasta, and G. Volonakis, "Electronic structure and electron-transport properties of three metal hexacyanoferrates," *Chemistry of Materials*, vol. 33, no.17, pp. 7067-7074, 2021.

5. M. Fiore, S. Wheeler, **K. Hurlbutt**, I. Capone, J. Fawdon, R. Ruffo, and M. Pasta, "Paving the way toward highly efficient, high-energy potassium-ion batteries with ionic liquid electrolytes," *Chemistry of Materials*, vol. 32, no. 18, pp. 7653-7661, 2020.

6. J. Cattermull, S. Wheeler, **K. Hurlbutt**, M. Pasta, and A.L. Goodwin, "Filling vacancies in a Prussian blue analogue using mechanochemical post-synthetic modification," *Chemical Communications*, vol. 56, no. 57, pp. 7873-7876, 2020.

7. I. Capone, **K. Hurlbutt**, A.J. Naylor, A.W. Xiao, and M. Pasta, "Effect of the particle-size distribution on the electrochemical performance of a red phosphorus–carbon composite anode for sodium-ion batteries," *Energy and Fuels*, vol. 33, no. 5, pp. 4651-4658, 2019.

8. **K. Hurlbutt**[*], S. Wheeler[*], I. Capone, and M. Pasta, "Prussian blue analogs as battery materials," *Joule*, vol. 2, no. 10, pp. 1950-1960, 2018.

9. S. Wheeler, **K. Hurlbutt**, and M. Pasta, "A new solid-state sodium-metal battery," *Chem*, vol. 4, no. 4 pp. 666-668, 2018.

[*] equal contribution

List of Figures

List of Tables

Chapter 1

Introductions: Prussian blue analogs as battery materials

1.1 Motivation for this work

This work is a first-principles study of the electrochemical properties of the Prussian blue analogs. It is motivated by the global need for better batteries, especially batteries that can insert ions other than lithium, like sodium and potassium. The Prussian blue analogs (PBAs) are excellent candidates for active materials in these next-generation batteries. This is also motivated by the great number of interesting, unanswered questions about the electronic structure of the PBAs. These questions lend themselves well to investigation by ab-initio simulation with density-functional theory (DFT). Figure 1.1 shows the growth in research into this work's three main topics: Prussian blue, density-functional theory, and batteries. Each is more popular than the last, with almost 20,000 scientific papers per year written on batteries in the decade from 2010 to 2020.

This chapter introduces the necessary context for what follows. The first section focuses on the science of electrochemical cells (the individual components of batteries). After that, the PBAs and the tunability of their materials properties are discussed. Finally, the use of DFT is motivated by the presentation of three achievements of the method in the study of batteries.

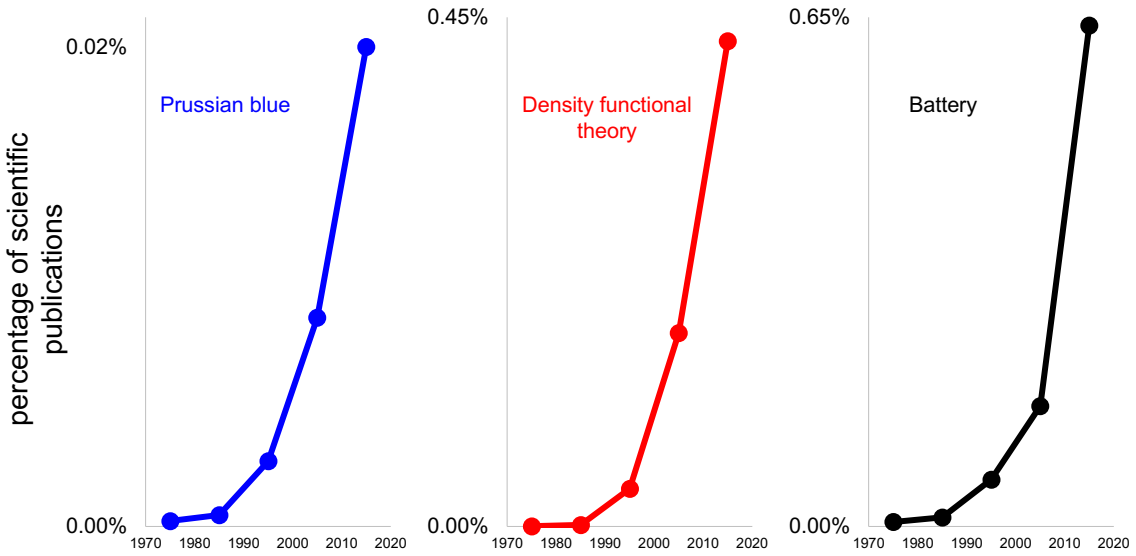

Figure 1.1: Growth in citations over time. The percentage of all scientific publications matching the search terms "Prussian blue" (blue, left), "Density functional theory" (red, middle), and "Battery" (black, right) are plotted versus time over the last 5 decades. Values are taken from a search of the database at webofknowledge.com.

1.2 The physical chemistry of electrochemical cells

This section introduces the physical chemistry of electrochemical cells. First, the thermodynamics of half-reactions are discussed and related to the energy that can be extracted from a battery. Electrode kinetics, including the effects of ionic and electronic conductivities, are then introduced through the Butler–Volmer equation. Finally, transport in the electrolyte phase is briefly discussed.

1.2.1 Thermodynamics and reduction potentials

A battery is a device made of one or more electrochemical cells, each of which converts chemical energy into electrical energy. A battery is based on a electrochemical reaction. One such reaction between the PBA iron hexacyanoferrate, $Fe[Fe(CN)_6]$, and sodium metal is [1]

$$Fe[Fe(CN)_6] + Na \rightarrow NaFe[Fe(CN)_6]. \tag{1.1}$$

The particular electrochemical properties of this and other PBAs are introduced in the following section; at present, it suffices that iron hexacyanoferrate is an electrochemically reactive species. In this reaction, an electron is transferred from the sodium to the iron hexacyanoferrate, so the sodium is said to be oxidized and the iron hexacyanoferrate is reduced. This reaction can be rewritten as two half-reactions [2]

$$\mathrm{Fe^{III}[Fe^{III}(CN)_6]} + \mathrm{e^-} \rightarrow \mathrm{Fe^{III}[Fe^{II}(CN)_6]^-} \tag{1.2}$$

and

$$\mathrm{Na} \rightarrow \mathrm{Na^+} + \mathrm{e^-}. \tag{1.3}$$

The oxidation states of the iron ions have been included explicitly. A battery operates by spatially separating the two half-reactions. During discharge, the reduction half-reaction (equation 1.2) happens at the cathode while the oxidation half-reaction (equation 1.3) happens at the anode. The cathode and anode are known generically as electrodes. At the same time, one or more ionic species cross from one electrode to the other internally through a phase called the electrolyte. In this case, sodium ions move from the anode to the cathode. The electrolyte is often a solution of conductive salts in an aqueous or organic solvent, but the study of solid-state electrolytes is one of the busiest in battery science [3]. Finally, while ions move through the electrolyte, electrons are driven from the anode to the cathode through a circuit external to the battery. These electrons can be harnessed to do useful electrical work. If the reaction is chemically reversible then the battery is called secondary; it can be recharged by inputting energy and driving the electronic circuit (and the electrochemical reaction) in reverse. If the reaction is irreversible the battery is called primary [4].

Chemical thermodynamics bounds the maximum amount of useful energy available from a battery. No more than the Gibbs free energy of reaction, ΔG_{rxn}, can be extracted. In electrochemistry, is it more usual and experimentally simpler to work in terms of the electric potential of the cell, E_{cell} (also called the cell potential). The

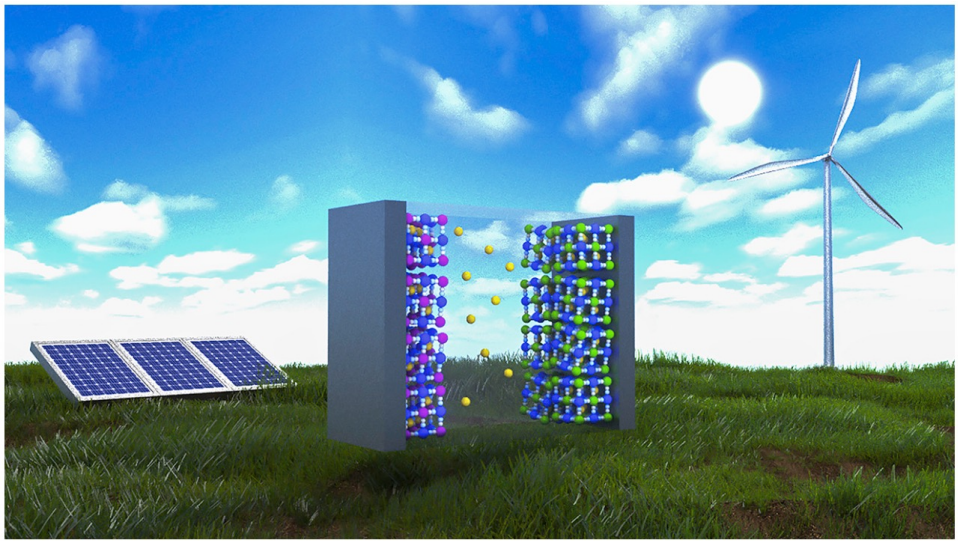

Figure 1.2: A clean energy economy. The work's motivation is shown schematically, highlighting the role of PBA batteries in grid-scale storage of clean energy. Renewable energy sources like solar and wind are needed to reduce greenhouse-gas emissions, and thus to stop further anthropogenic climate change. Solar and wind are intermittent or diurnal, so substantially more electrical-energy storage is required. Batteries based on inexpensive and easily synthesized PBAs could soon be deployed widely in grid-scale storage. Reprinted with permission from [5]. Copyright 2018 Cell Press.

two quantities are related by [6]

$$\Delta G_{\text{rxn}} = -nFE_{\text{cell}} \tag{1.4}$$

in which n is the amount of electrons per ion transferred (that is, the ion's valency) and F is the Faraday constant, $9.6485 \times 10^4\,\text{C}\,\text{mol}^{-1}$. The cell potential can also be written as the difference between the reduction potential of the cathode and the anode as

$$E_{\text{cell}} = E_{\text{cathode}} - E_{\text{anode}}. \tag{1.5}$$

For many electrodes (including iron hexacyanoferrate), the potential is nearly constant over the course of the reaction. However, this is not generally the case. The lithium-ion cathode lithium cobalt oxide (Li_xCoO_2) has a cell potential that is strongly a function of the lithium stoichiometry, x [7]. In these cases, the available

energy when a number of electrons $n(x_2 - x_1)$ is passed between electrodes is

$$\Delta G_{\text{rxn}}(x_1, x_2) = -nF \int_{x_1}^{x_2} dx[E_{\text{cathode}}(x) - E_{\text{anode}}(x)]. \tag{1.6}$$

The important materials properties for high-performance battery electrodes are apparent from equation 1.6. A good cathode-anode pair maximizes $(E_{\text{cathode}}(x) - E_{\text{anode}}(x))$ and $n(x_{\max} - x_{\min})$. The latter quantity is called the capacity, and it corresponds to the total amount of charge that can be extracted from or inserted into an electrode. When normalized by the electrode material's molar mass it is referred to as the specific capacity. Specific capacity is often reported in units of milliampere hours per gram, mA h g^{-1}. Much of modern materials science for batteries is devoted to predicting, synthesizing, and characterizing new electrodes with these properties.

1.2.2 Kinetics of crystalline electrodes

Besides thermodynamics, the kinetics of the reaction strongly influence battery performance. Electrochemical kinetics are governed in many important cases by the Butler–Volmer equation [6],

$$i = i_0 \left[\frac{c_o}{c_o^0} \exp\left(\frac{\alpha_{\text{a}} F \eta}{k_{\text{B}} T} \right) - \frac{c_r}{c_r^0} \exp\left(\frac{-\alpha_{\text{c}} F \eta}{k_{\text{B}} T} \right) \right]. \tag{1.7}$$

Here i is the areal current density; i_0 is the areal exchange current density; c_i/c_i^0 are the ratios of the oxidant or reductant concentration at the electrode surface to the bulk concentrations; α_i are the anodic and cathodic exchange coefficients; k_{B} is the Boltzmann constant, 1.381×10^{-23} J K^{-1}; T is the thermodynamic temperature; and η is the overpotential. (Note that I have the adopted the convention with Newman [6] that positive overpotentials result in positive, oxidizing currents. Bard takes the opposite convention [8].) The overpotential is defined as the difference between an electrode's operating potential and its equilibrium potential,

$$\eta = E - E_{\text{eq}}. \tag{1.8}$$

It can be thought of as a measure of how far from equilibrium an electrode must be driven to produce the desired current density, i.

A battery's rate capability refers to how quickly it can be charged or discharged. Improving a battery's rate capability requires increasing the battery's areal current density, i. As equation 1.7 shows, increasing the magnitude of i requires increasing the overpotential. Doing so, however, has two effects on the cell potential, and thus on the overall energy. First, increasing the magnitude of the overpotential in the cathode, where reduction occurs during discharge, requires decreasing E_{cathode} relative to its equilibrium value, per equation 1.8. Similarly, E_{anode} must increase relative to its equilibrium value. This is precisely the opposite of what is needed to maximize the cell energy, as discussed above. Second, increasing the magnitude of the overpotential causes the capacity, $n(x_{\text{max}} - x_{\text{min}})$, to decrease. This is due to the fact that x_{min}, for example, is determined practically by the minimum potential the cathode can achieve before the onset of deleterious, irreversible side reactions. So the cathode driven at a higher overpotential (magnitude) will reach the minimum safe potential at a higher value of x compared to the same battery operated at a slower rate. This leads to the general trend that increasing the rate at which a battery is operated decreases the amount of energy that can be extracted [9].

1.2.3 Mass transport in the electrolyte phase

Finally, transport phenomena in the electrolyte phase are critically important to understanding and improving battery operation. They are discussed here only briefly because this work focuses on the simulation of crystalline electrodes. But transport in the electrolyte is simply too important and too active an area of research to omit completely. In contrast to electrodes, electrolytes must be ionically conducting but electronically insulating. This ensures all electrons move through the external circuit and prevents short circuits, which are damaging and dangerous. Conduction,

diffusion, and convection all contribute to the flux of ions through the electrolyte, N, according to [6]

$$N = -nuFc\nabla\Phi - D\nabla c + cv \tag{1.9}$$

where n is (still) the valency, u is the ion mobility, c is the concentration, Φ is the electric potential field, D is the diffusivity, and v is the velocity of bulk flow (if any). Poor transport in the electrolyte has several undesirable effects. First, it increases the overpotential in analogy to the effect of conductivity in the electrodes discussed above. Second, it can deplete the ionic concentration at the cathode during discharge, which decreases the areal current density per the c_r/c_r^0 term in equation 1.7. Additionally, depletion at the anode during charge can lead to the metal plating and the formation of dendrites, which frequently cause cell failure - especially in lithium-metal anodes [10]. A great deal of research and development goes into optimizing the electrolyte for diverse applications, and a commercially viable solid-state electrolyte remains one of the great unsolved challenges of modern materials science.

This section reviews the general science and salient materials properties of electrochemical cells. While lithium-ion batteries are the incumbent technology, sodium- and potassium-ion batteries will be important components of the global energy-storage portfolio in any scenario where lithium or cobalt becomes scarce or prohibitively expensive [11]. More detailed reviews of the broader literature on these batteries can be found in references [12–14]. This work deals with calculating these and other properties of the PBAs for next-generation batteries.

1.3 Diverse, tunable materials properties of the Prussian blue analogs

The Prussian blue analogs (PBAs) are a scientifically and technologically important class of closely related materials. They have been applied as active electrochemical materials in clean energy technologies including sodium- [15–17] and potassium-ion

[18, 19] and all-solid-state [20] batteries, as well as electrocatalysis [21], thermionics [22], capacitors [23], and smart windows [24]. Outside clean energy, they are used as sensors [25], MRI contrast agents [26], and as a medicine for treatment of heavy- and radioactive-metal poisoning [27, 28]. Scientifically, the PBAs are a sandbox for the exploration of important, fundamental phenomena in solid-state physics and electronic-structure theory. They exhibit redox activity [29]; mixed valency [30] and disproportionation [31]; photo-induced charge transfer [32]; electronic spin transitions [33]; and ferro-, antiferro-, and ferrimagnetism [34, 35]. They have the general formula

$$A_x^I M^J [M'^K(\mathrm{CN})_6]_{1-y} \cdot w\mathrm{H_2O}. \tag{1.10}$$

Here, M and M' are possibly distinct transition metals in oxidation states J and K, respectively. They are bridged by cyanide ligands to form the PBA lattice as shown in Figure 1.3. The interstitial ion, A, has oxidation state I and is present in an amount x. There are y vacancies of the hexacyanometallate (M' and its six cyanide ligands), and there are w crystalline water molecules present per formula unit. The charge neutrality condition is then $xI + J + (1-y)(K-6) = 0$. The remainder of this section discusses the structure-property relationships in the PBAs.

1.3.1 The carbon-coordinated metal

The metal M' is octahedrally coordinated to the cyanide ligands via the carbon atoms. Synthetically, the PBAs are often prepared by a simple, aqueous co-precipitation reaction between the hexacyanometallate complex anion (where the central metal is M') and the cation that is to occupy the nitrogen-coordinated position [1]. So the availability of the hexacyanometallate salt can limit or at least complicate the choice of carbon-coordinated element. Salts of hexacyanoferrate are readily available, and others are more difficult to source or prepare. Structurally, the carbon-coordinated element strongly influences lattice parameter [36], and, therefore, density. Electrochemically, the lattice parameter can also determine the size of the channel through

which ions move in the crystal, so the choice of M' influences ion kinetics. The carbon-coordinated ion is (usually) the sole redox center for high-vacancy PBAs [16] and is (usually) the higher-potential redox center in compositions for which the nitrogen-coordinated ion also reacts [37]. The potentials for the hexacyanoferrate(III/II), hexacyanomanganate(III/II), and hexacyanochromate(III/II) couples are about +1, 0, and -1 V versus the standard hydrogen electrode (SHE), respectively [1].

1.3.2 The nitrogen-coordinated metal

The metal M is nitrogen-coordinated. Manganese [38], iron [39], and cobalt [40] hexacyanoferrates are of particular importance because they have been shown to be redox active within the electrochemical stability window of conventional organic electrolytes for next-generation cathodes. This nearly doubles theoretical specific capacity from $92\,\mathrm{mA\,h\,g^{-1}}$ to $171\,\mathrm{mA\,h\,g^{-1}}$ for sodiated Prussian blue, $NaFe[Fe(CN)_6]$. The reduction potential for the redox couple on the nitrogen-coordinated iron is usually within about 1 V of the hexacyanometallate's, and, in the case of dehydrated sodium manganese hexacyanoferrate, the two potentials are indistinguishable. The choice of nitrogen-coordinated element in conjunction with the choice of carbon-coordinated elements also determines important magnetic properties. For instance, the two metal centers in iron hexacyanoferrate align ferromagnetically, while they align antiferromagnetically in chromium hexacyanochromate [41].

1.3.3 The interstitial ion

Insertion or removal of the ion A balances the charge in the material as the compound is reduced or oxidized. The alkali metals lithium [42], sodium [16], potassium [18], rubidium [43], and cesium [44]; alkaline-earth metals magnesium [45] and calcium [46], and ions of other elements including aluminum [47] and zinc [48] have been inserted into the PBA lattice, shown schematically in Figure 1.4. Crystallographically, X-ray diffraction has convincingly placed the position of heavier atoms like rubidium

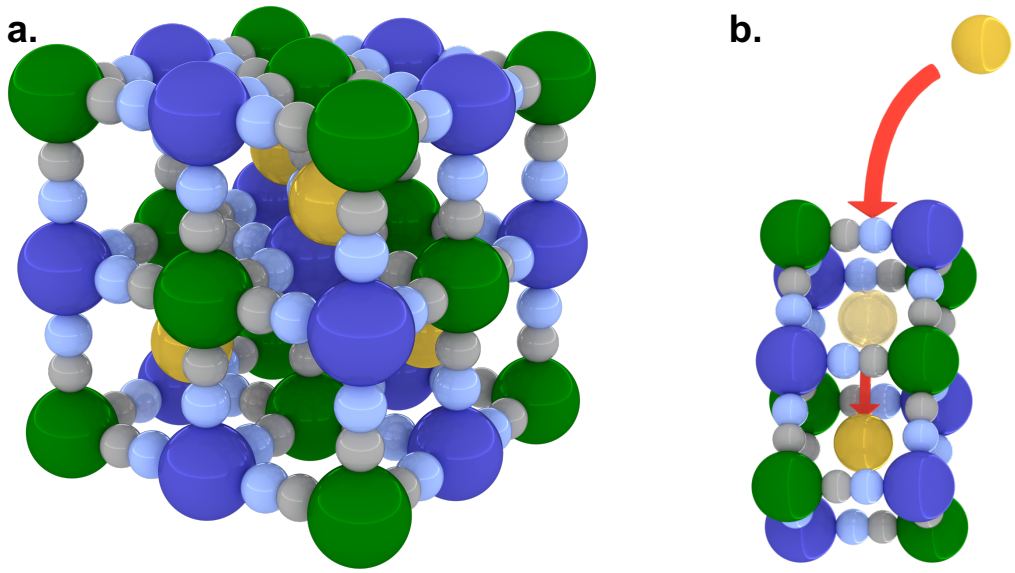

Figure 1.3: Crystal structure and ion transport. In (a), blue, green, gold, light blue, and gray atoms correspond to the nitrogen-coordinated, carbon-coordinated, and inserting ions and the nitrogen and carbon atoms, respectively. In (b), an inserting ion enters and moves from one subcube to another. Adapted with permission from [5]. Copyright 2018 Cell Press.

at the center of the interstitial site [49]. Locating the smaller ions like sodium is harder because they are lighter with smaller scattering cross sections, but computational evidence suggests that sodium prefers the interfacial position between two subcubes (see Chapter 3). Electrochemically, the reduction potential for insertion of the alkali metals increases with their ionic radius. The reduction potentials for nickel hexacyanoferrate for lithium, sodium, potassium, rubidium, and cesium are 0.4, 0.6, 0.7, 0.9, and 1.3 V versus the SHE, respectively [43] .

1.3.4 Vacancies, the primary defect

Vacancies of the hexacyanometallate complex are the most important defect in the PBAs [50]. A vacancy can be thought of as a positively charged defect competing with the inserting ion, A, for occupation. So vacancies severely limit specific capacity and therefore specific energy. A vacancy concentration of 10% (a common value for widely used synthesis conditions) leads to a decrease in theoretical specific capacity

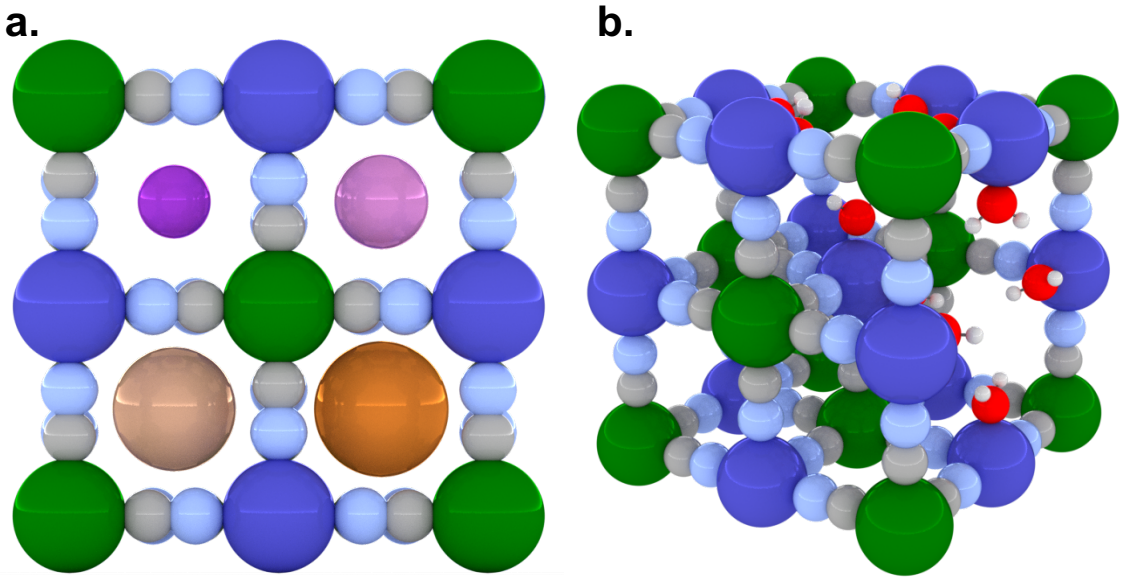

Figure 1.4: Tunable PBA crystallography. In (a), the inserting ions' relative sizes are shown. They are (clockwise from upper left) lithium, sodium, rubidium, and potassium. Ionic radii, taken from [53] are (Li, 0.92 Å), (Na, 1.18 Å), (K, 1.51 Å), and (Rb, 1.66 Å). In (b), two vacancies of the hexacyanometallate are shown with water coordinated to the under-coordinated lattice ions. Adapted with permission from [5]. Copyright 2018 Cell Press.

of 18%. Vacancies have two beneficial effects on PBA electrochemistry. First, there is evidence that vacancies open alternative routes for ion transport that can lead to faster solid-state diffusion and better rate capability in batteries. In the case of cesium, it seems that the ions are too large to move through the subcube faces at room temperature and that vacancy-mediated transport is the primary method of cesium conduction in PBAs [51]. Second, vacancies ameliorate undesirable phase changes that occur during discharge and that can decrease cycle life. A cubic-to-tetragonal transition is observed on oxidation of sodium manganese hexacyanoferrate because of the formation of manganese(III, high spin), inducing a Jahn–Teller distortion. With 17% vacancies, this transition was not observed [52]. Vacancy content must be optimized between the competing demands of high energy, high power, and long life.

1.3.5 The importance of crystalline water

The role of water in PBA crystallography and electrochemistry is a highly active area of research. Neutron diffraction studies have shown two distinct sites that water occupies [54, 55]. The first is zeolitic water, residing in the interstice. The second is bonded to under-coordinated ions at vacancies. Water seems to increase the rate of ion transport through the lattice, though the mechanism is poorly understood. The PBA battery with the highest recorded cycle life used an acidic proton as the counter ion and leveraged a Grotthuss-type conduction mechanism to achieve 0.73 million cycles [56]. In contrast, PBA electrodes targeting high specific energy are usually dehydrated aggressively [15]. Achieving high capacity requires cycling at higher voltages, which can lead to undesirable side reactions. As with vacancy engineering, water content has to be designed depending on the battery's application.

The PBAs have a wide composition space of lattice metals (M and M'), inserting ion (A), vacancy content (y), and water content (w), which leads to the great diversity and tunability in their materials properties. Comprehensive reviews of these and other structure-property relationships for batteries can be found in references [57–59]. There remains substantial opportunity, though, to better understand and even expand on the structure-property relationships described above. First-principles modeling is a powerful tool in that endeavor.

1.4 A survey of density-functional theory for batteries

This section introduces DFT as a useful tool by examining three examples of the technique in practice. The goal of this section is not to explain how DFT works or how the calculations considered were set up. Chapter 2 details DFT as a method, including its theoretical underpinnings and practical considerations for setting up

calculations. The aim of this section is rather to motivate the use of DFT by demonstrating several import and interesting contributions to battery science. These are Jung and coworkers' rationalization of the reaction voltages in sodium manganese oxide through a study of the material's stable phases; Ceder and coworkers' elucidation of design principles for the lithium solid electrolytes by calculating activation energies of transition states; and Bruce, Pérez-Osario, and coworkers' determination of the role of molecular-oxygen formation in the first-cycle hysteresis in lithium-rich transition-metal oxides.

1.4.1 Predicting insertion voltages for a sodium-ion cathode

Sodium-ion batteries are an increasingly active area of battery research. Two reasons for this are that sodium-ion batteries replace rare and expensive lithium with ubiquitous and inexpensive sodium and because there are fewer (if any) adequate active materials for electrodes relative to lithium-ion technology. Some compounds that are inert toward lithium insertion, like layered chromium dioxide, are active for sodium ions, while some lithium-ion electrodes like graphite are inert toward sodium intercalation. Certain transition-metal oxides, like sodium manganese oxide, are an interesting middle case; that is, Li_xMnO_2 is an excellent lithium-ion cathode and while Na_xMnO_2 is electrochemically active, it has a wide range of insertion potentials.

Jung and coworkers studied the charge-storage mechanism for sodium ions in the material $Na_{0.44}MnO_2$ using DFT [60]. The various stable phases of Na_xMnO_2 for $x \in [0.17, 0.67]$ were calculated. They simulated 156 difference sodium-ion configurations in the host lattice; the formation energies they calculated for these compounds are reproduced in Figure 1.5. The convex hull of formation energies consists of 7 stable sodium stoichiometries between 0.17 and 0.67. Figure 1.5 shows also the insertion-voltage profile calculated by Jung and coworkers. It is in very good agreement with the experimental data, reproducing the 1.75 V variation in the reduction potential

between $Na_{0.17}MnO_2$ and $Na_{0.67}MnO_2$. They found that the lattice structure actually changes very little over the course of the reaction.

1.4.2 Elucidating design rules for solid electrolytes

One important goal of battery science today is the design of a viable solid electrolyte. A solid electrolyte has a significant advantage, per se, over the incumbent technology in that it is safer. Lithium-ion batteries contain a liquid electrolyte that is comprised of a highly flammable organic solvent like ethylene carbonate, diethyl carbonate, dimethyl carbonate, ethyl methyl carbonate, or a mixture of those, with dissolved conductive and hazardous salts like lithium fluorophosphate and other additives. A solid electrolyte would replace this flammable electrolyte with a safer overall device. A solid electrolyte may also enable the use of an energy-dense lithium-metal anode. The first requirement of a solid electrolyte is adequate lithium-ion conductivity (on the order of 1 $mS\,cm^{-1}$ to be comparable to liquid electrolytes).

Ceder and coworkers published design principles for developing solid-state lithium superionic conductors in 2015 [61]. To study how easily lithium ions can be conducted through a lattice, they relied on the nudged elastic band method. Briefly, nudged elastic band is a strategy for calculating the energy of a transition state between two local minima on the potential energy surface. In this study, they examined the movement of lithium ions through theoretical lattices of sulfide anions (S^{2-}), free of any other cations. The results of some of their calculations are shown in Figure 1.6. They find that the lowest activation energies arise when the sulfide anions are arranged in a body-centered-cubic geometry. In particular, the bcc-like structure has an activation energy of 0.18 eV, versus 0.4 eV for the fcc-like and hcp-like geometries. As they describe it, the bcc-like arrangement uniquely produces a connected network of tetrahedral sites between which lithium ions can move easily. They confirm this structural motif is present in two known lithium superionic conductors ($Li_{10}GeP_2S_{12}$

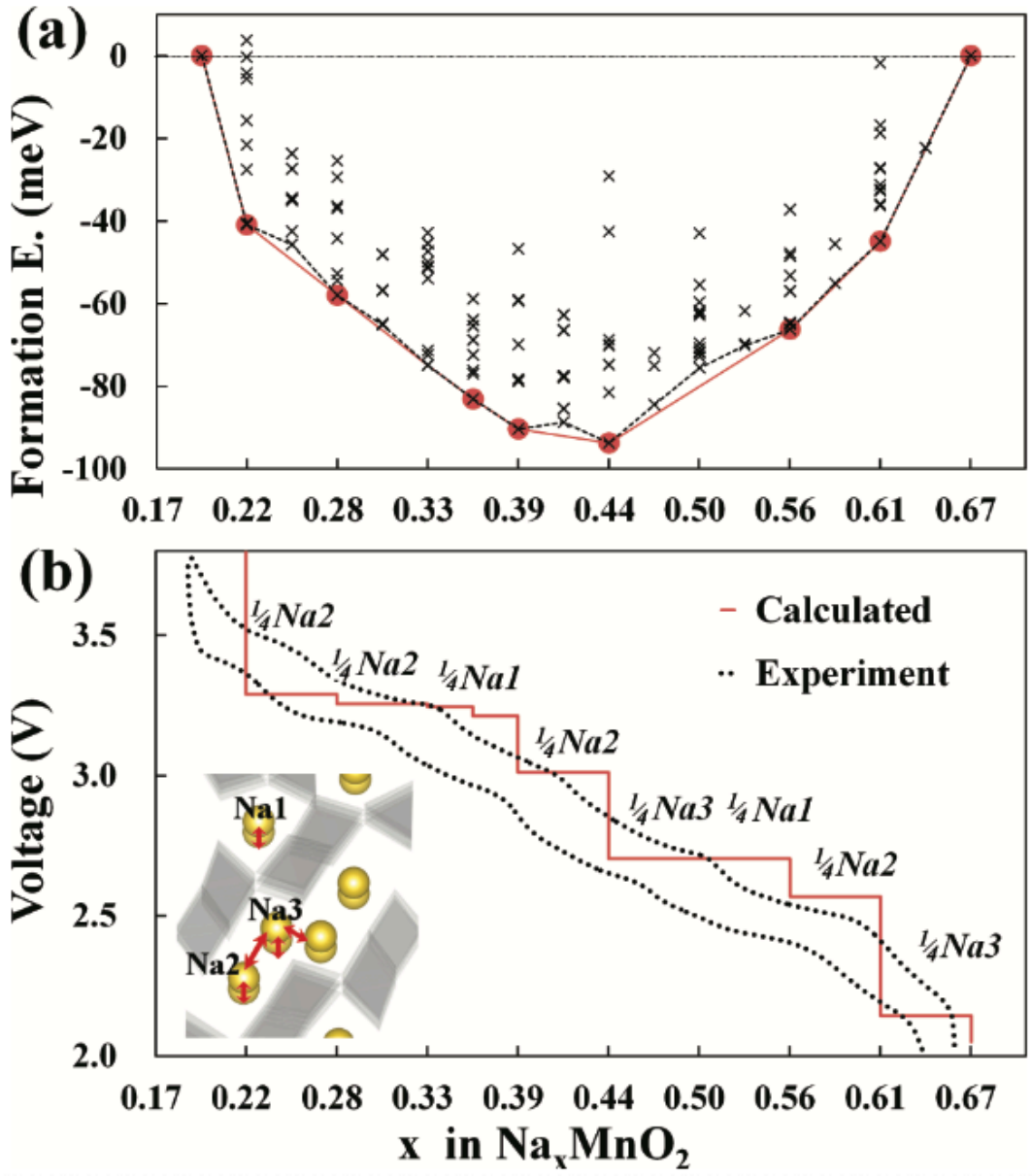

Figure 1.5: Formation energies and voltage in a sodium-ion electrode. Reprinted with permission from [60]. Copyright 2012 American Chemical Society.

and $Li_7P_3S_{11}$) and suggest that it can be used to design new electrolytes for solid-state batteries. This study is also a excellent demonstration of DFT's power to answer questions in ways that are challenging or impossible experimentally.

1.4.3 Formation of molecular oxygen in lithium-rich cathodes

The charge-storage mechanism in transition-metal oxides like Li_xMO_2 involves the reduction of the transition-metal ions on insertion of the lithium ions. However, the maximum capacity (the $n(x_{\max}-x_{\min})$ value from section 1.2) can be increased by synthesized a "lithium-rich" cathode with a formula that can be written as $Li_{x+\delta}M_{1-\delta}O_2$. Here, a small amount, δ, of the lattice transition-metal ions are substituted by lithium, which can be extracted without destroying the crystal structure. This strategy can lead to a cathode specific capacity of over $200\,\mathrm{mA\,h\,g^{-1}}$, compared to about $180\,\mathrm{mA\,h\,g^{-1}}$ in state-of-the-art cathodes. In these materials, the charge-storage mechanism also involves oxygen redox (**red**uction / **ox**idation) to balance the charge. This technology is still in the research phase; important questions about the reversibility of the reaction are still being investigated. However, this is one of the most promising areas of research to improve the performance of the lithium-ion battery - a technology that has been heavily optimized since its inception in 1990.

The effect of extracting this excess charge was investigated by Bruce, Pérez-Osario, and coworkers in a combined computational and experimental study [62]. They determined that the large hysteresis in the first cycle for $Na_{0.75}[Li_{0.25}Mn_{0.75}O_2]$ is due to the formation of molecular oxygen in the crystal structure. There was substantial experimental evidence for this, and it was complimented by their computational data shown in Figure 1.7. Pérez-Osario's key insights were crystallographic and electronic. First, relaxation of the crystal geometries for the high-voltage phase of the compound (that is, the phase with many alkali-metal ions removed) revealed migration of the manganese ions with a concomitant decrease in some O–O bond distances, from 2.6 Å to

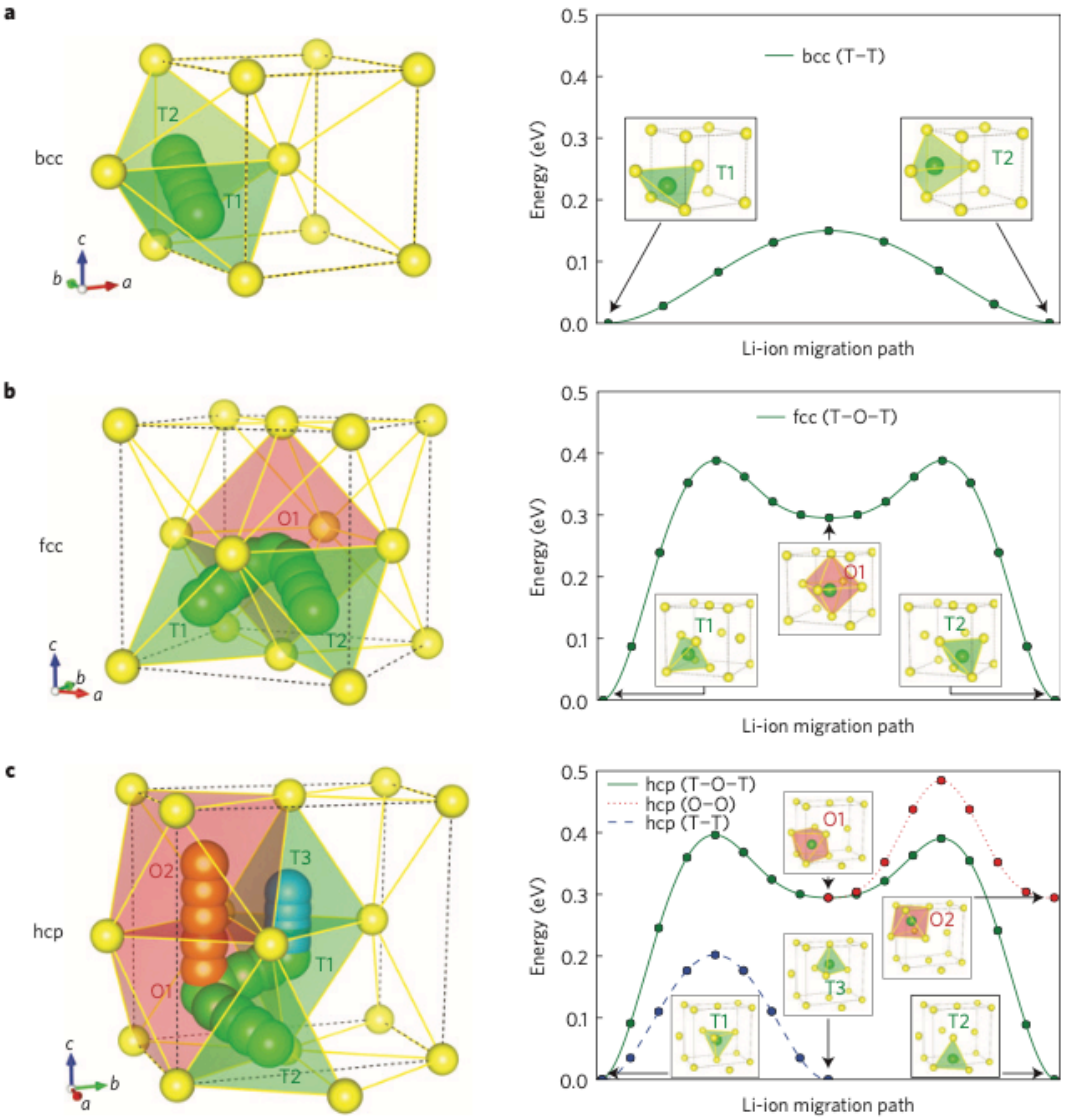

Figure 1.6: Different paths and associated activation energies. Reprinted with permission from [61]. Copyright 2015 Nature Publishing Group.

1.2 Å. This latter value is equal to the bond length in a diatomic oxygen molecule. Furthermore, the atom-projected densities of states reveal that states arising from the oxygen orbitals take on much more molecular π and π^* character, also consistent with the formation of molecular oxygen. The authors were able to use these insights to synthesize a different phase in which the manganese was unable to migrate. This prevented the formation of molecular oxygen and decreased the hysteresis. In this case, DFT was able to provide complementary, consistent data on a complicated and unintuitive reaction mechanism.

Three case studies are presented in this section. Each demonstrates the use of DFT in battery science. Calculation of reduction potential for sodium-ion cathodes, establishing design principles for solid electrolytes, and collaborating with experiment to understand a deleterious reaction mechanism are only a few of the many benefits that theory and computation have for electrochemical energy storage. Excellent reviews of how to use DFT to model battery materials can be found in references [63–65].

1.5 Overview of this work

1.5.1 State of the art in ab-initio simulation of PBAs for energy storage

Some of the earliest PBA modeling was performed on magnetic systems, including the hexacyanochromates and hexacyanovanadates, using a "binuclear" model to calculate magnetic exchange coupling constant [66, 67]. Modeling for batteries began in earnest with Wojdeł and coworkers in the first decade of the 2000s. Their first attempts to model the strong correlation in Prussian blue, $NaFe[Fe(CN)_6]$, relied on the use of two different pseudopotentials for carbon- and nitrogen-coordinated ions in the lattice [68–70]. They would go on to apply more advanced methods including DFT+U and hybrid functionals to predict half-metallic conductivity [71], to correlate hydration state with

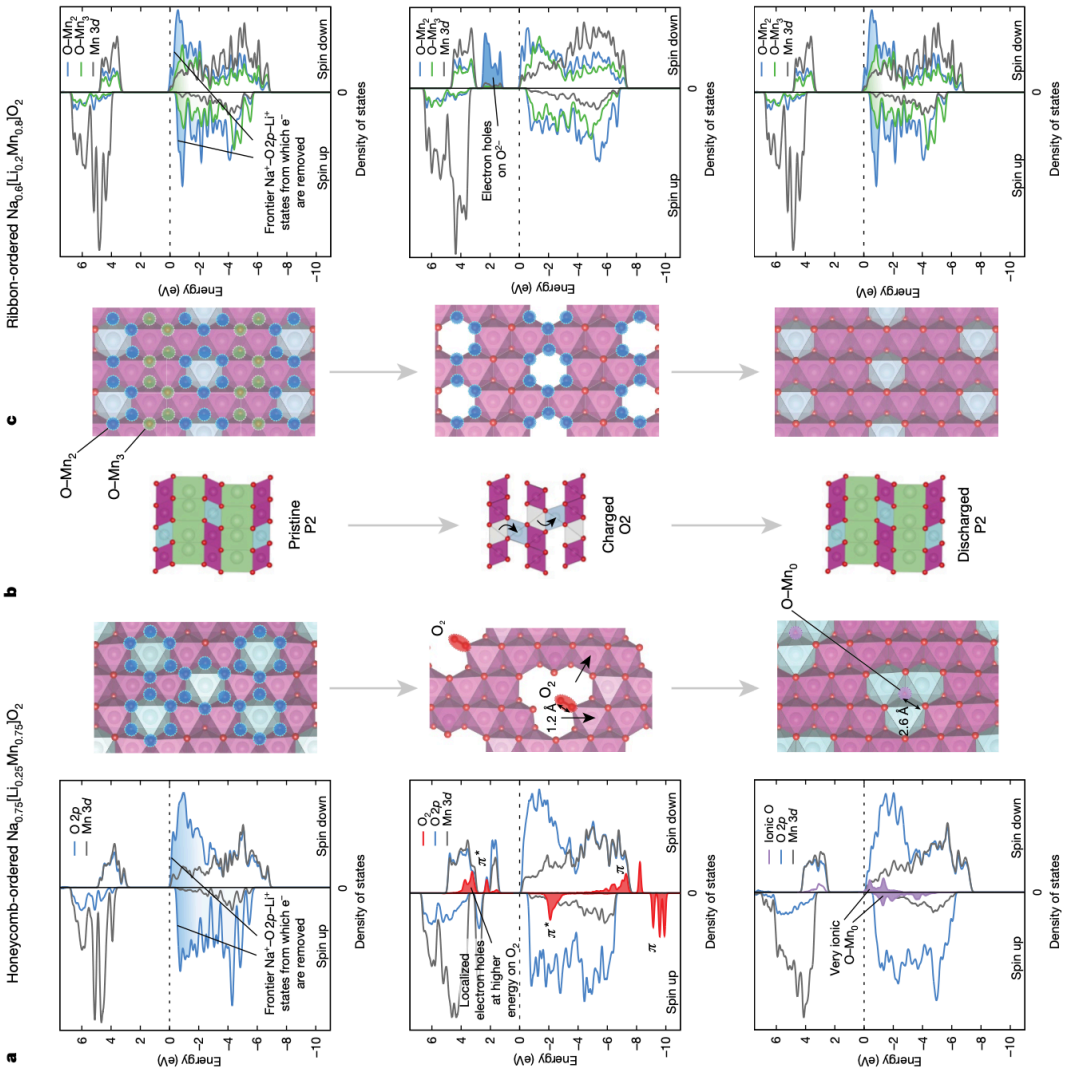

Figure 1.7: Formation of molecular oxygen. Reprinted with permission from [62]. Copyright 2020 Nature Publishing Group.

band gap [72], and to look at spin-crossover in cesium iron hexacyanochromate [73]. In 2013, Mizuno and coworkers used DFT+U to show that the voltage of a PBA increases with the ionic radius of the inserting ion [74]. Henkelman, Goodenough, and coworkers conducted a thorough theoretical investigation of the different stable phases of dehydrated sodium manganese hexacyanoferrate [75] to help explain data from a ground-breaking experimental study that found certain drying conditions which improved electrode performance [15]. In 2016, Hegner and coworkers tabulated a wide variety of simulated properties for the three oxidation states of Prussian blue [76]. And, most recently, Ong and coworkers studied the effect of water and voltage on PBA phase stability in diverse compositions [77].

1.5.2 Outline of this work

Despite the excellent work described above, important theoretical questions about the PBAs—including charge-transport properties, stability of highly sodiated phases, and the electronic structure of vacancy defects—remain. This work shows that **important electrochemical properties of the PBAs are calculable from first principles, but advanced, DFT-based methods including hybrid functionals and DFT+U are necessary to model strong correlation in these materials' electronic structures**.

The remainder of this work is organized as follows. Chapter 2 explains the theoretical underpinnings of DFT, practical considerations for setting up calculations, and the steps involved in proceeding from the output of DFT (total energy and ground-state electronic density) to materials properties relevant to battery performance. The chapter begins from the time-independent many-body Schrödinger equation and proceeds through the Hohenberg and Kohn Theorem, the Kohn–Sham equations, conventional and advanced functionals, and finally the mathematical operations to calculate battery properties from the output of DFT.

In Chapter 3, the electronic structure and electron-transport properties of three cathode materials are calculated and discussed. The materials are manganese, iron, and cobalt hexacyanoferrate, which are very promising active materials as positive electrodes in sodium- and potassium-ion batteries. A hybrid functional is used to find the ground-state spin configuration for each compound. From there, the projected densities of states are plotted to identify valence- and conduction-band states. Finally, the effective masses of electrons and holes are calculated. This work is the first experimental or theoretical calculation of effective masses in the PBAs. Future work on small-polaron hopping is suggested.

Chapter 4 addresses a quizzical, outstanding question from experimental PBA science. What is the origin of the specific capacity (209 mA h g^{-1}) in sodium manganese hexacyanomanganate? The formation energies for various oxidation states and magnetic phases for this system are calculated and the convex hull of stable phases is constructed. The simulated X-ray diffractograms are compared to synchrotron data from a previously published study and the electronic structure is examined through the projected densities of states and through the projected charges and magnetic moments. Finally, crystalline water is simulated in this system to examine how it affects the material's properties.

In Chapter 5, I consider the anode and molecular magnet chromium hexacyanochromate. A defect-free version of this compound is highly desirable, but it has thus-far eluded experimentalists. So I predict several materials properties in this material to provide theoretical support for ongoing efforts in our laboratory to synthesize it. First, I parameterize the Hubbard U values for this material, and then I use those values and supercells to explore four alkali-metal chromium hexacyanochromates: those base on sodium, potassium, rubidium, and cesium. I predict unit-cell volumes, reduction potentials, activation energies, infrared-spectroscopy absorption frequencies, and magnetic ordering.

Finally, the work concludes in Chapter 6 with a summary of the key results, and a description of important, future studies enabled by these findings. This work is an important contribution to the science of PBA electrochemistry and electronic structure. It is also an interesting story of advanced DFT-based methods achieving chemical accuracy in a spin-polarized, strongly correlated system. And this work enables future studies for faster commercialization and deeper understanding of next-generation batteries.

References

[1] F. Scholz and A. Dostal, "The formal potentials of solid metal hexacyanometalates," *Angewandte Chemie International Edition in English*, vol. 34, no. 23-24, pp. 2685–2687, 1996.

[2] P. Peter Atkins and J. De Paula, *Atkins' physical chemistry*. OUP Oxford, 2014.

[3] M. Pasta, D. Armstrong, Z. L. Brown, J. Bu, M. R. Castell, P. Chen, A. Cocks, S. A. Corr, E. J. Cussen, E. Darnbrough, *et al.*, "2020 roadmap on solid-state batteries," *Journal of Physics: Energy*, vol. 2, no. 3, p. 032008, 2020.

[4] T. B. Reddy, *Linden's handbook of batteries*. McGraw-Hill Education, 2011.

[5] K. Hurlbutt, S. Wheeler, I. Capone, and M. Pasta, "Prussian Blue Analogs as Battery Materials," *Joule*, vol. 2, no. 10, pp. 1950–1960, 2018.

[6] J. Newman and K. E. Thomas-Alyea, *Electrochemical systems*. John Wiley & Sons, 3 ed., 2012.

[7] K. Mizushima, P. C. Jones, P. J. Wiseman, and J. B. Goodenough, "Li_xCoO_2 ($0< x \leq 1$): A new cathode material for batteries of high energy density," *Solid State Ionics*, vol. 3-4, pp. 171–174, 1981.

[8] L. R. Faulkner and A. J. Bard, *Electrochemical methods: fundamentals and applications*. John Wiley & Sons, 2 ed., 2002.

[9] M. Doyle, Newman, John, and T. F. Fuller, "Modeling of Galvanostatic Charge and Discharge of the Lithium/Polymer/Insertion Cell," *Journal of The Electrochemical Society*, vol. 140, no. 6, p. 1526, 1993.

[10] J. B. Goodenough and Y. Kim, "Challenges for rechargeable batteries," *Journal of Power Sources*, vol. 196, no. 16, pp. 6688–6694, 2011.

[11] C. Vaalma, D. Buchholz, M. Weil, and S. Passerini, "A cost and resource analysis of sodium-ion batteries," *Nature Reviews Materials*, vol. 3, no. 4, pp. 1–11, 2018.

[12] J.-Y. Hwang, S.-T. Myung, and Y.-K. Sun, "Sodium-ion batteries: present and future," *Chemical Society Reviews*, vol. 46, no. 12, pp. 3529–3614, 2017.

[13] K. Kubota, M. Dahbi, T. Hosaka, S. Kumakura, and S. Komaba, "Towards K-Ion and Na-Ion Batteries as 'Beyond Li-Ion'," *The Chemical Record*, vol. 18, pp. 1–22, 2018.

[14] N. Yabuuchi, K. Kubota, M. Dahbi, and S. Komaba, "Research development on sodium-ion batteries," *Chemical Reviews*, vol. 114, no. 23, pp. 11636–11682, 2014.

[15] J. Song, L. Wang, Y. Lu, J. Liu, B. Guo, P. Xiao, J. J. Lee, X. Q. Yang, G. Henkelman, and J. B. Goodenough, "Removal of interstitial H_2O in hexacyanometallates for a superior cathode of a sodium-ion battery," *Journal of the American Chemical Society*, vol. 137, no. 7, pp. 2658–2664, 2015.

[16] Y. Lu, L. Wang, J. Cheng, and J. B. Goodenough, "Prussian blue: a new framework of electrode materials for sodium batteries," *Chemical Communications*, vol. 48, no. 52, p. 6544, 2012.

[17] M. Pasta, C. D. Wessells, N. Liu, J. Nelson, M. T. McDowell, R. A. Huggins, M. F. Toney, and Y. Cui, "Full open-framework batteries for stationary energy storage," *Nature Communications*, vol. 5, pp. 1–9, 2014.

[18] M. Fiore, S. Wheeler, K. Hurlbutt, I. Capone, J. Fawdon, R. Ruffo, and M. Pasta, "Paving the Way Toward Highly Efficient High-Energy Potassium-Ion Batteries with Ionic-Liquid Electrolytes," *Chemistry of Materials*, vol. 32, pp. 7653–7661, 2020.

[19] L. Jiang, Y. Lu, C. Zhao, L. Liu, J. Zhang, Q. Zhang, X. Shen, J. Zhao, X. Yu, H. Li, X. Huang, L. Chen, and Y.-S. Hu, "Building aqueous K-ion batteries for energy storage," *Nature Energy*, vol. 4, no. 6, pp. 495–503, 2019.

[20] H. Gao, S. Xin, L. Xue, and J. B. Goodenough, "Stabilizing a High-Energy-Density Rechargeable Sodium Battery with a Solid Electrolyte," *Chem*, vol. 4, no. 4, pp. 833–844, 2018.

[21] Z.-Y. Yu, Y. Duan, J.-D. Liu, Y. Chen, X.-K. Liu, W. Liu, T. Ma, Y. Li, X.-S. Zheng, T. Yao, M.-R. Gao, J.-F. Zhu, B.-J. Ye, and S.-H. Yu, "Unconventional CN vacancies suppress iron-leaching in Prussian blue analogue pre-catalyst for boosted oxygen evolution catalysis," *Nature Communications*, vol. 10, no. 1, p. 2799, 2019.

[22] C. Gao, Y. Yin, L. Zheng, Y. Liu, S. Sim, Y. He, C. Zhu, Z. Liu, H.-W. Lee, Q. Yuan, and S. W. Lee, "Engineering the Electrochemical Temperature Coefficient for Efficient Low-Grade Heat Harvesting," *Advanced Functional Materials*, vol. 28, p. 1803129, 2018.

[23] S.-C. Wang, M. Gu, L. Pan, J. Xu, L. Han, and F.-Y. Yi, "The interlocked in situ fabrication of graphene@ prussian blue nanocomposite as high-performance supercapacitor," *Dalton Transactions*, vol. 47, no. 37, pp. 13126–13134, 2018.

[24] T. Shibata and Y. Moritomo, "Quick Response of All Solid Electrochromic Device," *Applied Physics Express*, vol. 2, no. 10, p. 105502, 2009.

[25] A. A. Karyakin, "Advances of Prussian blue and its analogues in (bio)sensors," *Current Opinion in Electrochemistry*, vol. 5, no. 1, pp. 92–98, 2017.

[26] M. Shokouhimehr, E. S. Soehnlen, A. Khitrin, S. Basu, and S. D. Huang, "Biocompatible Prussian blue nanoparticles: Preparation, stability, cytotoxicity, and potential use as an MRI contrast agent," *Inorganic Chemistry Communications*, vol. 13, no. 1, pp. 58–61, 2010.

[27] Y. Yang, P. J. Faustino, J. J. Progar, C. R. Brownell, N. Sadrieh, J. C. May, E. Leutzinger, D. A. Place, E. P. Duffy, L. X. Yu, M. A. Khan, and R. C. Lyon, "Quantitative determination of thallium binding to ferric hexacyanoferrate: Prussian blue," *International Journal of Pharmaceutics*, vol. 353, no. 1-2, pp. 187–194, 2008.

[28] G. Lin, L. Yuan, L. Bai, Y. Liu, Y. Wang, and Z. Qiu, "Successful treatment of a patient with severe thallium poisoning in a coma using Prussian blue and plasma exchange," *Medicine*, vol. 98, no. 8, pp. 3–6, 2019.

[29] K. Itaya, I. Uchida, and V. D. Neff, "Electrochemistry of Polynuclear Transition Metal Cyanides: Prussian Blue and Its Analogues," *Accounts of Chemical Research*, vol. 19, no. 6, pp. 162–168, 1986.

[30] J. W. McCargar and V. D. Neff, "Thermodynamics of mixed-valence intercalation reactions: the electrochemical reduction of prussian blue," *The Journal of Physical Chemistry*, vol. 92, no. 12, pp. 3598–3604, 1988.

[31] R. Klenze, B. Kanellakopulos, G. Trageser, and H. H. Eysel, "Manganese hexacyanomanganate: Magnetic interactions via cyanide in a mixed valence Prus-

sian blue type compound," *The Journal of Chemical Physics*, vol. 72, no. 11, pp. 5819–5828, 1980.

[32] M. Cammarata, S. Zerdane, L. Balducci, G. Azzolina, S. Mazerat, C. Exertier, M. Trabuco, M. Levantino, R. Alonso-Mori, J. M. Glownia, S. Song, L. Catala, T. Mallah, S. F. Matar, and E. Collet, "Charge transfer driven by ultrafast spin transition in a CoFe Prussian blue analogue," *Nature Chemistry*, vol. 13, no. 1, pp. 10–14, 2021.

[33] M. Pasta, R. Y. Wang, R. Ruffo, R. Qiao, H.-W. Lee, B. Shyam, M. Guo, Y. Wang, L. A. Wray, W. Yang, M. F. Toney, and Y. Cui, "Manganese–cobalt hexacyanoferrate cathodes for sodium-ion batteries," *Journal of Materials Chemistry A*, vol. 4, no. 11, pp. 4211–4223, 2016.

[34] E. Ruiz, A. Rodríguez-Fortea, S. Alvarez, and M. Verdaguer, "Is it possible to get high T_C magnets with Prussian blue analogues? A theoretical prospect," *Chemistry - A European Journal*, vol. 11, no. 7, pp. 2135–2144, 2005.

[35] A. Bleuzen, C. Lomenech, V. Escax, F. Villain, F. Varret, C. Cartier dit Moulin, and M. Verdaguer, "Photoinduced Ferrimagnetic Systems in Prussian Blue Analogues $C^{I}_{x}Co_4[Fe(CN)_6]_y$ (C^{I} = Alkali Cation). 1. Conditions to Observe the Phenomenon," *Journal of the American Chemical Society*, vol. 122, no. 28, pp. 6648–6652, 2000.

[36] A. Ludi and H. U. Güdel, "Structural chemistry of polynuclear transition metal cyanides," *Inorganic Chemistry*, pp. 1–21, 1973.

[37] L. Wang, J. Song, R. Qiao, L. A. Wray, M. A. Hossain, Y. D. Chuang, W. Yang, Y. Lu, D. Evans, J. J. Lee, S. Vail, X. Zhao, M. Nishijima, S. Kakimoto, and J. B. Goodenough, "Rhombohedral Prussian white as cathode for rechargeable

sodium-ion batteries," *Journal of the American Chemical Society*, vol. 137, no. 7, pp. 2548–2554, 2015.

[38] X. Bie, K. Kubota, T. Hosaka, K. Chihara, and S. Komaba, "A novel K-ion battery: hexacyanoferrate(II)/graphite cell," *Journal of Materials Chemistry A*, vol. 5, no. 9, pp. 4325–4330, 2017.

[39] Y. You, X.-L. Wu, Y.-X. Yin, and Y. G. Guo, "High-quality Prussian blue crystals as superior cathode materials for room-temperature sodium-ion batteries," *Energy and Environmental Science*, vol. 7, no. 5, pp. 1643–1647, 2014.

[40] X. Wu, C. Wu, C. Wei, L. Hu, J. Qian, Y. Cao, X. Ai, J. Wang, and H. Yang, "Highly Crystallized $Na_2CoFe(CN)_6$ with Suppressed Lattice Defects as Superior Cathode Material for Sodium-Ion Batteries," *ACS Applied Materials and Interfaces*, vol. 8, no. 8, pp. 5393–5399, 2016.

[41] M. Verdaguer and G. S. Girolami, "Magnetic prussian blue analogs," in *Magnetism: Molecules to Materials V* (J. S. Miller and M. Drillon, eds.), ch. 9, pp. 283–346, John Wiley & Sons, Ltd, 2004.

[42] N. Imanishi, T. Morikawa, J. Kondo, Y. Takeda, O. Yamamoto, N. Kinugasa, and T. Yamagishi, "Lithium intercalation behavior into iron cyanide complex as positive electrode of lithium secondary battery," *Journal of Power Sources*, vol. 79, no. 2, pp. 215–219, 1999.

[43] H.-W. Lee, R. Y. Wang, M. Pasta, S. Woo Lee, N. Liu, and Y. Cui, "Manganese hexacyanomanganate open framework as a high-capacity positive electrode material for sodium-ion batteries," *Nature Communications*, vol. 5, pp. 1–6, 2014.

[44] R. Chen, H. Tanaka, T. Kawamoto, M. Asai, C. Fukushima, H. Na, M. Kurihara, M. Watanabe, M. Arisaka, and T. Nankawa, "Selective removal of cesium ions

from wastewater using copper hexacyanoferrate nanofilms in an electrochemical system," *Electrochimica Acta*, vol. 87, pp. 119–125, 2013.

[45] R. Y. Wang, C. D. Wessells, R. A. Huggins, and Y. Cui, "Highly reversible open framework nanoscale electrodes for divalent ion batteries," *Nano Letters*, vol. 13, no. 11, pp. 5748–5752, 2013.

[46] P. Padigi, G. Goncher, D. Evans, and R. Solanki, "Potassium barium hexacyanoferrate - A potential cathode material for rechargeable calcium ion batteries," *Journal of Power Sources*, vol. 273, pp. 460–464, 2015.

[47] L. D. Reed, S. N. Ortiz, M. Xiong, and E. J. Menke, "A rechargeable aluminum-ion battery utilizing a copper hexacyanoferrate cathode in an organic electrolyte," *Chemical Communications*, vol. 51, no. 76, pp. 14397–14400, 2015.

[48] Z. Liu, G. Pulletikurthi, and F. Endres, "A Prussian Blue/Zinc Secondary Battery with a Bio-Ionic Liquid-Water Mixture as Electrolyte," *ACS Applied Materials and Interfaces*, vol. 8, no. 19, pp. 12158–12164, 2016.

[49] T. Matsuda, J. Kim, and Y. Moritomo, "Control of the alkali cation alignment in Prussian blue framework," *Dalton Transactions*, vol. 41, no. 25, pp. 7620–7623, 2012.

[50] A. Simonov, T. De Baerdemaeker, H. L. Boström, M. L. R. Gómez, H. J. Gray, D. Chernyshov, A. Bosak, H.-B. Bürgi, and A. L. Goodwin, "Hidden diversity of vacancy networks in Prussian blue analogues," *Nature*, vol. 578, no. 7794, pp. 256–260, 2020.

[51] Y. Moritomo, K. Igarashi, J. Kim, and H. Tanaka, "Size dependent cation channel in nanoporous prussian blue lattice," *Applied Physics Express*, vol. 2, no. 8, pp. 2–5, 2009.

[52] Y. Kurihara, T. Matsuda, and Y. Moritomo, "Structural Properties of Manganese Hexacyanoferrates against Li Concentration," *Japanese Journal of Applied Physics*, vol. 52, p. 17301, 2013.

[53] W. M. Haynes, ed., *CRC Handbook of Chemistry and Physics*, pp. 12–11—12–12. CRC Press, 2014.

[54] G. W. Beall, W. O. Milligan, J. Korp, and I. Bernal, "Crystal structure of $Mn_3[Co(CN)_6]_2 \cdot 12H_2O$ and $Cd_3[Co(CN)_6]_2 \cdot 12H_2O$ by Neutron and X-Ray Diffraction," *Inorganic Chemistry*, vol. 16, no. 11, pp. 2715–2718, 1977.

[55] F. Herren, A. Ludi, P. Fischer, and W. Halg, "Neutron Diffraction Study of Prussian Blue, $Fe_4[Fe(CN)_6]_3 \cdot xH_2O$ Location of Water Molecules and Long-Range Magnetic Order," *Inorganic Chemistry*, vol. 19, no. 4, pp. 956–959, 1980.

[56] X. Wu, J. J. Hong, W. Shin, L. Ma, T. Liu, X. Bi, Y. Yuan, Y. Qi, T. W. Surta, W. Huang, J. Neuefeind, T. Wu, P. A. Greaney, J. Lu, and X. Ji, "Diffusion-free Grotthuss topochemistry for high-rate and long-life proton batteries," *Nature Energy*, vol. 4, no. 2, pp. 123–130, 2019.

[57] J. Qian, C. Wu, Y. Cao, Z. Ma, Y. Huang, X. Ai, and H. Yang, "Prussian Blue Cathode Materials for Sodium-Ion Batteries and Other Ion Batteries," *Advanced Energy Materials*, vol. 8, no. 17, p. 1702619, 2018.

[58] W.-J. Li, C. Han, G. Cheng, S.-L. Chou, H.-K. Liu, and S.-X. Dou, "Chemical properties, structural properties, and energy storage applications of Prussian blue analogues," *Small*, vol. 15, no. 32, p. 1900470, 2019.

[59] Y. Xu, S. Zheng, H. Tang, X. Guo, H. Xue, and H. Pang, "Prussian blue and its derivatives as electrode materials for electrochemical energy storage," *Energy Storage Materials*, vol. 9, pp. 11–30, 2017.

[60] H. Kim, D. J. Kim, D. H. Seo, M. S. Yeom, K. Kang, D. K. Kim, and Y. Jung, "Ab initio study of the sodium intercalation and intermediate phases in $Na_{0.44}MnO_2$ for sodium-ion battery," *Chemistry of Materials*, vol. 24, no. 6, pp. 1205–1211, 2012.

[61] Y. Wang, W. D. Richards, S. P. Ong, L. J. Miara, J. C. Kim, Y. Mo, and G. Ceder, "Design principles for solid-state lithium superionic conductors," *Nature Materials*, vol. 14, no. 10, pp. 1026–1031, 2015.

[62] R. A. House, U. Maitra, M. A. Pérez-Osorio, J. G. Lozano, L. Jin, J. W. Somerville, L. C. Duda, A. Nag, A. Walters, K. J. Zhou, M. R. Roberts, and P. G. Bruce, "Superstructure control of first-cycle voltage hysteresis in oxygen-redox cathodes," *Nature*, vol. 577, no. 7791, pp. 502–508, 2020.

[63] A. Van der Ven, Z. Deng, S. Banerjee, and S. P. Ong, "Rechargeable alkali-ion battery materials: theory and computation," *Chemical Reviews*, vol. 120, no. 14, pp. 6977–7019, 2020.

[64] A. Urban, D. H. Seo, and G. Ceder, "Computational understanding of Li-ion batteries," *Computational Materials*, vol. 2, no. 1, 2016.

[65] A. F. Harper, M. L. Evans, J. P. Darby, B. Karasulu, C. P. Koçer, J. R. Nelson, and A. J. Morris, "Ab initio Structure Prediction Methods for Battery Materials: A review of recent computational efforts to predict the atomic level structure and bonding in materials for rechargeable batteries," *Johnson Matthey Technology Review*, vol. 64, no. 2, pp. 103–118, 2020.

[66] M. Nishino, S. Kubo, Y. Yoshioka, A. Nakamura, and K. Yamaguchi, "Theoretical studies on magnetic interactions in prussian blue analogs and active controls of spin states by external fields," *Molecular Crystals and Liquid Crystals Science*

and Technology. Section A. Molecular Crystals and Liquid Crystals, vol. 305, no. 1, pp. 109–128, 1997.

[67] M. Nishino, Y. Yoshioka, and K. Yamaguchi, "Effective exchange interactions and magnetic phase transition temperatures in Prussian blue analogs: a study by density functional theory," *Chemical Physics Letters*, vol. 297, pp. 51–59, 1998.

[68] J. C. Wojdeł and S. T. Bromley, "Efficient calculation of the structural and electronic properties of mixed valence materials: Application to Prussian Blue analogues," *Chemical Physics Letters*, vol. 397, no. 1-3, pp. 154–159, 2004.

[69] J. C. Wojdeł and S. T. Bromley, "From cluster calculations to molecular materials: A mixed pseudopotential approach to modeling mixed-valence systems," *Journal of Molecular Modeling*, vol. 11, no. 4-5, pp. 288–292, 2005.

[70] J. C. Wojdeł and S. T. Bromley, "Band gap variation in Prussian Blue via cation-induced structural distortion," *Journal of Physical Chemistry B*, vol. 110, no. 48, pp. 24294–24298, 2006.

[71] J. C. Wojdeł, I. D. P. R. Moreira, S. T. Bromley, and F. Illas, "Prediction of half-metallic conductivity in Prussian Blue derivatives," *Journal of Materials Chemistry*, vol. 19, no. 14, p. 2032, 2009.

[72] J. C. Wojdeł, "First principles calculations on the influence of water-filled cavities on the electronic structure of Prussian Blue," *Journal of Molecular Modeling*, vol. 15, no. 6, pp. 567–572, 2009.

[73] J. C. Wojdeł, I. D. P. Moreira, and F. Illas, "Periodic density functional theory study of spin crossover in the cesium iron hexacyanochromate Prussian blue analog," *Journal of Chemical Physics*, vol. 130, no. 1, 2009.

[74] C. Ling, J. Chen, and F. Mizuno, "First-principles study of alkali and alkaline earth ion intercalation in iron hexacyanoferrate: The important role of ionic radius," *Journal of Physical Chemistry C*, vol. 117, no. 41, pp. 21158–21165, 2013.

[75] P. Xiao, J. Song, L. Wang, J. B. Goodenough, and G. Henkelman, "Theoretical study of the structural evolution of a $Na_2FeMn(CN)_6$ cathode upon Na intercalation," *Chemistry of Materials.*, vol. 27, no. 10, pp. 3763–3768, 2015.

[76] F. S. Hegner, J. R. Galán-Mascarós, and N. López, "A Database of the Structural and Electronic Properties of Prussian Blue, Prussian White, and Berlin Green Compounds through Density Functional Theory," *Inorganic Chemistry*, vol. 55, no. 24, pp. 12851–12862, 2016.

[77] X. Guo, Z. Wang, Z. Deng, X. Li, B. Wang, X. Chen, and S. P. Ong, "Water contributes to higher energy density and cycling stability of prussian blue analogue cathodes for aqueous sodium-ion batteries," *Chemistry of Materials*, vol. 31, no. 15, pp. 5933–5942, 2019.

Chapter 2

Methods: simulating batteries with density-functional theory

2.1 Density-functional theory in context: time and length scales

This chapter details density-functional theory (DFT) as a method generally and as a tool for modeling batteries specifically. For context, the time and length scales addressed by DFT are shown alongside the scales of other theoretical methods used in materials science for energy storage in Figure 2.1. DFT is an ab-initio theory, or a theory from first principles [1, 2]. It makes appropriate approximations to fundamental quantum-mechanical laws like the Schrödinger and Dirac equations to predict properties of materials. Its aim is to make predictions without the input of experimental parameters, making it a bottom-up approach.

This chapter begins with a development of the Kohn–Sham equations, starting from the time-independent many-body Schrödinger equation. The equations are then extended to the case of spin DFT for magnetic systems and some practical considerations for planewave representation are discussed. Then, the exchange-and-correlation functional is discussed in detail and the failure of local functionals in strongly correlated systems is described. The theory of hybrid functionals and DFT+U, which are two advanced, DFT-based methods that can deal with strongly correlated sys-

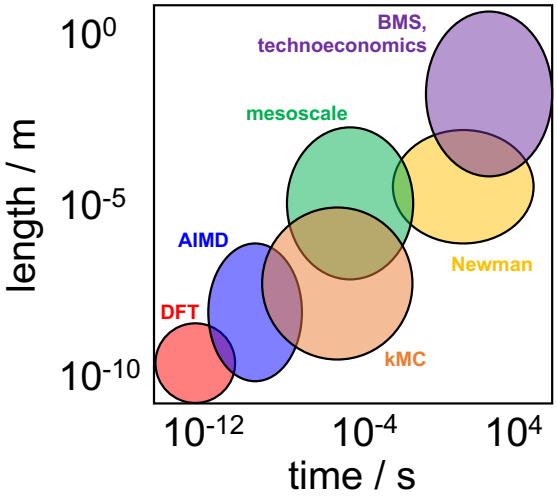

Figure 2.1: Time and length scales of different battery theories. Also shown are ab-initio molecular dynamics (AIMD), kinetic Monte Carlo (kMC), mesoscale models of particles' mechanical properties (mesoscale), the Newman method within continuum mechanics (Newman), and pack-level, battery management systems software (BMS) and technoeconomic analyses (technoeconomics). The limits of the theories are approximate.

tems, is then developed. Finally, mathematical procedures are introduced to bridge DFT's ground-state electronic density and total energy with battery properties like ground-state crystal structure, voltage, and density of states. This chapter is a succinct introduction to the state of the art in first-principle modeling for batteries, and it will be a useful reference for researchers starting calculations on the PBAs or other strongly correlated systems.

2.2 The algorithm for spin-density-functional theory

The aim of this section is to develop the Kohn–Sham equations, a set of simultaneous differential equations that are solved iteratively to achieve self-consistency in DFT. The equations are also extended to account for electron spin. Finally, the planewave representation of DFT is explained and a few relevant practical elements are considered.

2.2.1 The many-body Schrödinger equation

Materials are a collection of electrons and nuclei. Electrons are light enough that they require quantum mechanics to be described accurately. All information about a quantum-mechanical system composed of multiple particles is encoded in the system's wavefunction [3]. Strictly, the wavefunction is a function of the position or positions of a system's particles as well as time. But the ground-state electronic density and total energy (as well as many others of interest) are time-independent properties. This is because the Coulombic potential-energy operator does not vary in time. Throughout this work, the potential energy is not time varying, so it suffices to find the so-called stationary states of a system. (Note that in Chapter 5 spectroscopic properties are considered which necessarily involve interactions with the time-varying electromagnetic field. It is still sufficient to consider stationary states, though, since the relaxation time for perturbations of electrons is much faster than atomic vibration.) So I consider the many-body wavefunction, Ψ, which is a function of the electronic and nuclear coordinates, $\mathbf{r}_i$ and $\mathbf{R}_I$, respectively, as

$$\Psi = \Psi(\mathbf{r}_1, \mathbf{r}_2, ..., \mathbf{r}_N; \mathbf{R}_1, \mathbf{R}_2, ..., \mathbf{R}_M). \tag{2.1}$$

The ground-state total energy is related to the many-body wavefunction by the time-independent, many-body Schrödinger equation [4]

$$\hat{H}\Psi = E_{\text{total}}\Psi \tag{2.2}$$

in which E_{total} is the system's total energy and $\hat{H}$ is the Hamiltonian operator: the sum of the kinetic- ($\hat{T}$) and potential- ($\hat{V}$) energy operators, $\hat{H} = \hat{T} + \hat{V}$.

Substituting the standard form of the kinetic-energy operator and writing the potential-energy operator as the electrostatic potential energy [5] between pairs of nuclei with mass M_I and atomic number Z_I, pairs of electrons, and nucleus-electron

pairs, I write (in atomic units)

$$\left[-\sum_i \frac{\nabla_i^2}{2} - \sum_I \frac{\nabla_I^2}{2M_I} - \frac{1}{2}\sum_{I\neq J} \frac{Z_I Z_J}{|\mathbf{R}_I - \mathbf{R}_J|} - \sum_{i,I} \frac{Z_I}{|\mathbf{r}_i - \mathbf{R}_I|} - \frac{1}{2}\sum_{i\neq j} \frac{1}{|\mathbf{r}_i - \mathbf{r}_j|}\right] \Psi = E_{\text{total}}\Psi. \quad (2.3)$$

At this point, I make the clamped-nuclei approximation. This is generally a good approximation for molecules and extended solids. I take the limit of equation 2.3 as M_I go to infinity. The nuclear kinetic energy term goes to zero. I also make the following two definitions. First, subtracting off the constant contribution of the nucleus-nucleus potential energies, I define

$$E = E_{\text{total}} - \frac{1}{2}\sum_{I\neq J} \frac{Z_I Z_J}{|\mathbf{R}_I - \mathbf{R}_J|} \quad (2.4)$$

and I write the potential energy between nuclei and electrons as

$$V_{\text{n}}(\mathbf{r}) = -\sum_I \frac{Z_I}{|\mathbf{r} - \mathbf{R}_I|}. \quad (2.5)$$

This allows me to regard the nuclear coordinates as external parameters and to write the problem in terms of the electronic positions only, as

$$\left[-\sum_i \frac{\nabla_i^2}{2} + \sum_i V_{\text{n}}(\mathbf{r}_i) - \frac{1}{2}\sum_{i\neq j} \frac{1}{|\mathbf{r}_i - \mathbf{r}_j|}\right] \Psi(\mathbf{r}_1, \mathbf{r}_2, ..., \mathbf{r}_N) = E\Psi(\mathbf{r}_1, \mathbf{r}_2, ..., \mathbf{r}_N). \quad (2.6)$$

This is the fundamental equation for electronic-structure theory [6], and all of electronic-structure theory is as simple as solving equation 2.6 for a given arrangement of nuclei. This problem is intractably difficult for essentially everything more complicated than the hydrogen molecule.

2.2.2 The Hohenberg and Kohn Theorem

While equation 2.6 must be solved for Ψ to determine a quantum mechanical property of a system in general, it is *not* necessary to know the exact form of Ψ for the special

case in which the property of interest is the ground-state energy. Fortunately, this is exactly the property that governs many important materials properties like crystal geometry. It can be shown that the ground-state energy is a unique functional of the ground-state electronic density, $n(\mathbf{r})$. This result is due to Hohenberg and Kohn and is appropriately called the Hohenberg and Kohn Theorem [7]. A "functional" is a mathematical object that takes as input a function and returns a number. The name "density-functional theory" refers to the fact that the ground-state energy is a unique functional of the electronic density.

Briefly, the proof is organized into three parts. First, the ground-state electronic density, $n(\mathbf{r})$, uniquely determines the nuclear potential, V_{n}. Second, the nuclear potential uniquely determines the wavefunction, Ψ. Third, the wavefunction uniquely determines the total energy. If all three hold, then the total ground-state energy is a unique functional of the ground-state electronic density. The third statement is a phrasing of the fact that the total energy of the ground state is defined by $E = \langle\Psi|\hat{H}|\Psi\rangle$. The second statement can be understood by inspecting equation 2.3. It simply means that the identical arrangements of identical elements will have identical wavefunctions, and moving any ions will change the wavefunction. The first statement is somewhat more subtle. Hohenberg and Kohn showed it by contradiction, assuming that two different nuclear potentials, V_{n} and V'_{n}, with two different energies, E and E', can both produce the same ground-state electronic density. This leads to a false conclusion, so it must be that there is no such other potential V'_{n}, which completes the proof.

2.2.3 The Kohn–Sham equations

The problem of finding the ground-state total energy has now been simplified from a hunt for the electrons' many-body wavefunction, $\Psi(\mathbf{r}_1, \mathbf{r}_2, ..., \mathbf{r}_N)$, a function of $3N$ variables, to the hunt for $n(\mathbf{r})$, a function of only 3 variables. If $n(\mathbf{r})$ is known, the

total energy can be written as a functional, F of n, as

$$E = F[n] = \int d\mathbf{r}\, n(\mathbf{r}) V_{\mathrm{n}}(\mathbf{r}) + \langle \Psi[n] | \hat{T} + \hat{W} | \Psi[n] \rangle \tag{2.7}$$

in which $\hat{W}$ is the operator for the Coulomb potential energy between electron pairs. To determine n, I next assume the electrons are independent and group the error this causes into a new term. In the independent-electron assumption, the wavefunction of the i^{th} electron is written ϕ_i. The electrons do not "see" each other, which allows us to disregard the electron-electron repulsion term that made solution of equations 2.3 and 2.6 intractably difficult. Including only the Hartree potential, which is the potential each electron experiences in the average electrostatic field arising from the total electronic density, I write

$$E = F[n] = \int d\mathbf{r} n(\mathbf{r}) V_{\mathrm{n}}(\mathbf{r}) - \sum_i \int d\mathbf{r} \phi_i^*(\mathbf{r}) \frac{\nabla^2}{2} \phi_i(\mathbf{r}) + \frac{1}{2} \int d\mathbf{r} \int d\mathbf{r}' \frac{n(\mathbf{r}) n(\mathbf{r}')}{|\mathbf{r} - \mathbf{r}'|} + E_{\mathrm{xc}}[n]. \tag{2.8}$$

The first term is the external, nuclear potential, the second term is the kinetic energy, the third term is the Hartree potential, and the fourth term is the energy left over. It is called the exchange-and-correlation energy because it arises from energy associated with the "exchange" of identical, quantum-mechanical particles (more specifically, fermions) and with the "correlated" behavior of electrons (that is, their "non-independence" in some sense).

Equation 2.8 gives us an expression for the energy as a functional of the electronic density. The method of actually determining the ground-state electronic density relies first on a variation principle, which states that the ground-state electronic density is whatever function minimizes the total energy. In the parlance of functional derivatives, it is required that

$$\left. \frac{\delta F[n]}{\delta n} \right|_{n_0} = 0. \tag{2.9}$$

Further requiring that the wavefunctions be orthonormal, I write

$$\left[-\frac{1}{2} \nabla^2 + V_{\mathrm{n}}(\mathbf{r}) + V_{\mathrm{H}}(\mathbf{r}) + V_{\mathrm{xc}}(\mathbf{r}) \right] \phi_i(\mathbf{r}) = \epsilon_i \phi_i(\mathbf{r}). \tag{2.10}$$

```
def dft():
     read in nuclear coordinates and atomic numbers
     evaluate the nuclear potential
     make an initial guess at the electron density
     while the electron density is not converged:
          calculate the Hartree potential
          calculate the exchange and correlation potential
          solve the Schrödinger equation for the wavefunctions
          calculate the new electron density
     calculate the total energy
```

Figure 2.2: Pseudocode for DFT. The figure shows the algorithm for self-consistently determining the ground state electron density, n (blue), given the nuclear potential, $V(\mathbf{R}_I)$ (red). The Hartree potential, $V_{\mathrm{H}}(\mathbf{r})$ (green), and the exchange-and-correlation potential, $V_{\mathrm{xc}}(\mathbf{r})$ (gold) must be evaluated on each iteration before the Kohn–Sham single-particle wavefunctions, ϕ_i (pink) can be determined.

The equations defined by 2.10 are the Kohn–Sham equations [8], and they are a huge simplification of the problem. They can be solved in an iterative fashion from some initial guess at the electronic density until self-consistency is achieved. For reference, the simultaneous equations are written out as equations 2.11 to 2.16, and pseudocode explaining the algorithm to solve them is shown in Figure 2.2.

$$\left[-\frac{1}{2}\nabla^2 + V_{\mathrm{tot}}(\mathbf{r})\right]\phi_i(\mathbf{r}) = \epsilon_i\phi_i(\mathbf{r}) \tag{2.11}$$

$$V_{\mathrm{tot}}(\mathbf{r}) = V_{\mathrm{n}}(\mathbf{r}) + V_{\mathrm{H}}(\mathbf{r}) + V_{\mathrm{xc}}(\mathbf{r}) \tag{2.12}$$

$$V_{\mathrm{n}}(\mathbf{r}) = -\sum_I \frac{Z_I}{|\mathbf{r} - \mathbf{R}_I|} \tag{2.13}$$

$$\nabla^2 V_{\mathrm{H}}(\mathbf{r}) = -4\pi n(\mathbf{r}) \tag{2.14}$$

$$V_{\mathrm{xc}}(\mathbf{r}) = \frac{\delta E_{\mathrm{xc}}[n]}{\delta n}(\mathbf{r}) \tag{2.15}$$

$$n(\mathbf{r}) = \sum_i |\phi_i(\mathbf{r})|^2 \tag{2.16}$$

2.2.4 Extending DFT to include electron spin

As discussed in Chapter 3, spin configuration is an interesting and important phenomenon in the PBAs. Spin is an intrinsic property of all electrons that gives rise to a measurable angular momentum and magnetic moment [9]. The development of spin DFT is analogous to the development of DFT. It begins with the relativistic extension of Schrödinger's equation, the Dirac equation [10], proceeding through von Barth and Hedin's proof [11], in analogy with the Hohenberg and Kohn Theorem, that in the spin-polarized case the total ground-state energy is a unique functional of the ground-state electronic density and the spin density, $\mathbf{s}(\mathbf{r})$. Detailed treatment of magnetism and spin can be found in references [12] and [13], but the counterparts of the Kohn–Sham equations that result for spin DFT are

$$\left[-\frac{1}{2}\nabla^2 + V_{\mathrm{n}}(\mathbf{r}) + V_{\mathrm{H}}(\mathbf{r})\right]\phi_i(\mathbf{r};\alpha) + \sum_{\beta} v^{\mathrm{xc}}_{\alpha\beta}(\mathbf{r})\phi_i(\mathbf{r};\beta) = \epsilon_i\phi_i(\mathbf{r};\alpha) \tag{2.17}$$

$$V_{\mathrm{n}}(\mathbf{r}) = -\sum_{I}\frac{Z_I}{|\mathbf{r}-\mathbf{R}_I|} \tag{2.18}$$

$$\nabla^2 V_{\mathrm{H}}(\mathbf{r}) = -4\pi n(\mathbf{r}) \tag{2.19}$$

$$v^{\mathrm{xc}}_{\alpha\beta}(\mathbf{r}) = \frac{\delta E_{xc}[n_{\alpha\beta}]}{\delta n_{\alpha\beta}}(\mathbf{r}) \tag{2.20}$$

$$n_{\alpha\beta}(\mathbf{r}) = \sum_{i}\phi^*_i(\mathbf{r};\alpha)\phi_i(\mathbf{r};\beta) \tag{2.21}$$

$$n(\mathbf{r}) = \sum_{\alpha} n_{\alpha\alpha}(\mathbf{r}) \tag{2.22}$$

Many quantities remain unchanged, but several new quantities have been introduced. First, the single-particle wavefunctions, ϕ, are now a function of a spin coordinate, α. Second, the equations include the density matrix, $n_{\alpha\alpha}$. This matrix encodes both the electronic density, n, by equation 2.22 and the spin density, $\mathbf{s}(\mathbf{r})$. Heuristically, one can think of the quantity $\mathbf{s}(\mathbf{r})d\mathbf{r}$ as the magnetic moment of an infinitesimal volume of space $d\mathbf{r}$. It is given by

$$\mathbf{s}(\mathbf{r}) = \frac{1}{2}\sum_{\alpha\beta} n_{\alpha\beta}(\mathbf{r})\boldsymbol{\sigma}_{\alpha\beta} \tag{2.23}$$

in which $\boldsymbol{\sigma}_{\alpha\beta} = \sigma^x_{\alpha\beta}\hat{\mathbf{x}} + \sigma^y_{\alpha\beta}\hat{\mathbf{y}} + \sigma^z_{\alpha\beta}\hat{\mathbf{z}}$ for the Pauli matrices

$$\sigma^x = \begin{bmatrix} 0 & 1 \\ 1 & 0 \end{bmatrix}, \sigma^y = \begin{bmatrix} 0 & -i \\ i & 0 \end{bmatrix}, \sigma^z = \begin{bmatrix} 1 & 0 \\ 0 & -1 \end{bmatrix} \tag{2.24}$$

in which i is the imaginary unit. Finally, the exchange-and-correlation potential, $v^{\text{xc}}_{\alpha\beta}$, is a matrix performing essentially the same function as V_{xc}.

All spin-DFT calculations in this work are collinear. That is, I make the approximation that the electron-spin vectors are orientable in one direction.

2.2.5 Planewaves, reciprocal space, and pseudopotentials

From Bloch's Theorem [14] it is known that the wavefunction for an electron in a periodic potential (like, for instance, a crystalline arrangement of ions) must satisfy

$$\phi_{\nu\mathbf{k}} = e^{i\mathbf{k}\cdot\mathbf{r}} u_{\mathbf{k}}(\mathbf{r}) \tag{2.25}$$

in which ν is the band index, $\mathbf{k}$ is the electron's wavevector, and $u_{\mathbf{k}}(\mathbf{r})$ is a periodic function with the same period as the potential. The function $u_{\mathbf{k}}(\mathbf{r})$ can be expanded in a set of planewaves as

$$u_{\mathbf{k}}(\mathbf{r}) = \sum_{\mathbf{G}} c_{\mathbf{G}} e^{i\mathbf{G}\cdot\mathbf{r}}. \tag{2.26}$$

In DFT, this is called a planewave representation, and it is a natural choice for modeling the unit cell of an extended, crystalline solid with periodic boundary conditions. Combining equations 2.25 and 2.26 gives

$$\phi_{\nu\mathbf{k}} = \sum_{\mathbf{G}} c_{\mathbf{G}} e^{(\mathbf{G}+\mathbf{k})\cdot\mathbf{r}}. \tag{2.27}$$

The vectors $\mathbf{G}$ in equations 2.26 and 2.27 are the lattice vectors in reciprocal space. For a lattice spanned by the vectors $\mathbf{a_1}$, $\mathbf{a_2}$, and $\mathbf{a_3}$, the reciprocal lattice vectors, $\mathbf{b_i}$, are given by [15, 16]

$$\mathbf{b_1} = 2\pi \frac{\mathbf{a_2} \times \mathbf{a_3}}{\mathbf{a_1} \cdot (\mathbf{a_2} \times \mathbf{a_3})},\ \mathbf{b_2} = 2\pi \frac{\mathbf{a_3} \times \mathbf{a_1}}{\mathbf{a_2} \cdot (\mathbf{a_3} \times \mathbf{a_1})},\ \mathbf{b_3} = 2\pi \frac{\mathbf{a_1} \times \mathbf{a_2}}{\mathbf{a_3} \cdot (\mathbf{a_1} \times \mathbf{a_2})}. \tag{2.28}$$

The set of vectors $\mathbf{G}$ are defined by the points $m_1\mathbf{b_1} + m_2\mathbf{b_2} + m_3\mathbf{b_3}$ for integer values of m_i. To be exact, the summation in equation 2.26 is taken over an infinite number of $\mathbf{G}$ vectors. Obviously, this is impossible, so a kinetic-energy cutoff is specified when running calculations and only those $\mathbf{G}$ vectors with a kinetic energy

$$E(\mathbf{G}) = \frac{|\mathbf{G}|^2}{2} \tag{2.29}$$

that is less than the cutoff are included in the sum. Furthermore, the wavevectors $\mathbf{k}$ in equation 2.25 are, in fact, points in reciprocal space. In practice, multiple $\mathbf{k}$ points in the first Brillouin zone are specified in DFT calculations.

The problem of solving the Kohn–Sham equations in a planewave representation has become a problem of solving for the matrix of coefficients in equation 2.27. This is usually done with a Fourier transform and algorithms that efficiently diagonalize matrices [17].

For completeness, planewaves are not the only sensible choice for expanding the Kohn–Sham wavefunctions. Real-space representations [18] and atomic orbitals [19] are other reasonable choices. Atomic orbitals in particular can have certain advantages over the planewave representation, especially for isolated molecules. All calculations in this work are carried out using planewaves.

One drawback of the planewave representation is that it requires very high energy cutoffs to accurately represent wavefunctions that oscillate with a small wavelength in real space. And this is precisely the behavior for core electrons. This is doubly unfortunate, because these electrons are less important that the valence electrons involved in chemical bonding and many materials properties. One strategy to avoid the computational cost of modeling these tightly bound electrons is the use of pseudopotentials [20]. A pseudopotential is a description of the behavior, especially the screening effect, of the core electrons. The benefit of pseudopotentials is that they reduce the total number of electrons that have to be simulated, reducing the amount

of computational memory and time needed to solve the Kohn–Sham equations. The main disadvantage to the use of pseudopotentials is that they require semiempirical parameters to capture the nature of the core electrons, and at least one unique pseudopotential has had to be developed for every element. However, the pseudopotential for a given element is usually usable for any crystal structure. And by now, high-performing and highly transferable pseudopotentials have been developed for basically every element. Reference [21] details the field of pseudopotential development.

2.3 Functionals for strongly correlated systems

This section discusses the exchange-and-correlation functionals used in later chapters and why they are appropriate to modeling the PBA electronic structure. While the Hohenberg and Kohn Theorem guarantees the existence of the exact functional mapping from the ground-state electronic density to the ground-state energy, it does not provide for how to determine the functional. All functionals used in practice are approximations, and the hunt for a fast, accurate, and widely (or even universally) applicable functional is one of the great open questions of modern materials science [22]. First, conventional DFT functionals are introduced, using the local-density approximation (LDA) as an example. The problem of electron self-interaction is then introduced. Finally, two functionals are discussed that have seen great success in overcoming spurious self-interaction in related materials. These methods are DFT+U and hybrid functionals.

2.3.1 The local-density approximation

The first and simplest exchange-and-correlation functional of DFT is that developed under the LDA. This approximation concerns the homogeneous electron gas, a model very closely related to the free electron gas (FEG) of elementary solid-state physics [16]. The added feature relative to the FEG is electron repulsion. The exchange

energy for the homogeneous electron gas is exactly [23]

$$E_{\mathrm{x}}[n(\mathbf{r})] = -\frac{3}{4}\left(\frac{3}{\pi}\right)^{1/3} n^{4/3}(\mathbf{r}). \tag{2.30}$$

The correlation energy, in contrast, cannot be written analytically for even this simplest system. It has been calculated by Monte Carlo methods [24] and parameterized as [25]

$$E_{\mathrm{c}} = nV \cdot \begin{cases} -0.0480 + 0.0311\ln(r_s) - 0.0116 r_s + 0.002 r_s \ln(r_s) & r_s < 1 \\ \dfrac{-0.1423}{1 + 1.0529\sqrt{r_s} + 0.3334 r_s} & r_s \geq 1 \end{cases} \tag{2.31}$$

in which r_s is the Wigner-Seitz radius, the radius of the sphere occupied by each electron on average, given by

$$\frac{V}{N} = \frac{4\pi}{3} r_s^3 = \frac{1}{n}. \tag{2.32}$$

A simple extension to LDA which increases its accuracy in some important cases is writing the functional in terms of the gradient of the local electronic density as well. That is, $E_{\mathrm{xc}} = E_{\mathrm{xc}}[n(\mathbf{r}), \nabla n(\mathbf{r})]$. This extension is called the generalized-gradient assumption (GGA). Despite the simplicity of the LDA and GGA, they are the basis for the overwhelming majority of functionals used in modern DFT. The functional due to Perdew, Burke, and Ernzerhof (PBE) [26] and extensions of it are used throughout this work.

2.3.2 Self-interaction and over-delocalization in strongly correlated systems

Self-interaction is a consequence of separating the electronic potential into a classical part (the Hartree potential of equation 2.14) and everything else (the exchange-and-correlation potential). Because the electron interacts with the electrostatic field, an electron in DFT can repel itself, which is obviously unphysical. A clear and dramatic example is Pople's observation that a functional within the LDA incorrectly predicts

the molecule H_3 to be stable relative to H and H_2 [27]. There should be absolutely no electron repulsion on H, since it has exactly one electron, but the model has a non-zero Hartree potential. Self-interaction also destabilizes highly localized orbitals to minimize self-interaction. The leads to, for example, over-delocalization of electrons in d orbitals of transition metals [28]. Materials that contain multiple electrons in these kinds of highly localized states are called strongly correlated.

2.3.3 A hybrid function

Hartree–Fock theory is a wavefunction-based method in quantum chemistry. Within Hartree–Fock, the self-interaction error introduced by the Hartree potential is precisely canceled by the exchange energy given by [3]

$$E_{\mathrm{X}}^{\mathrm{HF}} = -\frac{1}{2}\sum_{i}\sum_{j}\int d\mathbf{r}\int d\mathbf{r}'\frac{\phi_i^*(\mathbf{r})\phi_j^*(\mathbf{r}')\phi_j(\mathbf{r})\phi_i(\mathbf{r}')}{|\mathbf{r}-\mathbf{r}'|} \tag{2.33}$$

in which the ϕ_i are single-particle wavefunctions. Hartree–Fock theory gives an exact value for the exchange energy where the LDA and GGA give only an approximation.

The hybrids are a class of functional that mix a portion of the non-local Hartree–Fock exact exchange with a local approximation (from, for instance, LDA or GGA) [29, 30]. The hybrid functional due to Heyd, Scuseria, Ernzerhof (HSE) [31] is defined by

$$E_{\mathrm{xc}}^{\omega\mathrm{PBEh}} = aE_{\mathrm{x}}^{\mathrm{HF,SR}}(\omega) + (1-a)E_{\mathrm{x}}^{\mathrm{PBE,SR}}(\omega) + E_{\mathrm{x}}^{\mathrm{PBE,LR}}(\omega) + E_{\mathrm{c}}^{\mathrm{PBE}} \tag{2.34}$$

in which SR and LR are short- and long-range contributions, respectively. The value a is the mixing fraction and ω is the range-separation parameter. It characterizes how fast short-range interactions become negligible. Throughout this work I use HSE06 [32] for which $a = 0.25$ and $\omega = 0.2$ Å^{-1}.

The great advantage of hybrid functionals is that they allow strongly correlated materials to be modeled purely ab initio. Critically, though, they are *non-local*. That is, equation 2.33 involves evaluating an integral over the additional variable, $\mathbf{r}'$. This

significantly increases the time and memory required to perform DFT calculations with hybrid functionals.

2.3.4 The Hubbard model and DFT+U

Another strategy to overcome self-interaction is DFT+U [33, 34]. In DFT+U, an energetic penalty determined by the parameter U is added to partially occupied orbitals, driving the system to localize electrons. The Hamiltonian is based on Hubbard's model of a lattice with onsite repulsion [35–37], so the parameter is called the Hubbard U. The DFT functional is modified according to [38]

$$E_{\mathrm{DFT+U}} = E_{\mathrm{DFT}} + \sum_{l} \left[\frac{U^l}{2} \sum_{m,\sigma \neq m',\sigma'} n_m^{l\sigma} n_{m'}^{l\sigma'} - \frac{U^l}{2} n^l (n^l - 1) \right] \tag{2.35}$$

in which E_{DFT} is the underlying LDA or GGA, l and m are the orbital and magnetic quantum numbers, respectively, σ is the spin coordinate, and n is the orbital's occupation. The second term is the Hubbard-model penalization of partially occupied orbitals while the third term subtracts those electronic interactions from E_{DFT} where they are already counted. It is appropriately called the double-counting term.

A first-order approximation to the rotationally invariant form of equation 2.35

$$E_{\mathrm{DFT+U}} = \sum_{l,\sigma} \frac{U^l}{2} \mathrm{Tr}[\mathbf{n}^{l\sigma}(1 - \mathbf{n}^{l\sigma})]. \tag{2.36}$$

where $\mathbf{n}$ is now an (m x m) matrix of orbital occupations and Tr represents a matrix's trace. Equation 2.36 is the form of the equation as commonly implemented in DFT codes.

The great advantage of DFT+U is that its time and memory requirements are insignificantly greater than those of DFT. Its main disadvantage is that it requires the parameter U as input. This must be parameterized by comparison to experiment or to results from more advanced, purely ab-initio methods. Some groups have had success calculating U from first principles by linear-response theory [39].

To conclude, I reemphasize that the transition-metal oxides are almost the prototypical material family in which DFT can fail because of over-delocalization of *d*-orbital electrons. But these are exactly some of the most relevant compounds for battery electrodes. Ceder and coworkers have shown the improvement over conventional functionals by hybrids [40] and DFT+U [41] in these compounds by minimizing self-interaction error.

In this section, the conventional DFT functionals within the LDA and GGA are discussed. Self-interaction error introduced by the Hartree potential in the Kohn–Sham equations is not completely canceled by these approximate functionals. Advanced, DFT-based methods including hybrid functionals and DFT+U are necessary to accurately model strongly correlated systems. This work demonstrates the need for these methods in simulating the PBAs.

2.4 From total energy and electronic density to materials properties

As discussed above, the main outputs of DFT are the ground-state electronic density and the ground-state total energy. This section discusses six mathematical processes by which these outputs (along with the final Kohn–Sham single-particle wavefunctions) are used to predict materials properties relevant to batteries. Those properties are the equilibrium crystal structure, formation energy of a chemical phase, electrochemical reduction potential, activation energy for ion movement, electronic density of states, and the projection of the charge density onto atomic orbitals. These properties are chosen because they are particularly common or important throughout the work.

2.4.1 Relaxation of the crystal geometry

Determining the ground-state crystal structure of a material is among the most important applications of DFT. It is so important that implementations of DFT commonly automate the procedure of finding the ground-state ion positions iteratively. It can be shown that the forces acting on the ions are given by [1]

$$\mathbf{F}_I = -\frac{\partial U}{\partial \mathbf{R}_I} \tag{2.37}$$

where $U = U(\mathbf{R}_I)$ is the total energy experienced by the nuclei, including contributions from their mutual repulsion and attraction to the electrons. The mapping U is the potential-energy surface. From equation 2.37 it is obvious that the equilibrium ion positions are the stationary points on the potential-energy surface. An impressive quantum-mechanical result due to Hellmann and Feynman is that the forces can also be written as [42, 43]

$$\mathbf{F}_I = Z_I \left[\nabla V_{\mathrm{H}}(\mathbf{R}_I) - \sum_{J \neq I} Z_J \frac{\mathbf{R}_J - \mathbf{R}_I}{|\mathbf{R}_J - \mathbf{R}_I|^3} \right]. \tag{2.38}$$

This result is striking because a fully quantum-mechanical treatment gives an expression for the forces on the ions that can be understood in terms of two classical fields: electron attraction and nuclear repulsion. This result is useful because a single DFT run allows for the calculation of ionic forces. Relaxation is performed iteratively (with the DFT process of Figure 2.2 essentially wrapped in an outer, ionic loop) using an optimization algorithm, like the quasi-Newtonian [44] or conjugate-gradient algorithm [45].

2.4.2 Formation energies and chemical phase stability

The formation energy is the relevant thermodynamic property for determining whether a chemical compound is stable relative to other nearby compositions. For conventional

transition-metal oxides, $\mathrm{Li}_x M\mathrm{O}_2$, I can consider the energy of their formation from the fully delithiated ($x = 0$) and fully lithiated ($x = 1$) compounds as [46]

$$E_\mathrm{f}(\mathrm{Li}_x M\mathrm{O}_2) = E(\mathrm{Li}_x M\mathrm{O}_2) - xE(\mathrm{Li}M\mathrm{O}_2) - (1-x)E(M\mathrm{O}_2). \tag{2.39}$$

There are other electrodes, like phosphorus, which alloy with lithium and sodium. For a binary mixture, $A_a B_b$, the formation energy is written as [47]

$$E_\mathrm{f}(A_a B_b) = \frac{E(A_a B_b) - aE(A) - bE(B)}{a+b}. \tag{2.40}$$

Equations 2.39 and 2.40 can be shown to be equivalent by setting $A = \mathrm{Li}M\mathrm{O}_2$, $B = M\mathrm{O}_2$, $a = x$, and $b = (1-x)$. So the denominator $a + b = x + (1-x) = 1$ is unity. The energies in equations 2.39 and 2.40 are the DFT total energies. The formation energies of the chemically stable phases form the convex hull when plotted versus x. Finally, I note that this discussion addresses binary mixtures, but it is possible to consider more decomposition products in a higher-dimensional space of chemical compositions.

2.4.3 Reduction potential

The reduction potential of an electrode is calculable from the DFT. Rearranging equation 1.4 and approximating the Gibbs free energy by the DFT total energy, the average voltage, V, for the insertion of an amount $x_2 - x_1$ of sodium into $\mathrm{Fe[Fe(CN)_6]}$ (for example) can be written as [48]

$$V(x_1, x_2) = \frac{E(\mathrm{Na}_{x_2}\mathrm{Fe[Fe(CN)_6]}) - E(\mathrm{Na}_{x_1}\mathrm{Fe[Fe(CN)_6]}) - (x_2 - x_1)E(\mathrm{Na})}{e(x_2 - x_1)} \tag{2.41}$$

in which e is the fundamental charge and $E(\mathrm{Na})$ is the energy of sodium in some reference phase. Throughout this work, the reference phase is the metallic form of the inserting alkali-metal ion. In experimental electrochemistry, the voltage is often reported as a function of the charge, or capacity, passed to the electrode under conditions of constant current, i. (The usefulness of this format is evident from equation 1.6). These are known as galvanostatic conditions [49].

2.4.4 Activation energy for ion movement

Diffusivity and ionic conductivity for crucial parameters for understanding and improving electrode kinetics. These properties follow Arrhenius-type relations as [50]

$$D = D_0 e^{\frac{E_\mathrm{a}}{k_\mathrm{B}T}} \tag{2.42}$$

in which D is the diffusivity, D_0 is a limiting diffusivity, and E_a is a characteristic activation energy for the movement of an ion from one lattice site to another. The activation energy is calculable from first principles using the nudged elastic band (NEB) method [51, 52].

Within NEB, finding E_a is framed as finding the minimum-energy path, M, between two stationary points on the potential-energy surface. That is, NEB minimizes the function

$$M(\mathbf{r}_1, \mathbf{r}_2, ..., \mathbf{r}_P) = \sum_{i=1}^{P-1} E(\mathbf{r}_i) + \sum_{i=1}^{P} \frac{1}{2} K(\mathbf{r}_i - \mathbf{r}_{i-1})^2 \tag{2.43}$$

in which $\mathbf{r}_i$ are a set of ion positions, called images, E is the total energy, and K is a spring constant that prevents the images from simply sliding down to the stationary points. Within NEB, it is further required that ions only be allowed to relax within the hyperplane normal to the tangent of the local path, $\hat{\tau}$. Meanwhile, only the component of the spring force that is parallel to the path is considered.

2.4.5 Electronic densities of states

The electronic density of states, ρ, for a system is a measure of the number of Kohn–Sham states with energy eigenvalues inside some energy interval. It is given by [16]

$$\rho(E) = \sum_{\nu} \int_{\mathrm{BZ}} \frac{d\mathbf{k}}{\Omega_{\mathrm{BZ}}} \delta(E - \epsilon_{\nu\mathbf{k}}) \tag{2.44}$$

in which the integral is taken over the whole first Brillouin zone, BZ (although in practical calculations this is a sum over the finite number of $\mathbf{k}$ points), Ω_{BZ} is the volume of the first Brillouin zone, and the sum is taken over all bands. In a plot of

the density of states versus energy, the states can be divided into two regions: one of occupied states and one of unoccupied states. The two regions are divided at the Fermi energy, ϵ_{F}, given by [16]

$$\int_{-\infty}^{\epsilon_{\mathrm{F}}} \rho(E) dE = N \tag{2.45}$$

in which N is the total number of electrons in the system. The Fermi level and the density of states are extremely important to the study of electronic structure. For example, whether or not a material conducts electrons like a metal can be determined by checking if there are states at the Fermi level. Chapter 3 explores exactly this question for nine important PBAs.

2.4.6 Projection onto atomic orbitals

It is often useful to examine the electronic charge density or spin density arising from (or localized to) atomic orbitals. The planewave state $|\phi_{\nu\mathbf{k}}\rangle$ with band index ν at k-point $\mathbf{k}$ can be projected onto the l atomic orbital of atom α by [53]

$$n_{\alpha l} = \frac{1}{N_{\mathbf{k}}} \sum_{\nu\mathbf{k}} f_{\nu\mathbf{k}} |\langle Y_{ml}^{\alpha} | \phi_{\nu\mathbf{k}} \rangle|^2 \tag{2.46}$$

in which f is the occupation factor and the Y_{ml} are the spherical harmonics. Atomic projection allows for the assignment of electronic charge density and spin density to specific atoms. This is helpful in, for instance, differentiating the two possible intermediate oxidation states for a PBA: $AM^{J-1}[M'^{K}(\mathrm{CN})_6]$ versus $AM^{J}[M'^{K-1}(\mathrm{CN})_6]$. The projection of the density of states is discussed frequently in this work. It is useful for determining which atoms give rise to valence- and conduction-band states.

This section explains the scientific and mathematical procedures by which important materials properties like voltage, ion-hopping activation energy, and the density of states are calculated from the ground-state electronic density and total energy (and the single-particle Kohn–Sham wavefunctions). These methods are used throughout this work to understand the theoretical properties and performances of new PBA compositions.

2.5 Conclusions

This chapter describes the methodology used in the rest of this work. DFT is a suite of theoretical, ab-initio methods to describe the properties of materials. The Kohn–Sham equations are a set of equations that can be solved iteratively to find the ground-state electronic density. The Hohenberg and Kohn theorem guarantees that the functional which maps from that ground-state to the total energy exists. The method to expand the equations to describe electron spin, and thus magnetism in materials, is sketched. The failure of conventional DFT functionals within the LDA and GGA to describe strongly correlated systems is described; the advantages and disadvantages of hybrid functionals and DFT+U to overcome the electron self-interaction error are discussed. Finally, the mathematical procedures to move from DFT's output, ground-state electronic density and total energy (and the approximate single-particle Kohn–Sham wavefunctions), are described as used throughout this work. This chapter's review of DFT is a concise summary of several levels of electronic-density-based theory. It will be beneficial to researchers beginning first-principles studies of PBAs and of battery materials.

References

[1] F. Giustino, *Materials modelling using Density Functional Theory: Properties and Predictions*. Oxford, England: Oxford University Press, 2014.

[2] D. S. Sholl and J. A. Steckel, *Density Functional Theory: A Practical Introduction*. Hoboken, New Jersey: Wiley, 2009.

[3] D. A. McQuarrie, *Quantum Chemistry*. Sausalito, California: University Science Books, 2 ed., 2008.

[4] E. Schrödinger, "Quantisierung als Eigenwertproblem," *Annalen der Physik*, vol. 384, p. 5572, 1926.

[5] W. J. Duffin, *Electricity and Magnetism*. McGraw-Hill, 4 ed., 1990.

[6] R. M. Martin, *Electronic Structure: Basic Theory and Practical Methods*. Cambridge University Press, 2004.

[7] W. Kohn and P. Hohenberg, "Inhomogeneous Electron Gas," *Physical Review B*, vol. 136, no. 3, pp. 864–871, 1964.

[8] W. Kohn and L. J. Sham, "Self-Consistent Equations Including Exchange and Correlation Effects," *Physical Review A*, vol. 140, no. 4, pp. 1132–1138, 1965.

[9] W. Gerlach and O. Stern, "Der experimentelle Nachweis der Richtungsquantelung im Magnetfeld," *Zeitschrift für Physik*, vol. 9, pp. 349–352, 1922.

[10] P. Dirac, "The quantum theory of the electron," *Proceedings of the Royal Sociey of London*, vol. 117, p. 610, 1928.

[11] U. von Barth and L. Hedin, "A local exchange-correlation potential for the spin polarized case," *Journal of Physics C: Solid State Pysics*, vol. 5, p. 1629, 1972.

[12] B. H. Bransden and C. J. Joachain, *Physics of Atoms and Molecules*. 2 ed.

[13] A. Messiah, *Quantum Mechanics Volume II*. Elsevier Science B.V., 1961.

[14] F. Bloch, "Über die Quantenmechanik der Elektronen in Kristallgittern," *Zeitschrift für Physik*, vol. 52, pp. 555–600, 1928.

[15] N. W. Ashcroft and N. D. Mermin, *Solid State Physics*. Holt-Saunders, 1976.

[16] C. Kittel, *Introduction to Solid State Physics*. Wiley, 8 ed., 2004.

[17] S. G. Johnson and M. Frigo, "A modified split-radix FFT with reduced arithmetic complexity," *IEEE Transactions on Signal Processing*, vol. 55, no. 1, pp. 111–119, 2005.

[18] A. Castro, H. Appel, M. Oliveira, C. A. Rozzi, X. Andrade, F. Lorenzen, M. A. Marques, E. K. Gross, and A. Rubio, "Octopus: A tool for the application of time-dependent density functional theory," *Physica Status Solidi (B) Basic Research*, vol. 243, no. 11, pp. 2465–2488, 2006.

[19] J. A. Pople, M. Head-Gordon, D. J. Fox, K. Raghavachari, and L. A. Curtiss, "Gaussian-1 theory: A general procedure for prediction of molecular energies," *The Journal of Chemical Physics*, vol. 90, no. 10, pp. 5622–5629, 1989.

[20] D. Vanderbilt, "Soft self-consistent pseudopotentials in a generalized eigenvalue formalism," *Physical Review B*, vol. 41, no. 11, pp. 7892–7895, 1990.

[21] G. Kresse and D. Joubert, "From ultrasoft pseudopotentials to the projector augmented-wave method," *Physical Review B - Condensed Matter and Materials Physics*, vol. 59, no. 3, pp. 1758–1775, 1999.

[22] R. Peverati and D. G. Truhlar, "Quest for a universal density functional: The accuracy of density functionals across a broad spectrum of databases in chemistry and physics," *Philosophical Transactions of the Royal Society A: Mathematical, Physical and Engineering Sciences*, vol. 372, no. 2011, p. 20120476, 2014.

[23] A. L. Fetter and J. D. Walecka, *Quantum Theory of Many-Particle Systems*. Dover Publications, 2003.

[24] D. M. Ceperley and B. J. Alder, "Ground state of the electron gas by a stochastic method," *Physical Review Letters*, vol. 45, no. 7, pp. 566–569, 1980.

[25] J. P. Perdew and A. Zunger, "Self-interaction correction to density-functional approximations for many-electron systems," *Physical Review B*, vol. 23, no. 10, pp. 5048–5079, 1981.

[26] J. P. Perdew, K. Burke, and M. Ernzerhof, "Generalized Gradient Approximation Made Simple," *Physical Review Letters*, vol. 77, no. 18, pp. 3865–3868, 1996.

[27] B. G. Johnson, C. A. Gonzales, P. M. W. Gill, and J. A. Pople, "A density functional study of the simplest hydrogen abstraction reaction. Effect of self-interaction correction," *Chemical Physics Letters*, vol. 221, no. 1-2, pp. 100–108, 1994.

[28] F. Liu and H. J. Kulik, "Impact of Approximate DFT Density Delocalization Error on Potential Energy Surfaces in Transition Metal Chemistry," *Journal of Chemical Theory and Computation*, vol. 16, no. 1, pp. 264–277, 2020.

[29] J. Paier, M. Marsman, K. Hummer, G. Kresse, I. C. Gerber, and J. G. Angyán, "Screened hybrid density functionals applied to solids," *Journal of Chemical Physics*, vol. 124, no. 15, p. 154709, 2006.

[30] J. L. Da Silva, M. V. Ganduglia-Pirovano, J. Sauer, V. Bayer, and G. Kresse, "Hybrid functionals applied to rare-earth oxides: The example of ceria," *Physical Review B - Condensed Matter and Materials Physics*, vol. 75, no. 4, pp. 19–24, 2007.

[31] J. Heyd, G. E. Scuseria, and M. Ernzerhof, "Hybrid functionals based on a screened Coulomb potential," *Journal of Chemical Physics*, vol. 118, no. 18, pp. 8207–8215, 2003.

[32] A. V. Krukau, O. A. Vydrov, A. F. Izmaylov, and G. E. Scuseria, "Influence of the exchange screening parameter on the performance of screened hybrid functionals," *The Journal of chemical physics*, vol. 125, no. 22, p. 224106, 2006.

[33] V. I. Anisimov, F. Aryasetiawan, and A. I. Lichtenstein, "First-principles calculations of the electronic structure and spectra of strongly correlated systems: The LDA + U method," *Journal of Physics: Condensed Matter*, vol. 9, no. 4, pp. 767–808, 1997.

[34] B. Himmetoglu, A. Floris, S. De Gironcoli, and M. Cococcioni, "Hubbard-corrected DFT energy functionals: The LDA+U description of correlated systems," *International Journal of Quantum Chemistry*, vol. 114, no. 1, pp. 14–49, 2014.

[35] J. Hubbard, "Electron correlations in narrow energy bands," *Proceedings of the Royal Society of London. Series A. Mathematical and Physical Sciences*, vol. 276, no. 1365, pp. 238–257, 1963.

[36] J. Hubbard, "Electron correlations in narrow energy bands. II. The degenerate band case," *Proceedings of the Royal Society of London. Series A. Mathematical and Physical Sciences*, vol. 277, no. 1369, pp. 237–259, 1964.

[37] J. Hubbard, "Electron correlations in narrow energy bands III. An improved solution," *Proceedings of the Royal Society of London. Series A. Mathematical and Physical Sciences*, vol. 281, no. 1386, pp. 401–419, 1964.

[38] V. I. Anisimov, J. Zaanen, and O. K. Andersen, "Band theory and Mott insulators: Hubbard U instead of Stoner I," *Physical Review B*, vol. 44, no. 3, pp. 943–954, 1991.

[39] H. J. Kulik, M. Cococcioni, D. A. Scherlis, and N. Marzari, "Density functional theory in transition-metal chemistry: A self-consistent Hubbard U approach," *Physical Review Letters*, vol. 97, no. 10, pp. 1–4, 2006.

[40] V. L. Chevrier, S. P. Ong, R. Armiento, M. K. Chan, and G. Ceder, "Hybrid density functional calculations of redox potentials and formation energies of transition metal compounds," *Physical Review B - Condensed Matter and Materials Physics*, vol. 82, no. 7, pp. 1–11, 2010.

[41] L. Wang, T. Maxisch, and G. Ceder, "Oxidation energies of transition metal oxides within the GGA+U framework," *Physical Review B - Condensed Matter and Materials Physics*, vol. 73, no. 19, pp. 1–6, 2006.

[42] H. Hellmann, "Zur Rolle der kinetischen Elektronenenergie für die zwischenatomaren Kräfte," *Zeitschrift für Physik*, vol. 85, no. 3-4, pp. 180–190, 1933.

[43] R. P. Feynman, "Forces in molecules," *Physical Review*, vol. 56, no. 4, pp. 340–343, 1939.

[44] P. Pulay, "Convergence acceleration of iterative sequences. The case of SCF iteration," *Chemical Physics Letters*, vol. 73, no. 2, pp. 393–398, 1980.

[45] W. H. Press, W. T. Vetterling, S. A. Teukolsky, and B. P. Flannery, *Numerical Recipes in C++: The Art of Scientific Computing*. Cambridge, England: Cambridge University Press, 2002.

[46] A. Van der Ven, M. K. Aydinol, G. Ceder, G. Kresse, and J. Hafner, "First-principles investigation of phase stability in Li_xCoO_2," *Physical Review B*, vol. 58, no. 6, pp. 2975–2987, 1998.

[47] M. Mayo, K. J. Griffith, C. J. Pickard, and A. J. Morris, "Ab Initio Study of Phosphorus Anodes for Lithium- and Sodium-Ion Batteries," *Chemistry of Materials*, vol. 28, no. 7, pp. 2011–2021, 2016.

[48] M. K. Aydinol, A. F. Kohan, G. Ceder, K. Cho, and J. Joannopoulos, "Ab initio study of lithium intercalation in metal oxides and metal dichalcogenides," *Physical Review B*, vol. 56, no. 3, pp. 1354–1365, 1997.

[49] L. R. Faulkner and A. J. Bard, *Electrochemical methods: fundamentals and applications*. John Wiley & Sons, 2 ed., 2002.

[50] J. Newman and K. E. Thomas-Alyea, *Electrochemical systems*. John Wiley & Sons, 3 ed., 2012.

[51] G. Henkelman, B. P. Uberuaga, and H. Jónsson, "Climbing image nudged elastic band method for finding saddle points and minimum energy paths," *Journal of Chemical Physics*, vol. 113, no. 22, pp. 9901–9904, 2000.

[52] M. S. Islam, D. J. Driscoll, C. A. Fisher, and P. R. Slater, "Atomic-scale investigation of defects, dopants, and lithium transport in the $LiFePO_4$ olivine-type battery material," *Chemistry of Materials*, vol. 17, no. 20, pp. 5085–5092, 2005.

[53] M. Schüler, O. E. Peil, G. J. Kraberger, R. Pordzik, M. Marsman, G. Kresse, T. O. Wehling, and M. Aichhorn, "Charge self-consistent many-body corrections using optimized projected localized orbitals," *Journal of Physics: Condensed Matter*, vol. 30, no. 47, 2018.

Chapter 3

Electronic structure and electron-transport properties of three metal hexacyanoferrates

Abstract

Metal hexacyanometallates, or Prussian blue analogs (PBAs), are active materials in important electrochemical technologies, including next-generation sodium- and potassium-ion batteries. They have tunable properties including reduction potential, ionic conductivity, and color. However, little is known about their electronic conductivities. In this work, I use density-functional theory to model electronic structures and explore the likely electron-conduction mechanism in three promising cathodes (manganese, iron, and cobalt hexacyanoferrate) in each of three oxidation states. First, I demonstrate that a hybrid functional reliably reproduces experimentally observed spin configurations and geometric phase changes. I confirm that these materials are semiconductors or insulators with band gaps ranging from 1.90 eV up to 4.94 eV. I identify that for most of the compounds the electronic band edges originate from carbon-coordinated-iron orbitals, suggesting that doping at the carbon-coordinated site may strongly affect carrier conductivity. Finally, I calculate charge-carrier effective masses, which are very high. This study is an important foundation for making electronic conductivity a tunable PBA material property.

3.1 Electronic conductivity in the PBAs

Manganese, iron, and cobalt hexacyanoferrate are the Prussian blue analog (PBA) compositions that are among the most promising cathodes for sodium-ion batteries [1–3]. They have high reduction potentials (about +1.0 V versus the standard hydrogen electrode), a high specific capacity of about 170 $\mathrm{mA\,h\,g^{-1}}$, and two flat voltage plateaus. Despite the importance of this system, a critical material property remains poorly understood; that property is the electronic conductivity.

Many structure-property relationships have been established in the PBAs. In particular, the effect of the choice of elements for the two lattice ions and the inserting metal ion on properties like lattice parameter [4], reduction potential [5], and coefficient of thermal expansion [6] have been reported previously. But there has never been a systematic study of the effect of composition on electronic conductivity. This is despite the fact that electronic conductivity is important in virtually every PBA-based technology. Early work on the composition $\mathrm{NaFe[Fe(CN)_6]}$ (also known as Prussian blue, the prototype compound) reported a value on the order of $\sigma_\mathrm{e} = 10^{-5}\,\mathrm{S\,m^{-1}}$, but it lacked structural characterization [7]. Studies on the effect of hydration state [8] and nickel substitution at the nitrogen-coordinated site [9] gave similar values. The full range of possible values for the electronic conductivities of the PBAs remains unmeasured.

Here the electronic structure and electron-transport properties are explored systematically for ($\mathrm{Na}_x\mathrm{Mn[Fe(CN)_6]}$), ($\mathrm{Na}_x\mathrm{Fe[Fe(CN)_6]}$), and ($\mathrm{Na}_x\mathrm{Co[Fe(CN)_6]}$). Each material is studied in each of three oxidation states ($x \in \{0, 1, 2\}$) for a total of nine (9) compounds, related schematically in Figure 3.1. The ground-state spin configuration for each compound is determined by comparing the total energy of the low-spin and high-spin phases. The projected densities of states are calculated to examine the nature of the valence- and conduction-bands as well as to determine the compounds' band gaps. Finally, the charge-carrier effective masses are calculated.

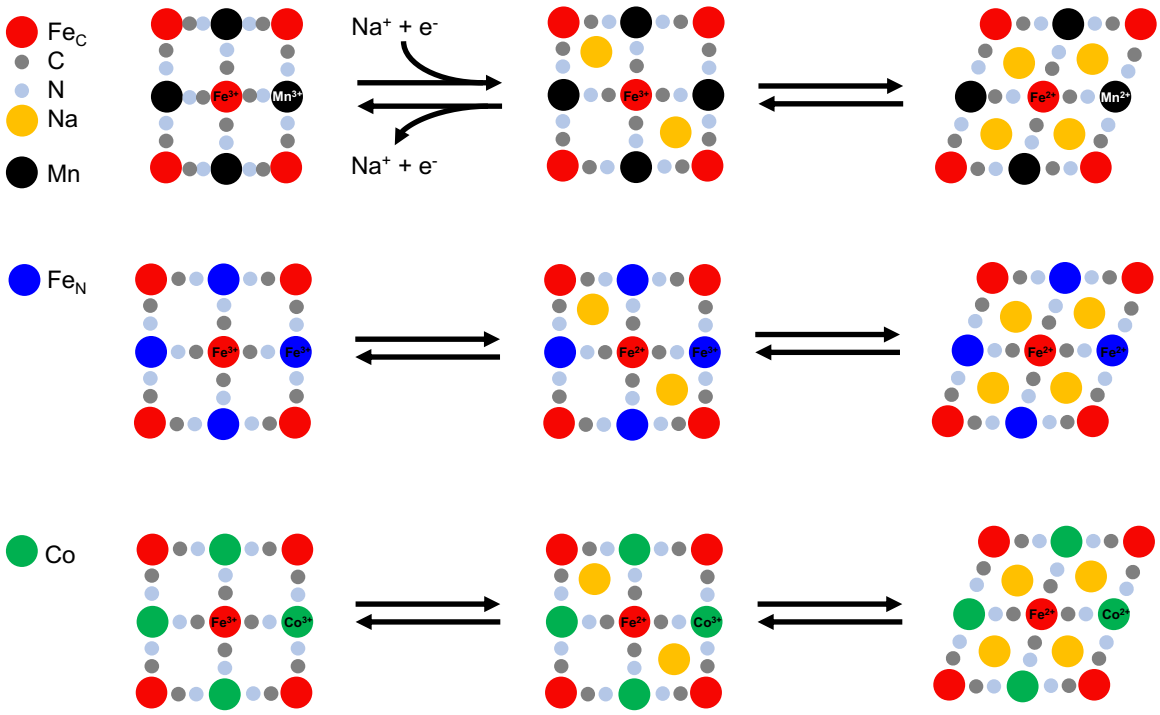

Figure 3.1: Metal hexacyanoferrate phases. Manganese (black, top), iron (blue, middle), and cobalt (green, bottom) hexacyanoferrates are shown in each of three oxidation states corresponding to 0 (left), 1 (middle), and 2 (right) sodium ions (gold) per formula unit. Note reaction arrows showing the addition of sodium (reduction) or removal of sodium (oxidation) in the upper left are implied in all the other 5 reactions; they are omitted only for clarity.

Results are compared between the Perdew–Burke–Ernzerhof (PBE) functional [10] and the hybrid Heyd–Scuseria–Ernzerhof (HSE06) functional [11, 12]. This work is a critically important study of the electronic structure of three highly promising cathodes for sodium-ion batteries, and it is an important foundation for making electronic conductivity a tunable PBA property.

3.2 Ground-state crystal structure and spin configurations

For PBAs, the carbon-coordinated metal ion assumes a low-spin (ls) electronic configuration while the nitrogen-coordinated metal is usually in a high-spin (hs) electronic configuration. In order to treat the spin configuration of PBAs within spin-polarized

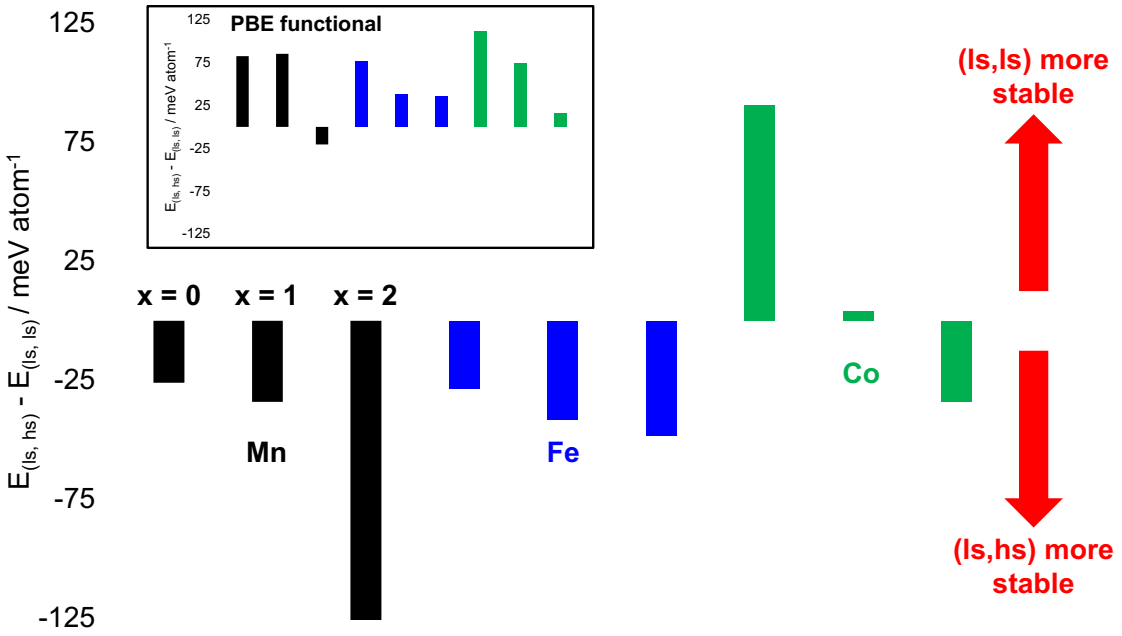

Figure 3.2: Energy differences between spin configurations. Negative differences correspond to energetic stability of the (ls, hs) state. Black, blue, and green bars correspond to Mn, Fe, and Co, respectively. Within each color, the three bars represent 0, 1, or 2 Na ions per formula unit from left to right. The inset shows the results using the PBE functional. Reprinted with permission from [13]. Copyright 2021 American Chemical Society.

DFT calculations, I assume a ferromagnetic ordering between the two metal centers and fix the overall spin, per formula unit, of the material, and perform a total energy calculation. Figure 3.2 shows the difference in total energy between the (ls, hs) configuration and the (ls, ls) configuration. Seven compounds are more stable in the (ls, hs) configuration, and only compounds $Co[Fe(CN)_6]$ and $NaCo[Fe(CN)_6]$ are more stable in the (ls, ls) configuration. The total energies calculated using the hybrid functional correctly reproduce the experimentally observed spin configuration for all nine compounds as measured by soft X-ray absorption and infrared spectroscopies [1, 2, 4]. Contrast these results with those calculated by the PBE functional, which incorrectly energetically favors the (ls, ls) configuration for eight of the nine compounds.

The compound $NaMn[Fe(CN)_6]$ can attain two (ls, hs) electronic configurations: (Fe(t_{2g}^5), Mn($t_{2g}^3 e_g^2$)) and (Fe(t_{2g}^6), Mn($t_{2g}^3 e_g^1$)), with the latter lower in energy by less

than $0.04\,\mathrm{meV\,atom^{-1}}$. These correspond to different oxidation states: (Fe(III), Mn(II)) versus (Fe(II), Mn(III)), respectively. Experimental characterization including X-ray diffractometry, X-ray photoelectron spectroscopy, and infrared spectroscopy have shown that below 225 K, the tetragonal, Jahn–Teller-distorted (Fe(t_{2g}^6), Mn($t_{2g}^3 e_g^1$)) phase is favored, in agreement with these calculations; at higher temperatures, cubic (Fe(t_{2g}^5), Mn($t_{2g}^3 e_g^2$)) is observed [14]. Furthermore, operando X-ray diffraction (XRD) [15] and ex-situ X-ray absorption near-edge structure (XANES) [16] studies of room-temperature batteries clearly show that the manganese is first reduced from manganese(III) to manganese(II) and then the iron is reduced form iron(III) to iron(II) [2]. So in the rest of this chapter I only consider the technologically relevant (Fe(t_{2g}^5), Mn($t_{2g}^3 e_g^2$)) phase of NaMn[Fe(CN)$_6$]. The three iron compounds are lower in energy in the (ls, hs) configuration. The intermediate oxidation state is (Fe$_\mathrm{C}$(t_{2g}^6), Fe$_\mathrm{N}$($t_{2g}^3 e_g^2$)), which is also consistent with experimental findings.[1]. The compounds' electronic configurations as calculated within HSE are shown in Figure 3.3.

Each atom in Figure 3.3 has two sets of valence orbitals: the triply degenerate t_{2g} orbitals (lower in energy) and the doubly degenerate e_g orbitals (higher in energy). These originate from the 5 degenerate, atomic d orbitals in the isolated atom. The $d_{x^2-y^2}$ and d_{z^2} orbitals are oriented such that the maxima of their electron densities are on axis (the x and y axes for the $d_{x^2-y^2}$ orbital and the z axis for the d_{z^2} orbital). In contrast the d_{xy}, d_{yz}, and d_{xz} orbitals are oriented with their maximal electron density off axis. Within crystal field theory, the ligands are modeled as negatively charged point particles. For octahedral crystal environments (as in the PBAs), the ligands' negative charge interacts repulsively more with the on-axis orbitals ($d_{x^2-y^2}$ and d_{z^2}) which increase in energy and become the e_g orbitals. And the ligands' charge density interacts less with the off-axis orbitals (d_{xy}, d_{yz}, and d_{xz}) which become the t_{2g} orbitals. The names e_g and t_{2g} come from the orbitals' symmetries. The separation in energy between the t_{2g} and e_g orbitals is designated Δ_oct. If Δ_oct is large, the ligand

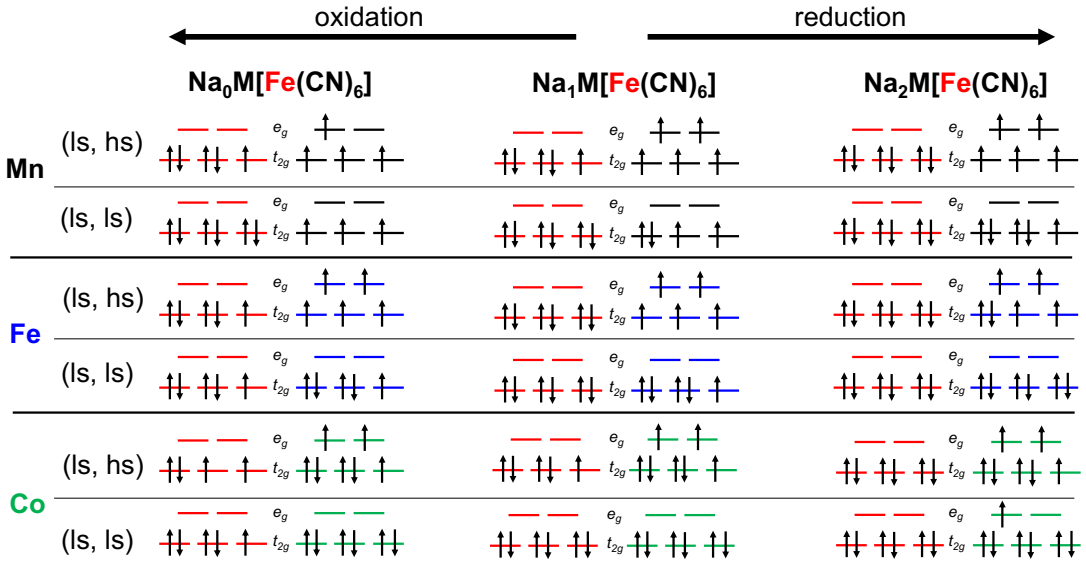

Figure 3.3: Ground-state electronic configurations. The three t_{2g} orbitals and two e_g orbitals are formed from the five d orbitals of an octahedrally coordinated transition metal. The red orbitals correspond to carbon-coordinated iron, while black, blue, and green states refer to manganese, nitrogen-coordinated iron, and cobalt orbitals, respectively. Reprinted with permission from [13]. Copyright 2021 American Chemical Society.

is referred to as a "strong-field ligand". (Cyanide is an example of a strong-field ligand when coordinated via the carbon atom.) Strong-field ligands lead to low-spin configurations on the metal atom as it is energetically favorable to fill the relatively low-lying t_{2g} orbitals. In contrast, "weak-field" ligands (like bromide) have a small Δ_{oct}, on the order of the energy of repulsion between two electrons (of opposite spin) in the same orbital. Weak-field ligands cause a high-spin configuration on the metal atom.

The two lower oxidation states of the cobalt compound (i.e. $Co[Fe(CN)_6]$ and $NaCo[Fe(CN)_6]$) are more stable in the (ls, ls) configuration; both contain cobalt(III, ls). On further reduction to $Na_2Co[Fe(CN)_6]$, the cobalt becomes cobalt(II) and switches to high spin. This is in agreement with electrochemical observations of a spin transition over the second reduction plateau during battery discharge [17]. $NaCo[Fe(CN)_6]$ has the smallest energy difference between the two spin configura-

tions at 4 meV atom^{-1}. This small energetic difference is consistent with studies that observe facile photo-induced spin transition in this material [18]. These experiments show that the spin transition is accompanied by a charge transfer from the iron to the cobalt. The calculated atom-projected magnetic moment vanishes on both the iron atom and the cobalt atom in the ground state, which is consistent with a non-spin-polarized electronic configuration of t_{2g}^6 for iron and t_{2g}^6 for cobalt. In the higher energy (ls, hs) state, the atom-projected magnetic moments are $\mu_{\mathrm{Fe}} = 1.051\,\mu_{\mathrm{B}}$ and $\mu_{\mathrm{Co}} = 2.753\,\mu_{\mathrm{B}}$ (where μ_{B} is the Bohr magneton). This is consistent with an electronic configuration of t_{2g}^5 for iron and $t_{2g}^5 e_g^2$ for cobalt, shown in Figure 3.3, and supports the experimental model of charge-transfer-accompanied spin transition [18]. All other energy differences are greater (in magnitude) than the thermal excitation of 26 meV atom^{-1} at 300 K.

In terms of crystal structure, the fully oxidized compound $\mathrm{Mn[Fe(CN)_6]}$ has a tetragonal geometry. This is the result of a Jahn–Teller distortion arising from the electronic configuration on the manganese, $\mathrm{Mn}(t_{2g}^3 e_g^1)$. The simulated X-ray diffractogram for this compound, shown in Figure 3.4 along with the diffractograms for all other compounds, has two peaks at 16.68° and 17.62°. These arise from the (110) and (101) reflections, respectively. On reduction to $\mathrm{NaMn[Fe(CN)_6]}$, the sodium ion occupies the center of the face separating two subcubes (that is, the cubic interstice formed by eight cyanide ligands and four of each lattice metal ion). This relaxes the tetragonal distortion, so that the (110) and (101) reflections combine into a single intense peak at about 16.79°. But it introduces a slight rhombohedral distortion. The lattice vectors are changed by about 2° away from the value of 60° for the face-centered cubic geometry. The fully reduced compound $\mathrm{Na_2Mn[Fe(CN)_6]}$ has its second sodium ion in a different face of the cube and is also rhombohedrally distorted. For the iron materials, the fully oxidized compound $\mathrm{Fe[Fe(CN)_6]}$ is cubic. The reduced compounds $\mathrm{NaFe[Fe(CN)_6]}$ and $\mathrm{Na_2Fe[Fe(CN)_6]}$ have their sodium ions in the cube faces and are

Table 3.1: Average bond lengths in $NaFe[Fe(CN)_6]$. The cyanide bond length and the average Fe_C–C bond lengths are mostly unchanged, but the Fe_N–N bond length increases by 7.3% in the (ls, hs) phase versus the (ls, ls) phase.

	(ls, ls)	(ls, hs)
volume / Å^3	246.08	267.12
Fe_N–N / Å	1.92	2.06
N–C / Å	1.16	1.17
C–Fe_C / Å	1.89	1.89

rhombohedrally distorted. For the cobalt materials, $Co[Fe(CN)_6]$ is cubic and the reduced compounds are rhombohedrally distorted. For all compounds, the main difference between the (ls, ls) and the (ls, hs) configurations is a longer M_N–N bond length (where M_N is Mn, Fe, or Co), and thus higher unit-cell volumes, for the (ls, hs) configuration. This is due to the increased density of spin-aligned electrons. As an example, the bond lengths for the two spin configurations of $NaFe[Fe(CN)_6]$ are summarized in Table 3.2. Finally, comparing structural optimization between DFT-PBE with the hybrid HSE functional, I found that both result in basically the same geometry for all studied compounds.

These calculated geometries are consistent with two important phase changes that have been observed experimentally. First, fully desodiated $Mn[Fe(CN)_6]$ has been shown to be tetragonal [2]. Second, $Na_xMn[Fe(CN)_6]$, $Na_xFe[Fe(CN)_6]$, and $Na_xCo[Fe(CN)_6]$ all become rhombohedral above a critical sodium concentration between 1 and 2 sodium ions per formula unit, $1 < x_{\text{critical}} < 2$ [19, 20]. Below x_{critical} the compounds are cubic (except for $Mn[Fe(CN)_6]$, which, as discussed, is tetragonal). The calculated geometries are already rhombohedral in the $x = 1$ phase. I attribute the early onset of the rhombohedral distortion to the fact that the simulated compounds are completely free of vacancies and crystalline water, both of which are known to stabilize the cubic structure over the rhombohedral structure [21].

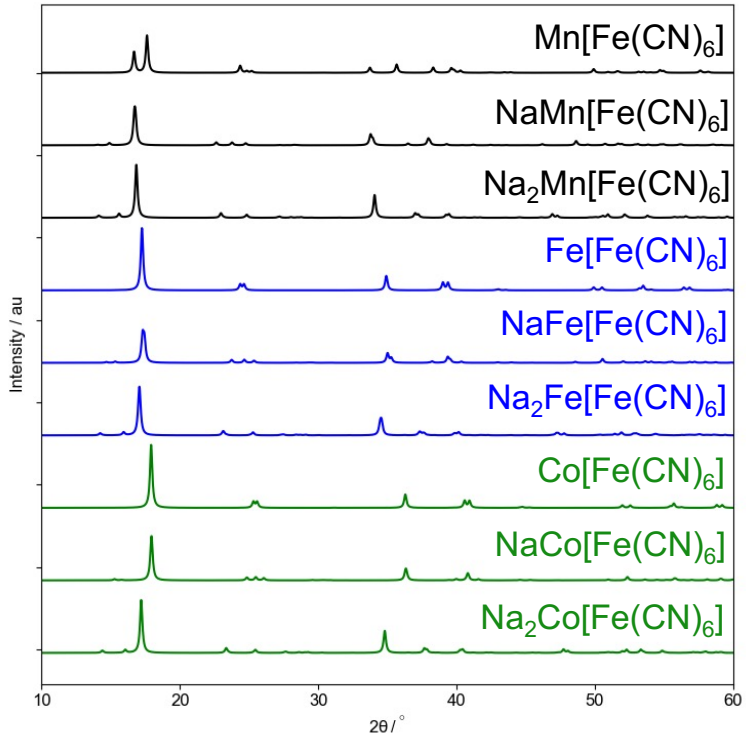

Figure 3.4: Simulated diffractograms for the hexacyanoferrates. The X-ray diffractograms for the compounds $Na_xM[Fe(CN)_6]$ are simulated using VESTA at an incident wavelength of $\lambda = 1.5406$ Å and plotted using a Lorenzian function with $\gamma = 0.1°$.

3.3 Atomic projections of valence- and conduction-band states

The projected density of states (PDOS) for the ground-state spin configuration of the nine materials as calculated with the HSE functional are shown in Figure 3.5. (The PDOS as calculated with the PBE functional are plotted for comparison in Figure 3.6. The differences between the two levels of theory are highlighted and discussed at the end of this section.) For $Mn^{III}[Fe^{III}(CN)_6]$, the valence-band states arise from spin-down iron t_{2g} orbitals, which are nearly degenerate with the spin-up manganese e_g orbitals and cyanide orbitals. The conduction-band states stem from spin-down, iron t_{2g} orbitals. The valence-band states for $NaMn^{II}[Fe^{III}(CN)_6]$ originate from the spin-up, manganese e_g orbitals, in accordance with Figure 3.3 and the conduction-band states still arise from spin-down, iron t_{2g} orbitals. These become occupied on further reduction to $Na_2Mn^{II}[Fe^{II}(CN)_6]$, in which the valence-band states stem from degenerate spin-up iron t_{2g} orbitals, spin-up manganese e_g orbitals, spin-down iron t_{2g} orbitals, and cyanide orbitals. The conduction-band states originate from spin-down manganese t_{2g} orbitals and cyanide orbitals.

In $Fe^{III}[Fe^{III}(CN)_6]$, the valence-band states arise from spin-down t_{2g} orbitals on the carbon-coordinated iron. The conduction band bottom stems from t_{2g} orbitals of both iron atoms, which is consistent with the t_{2g}^5 and t_{2g}^3 spin configuration shown in Figure 3.3. Upon reduction, $NaFe^{III}[Fe^{II}(CN)_6]$ also has its valence-band states originating from the carbon-coordinated-iron, but the conduction-band states now solely originate from the nitrogen-coordinated-iron t_{2g} orbitals. This can be explained due to the change of the carbon-coordinated-iron spin configuration to the fully filled t_{2g}^6. Further reduction to $Na_2Fe^{II}[Fe^{II}(CN)_6]$ breaks the symmetry of the spin-down nitrogen-coordinated-iron t_{2g} orbitals, one of which becomes occupied. Both the valence-band and the conduction-band states thus stem from spin-down orbitals.

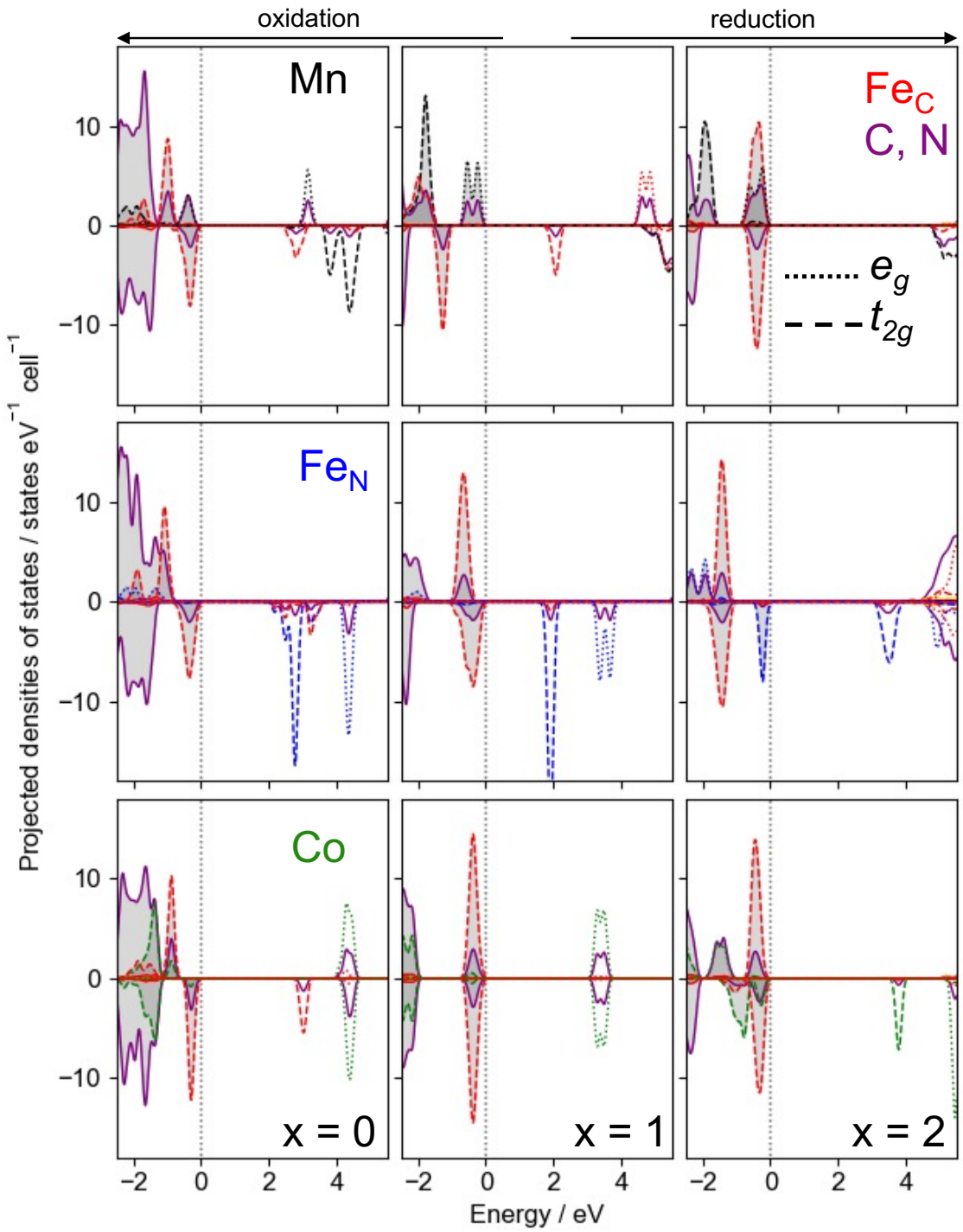

Figure 3.5: PDOS computed with the HSE06 functional. The top, middle, and bottom rows correspond to Mn, Fe, and Co, respectively. The left, middle, and right columns correspond to 0, 1, and 2 Na ions per formula unit, respectively. The energy axis is referred to the Fermi level (gray, dotted line) and occupied states are shaded light gray. Reprinted with permission from [13]. Copyright 2021 American Chemical Society.

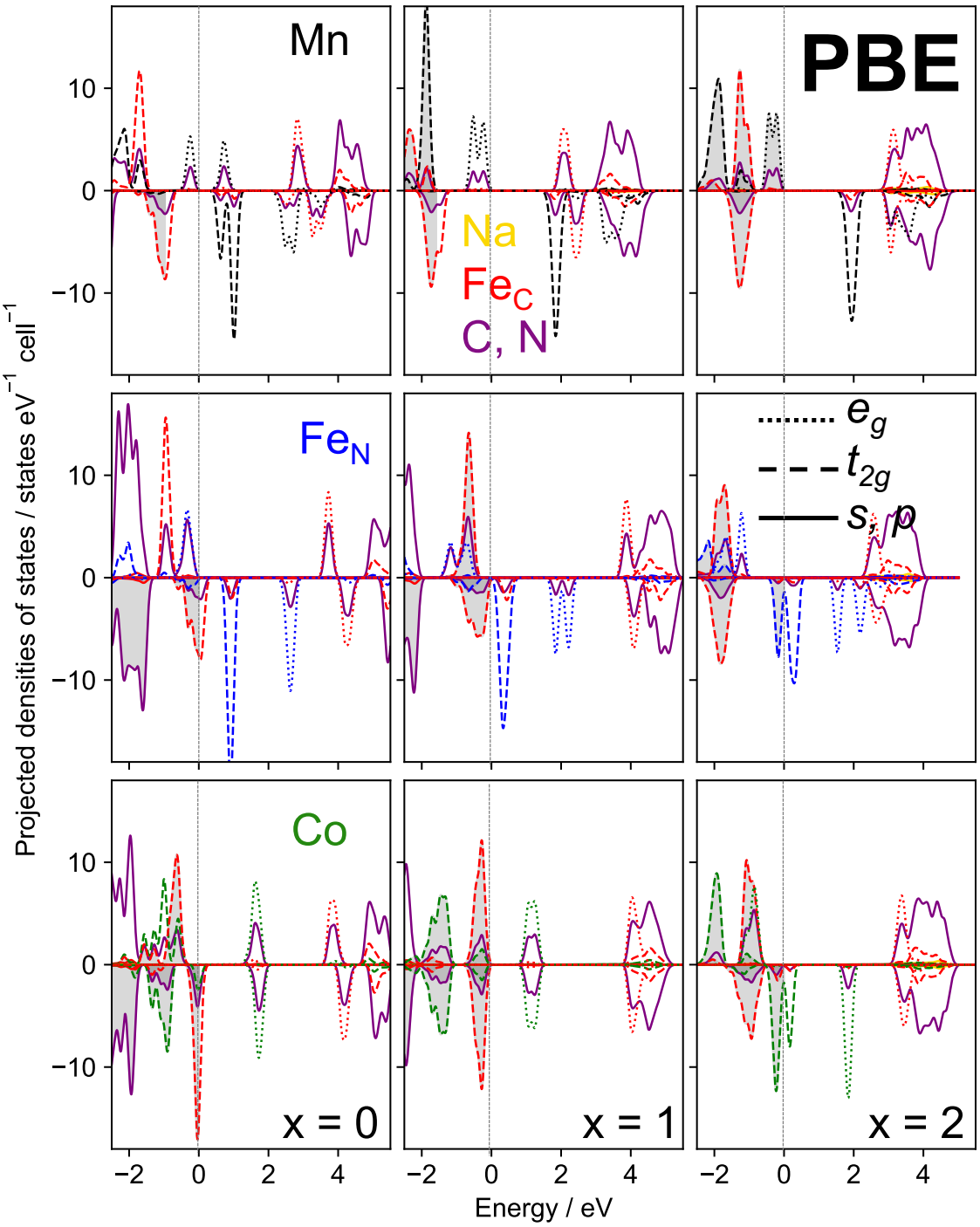

Figure 3.6: PDOS computed with the PBE functional. The top, middle, and bottom rows correspond to Mn, Fe, and Co, respectively. The left, middle, and right columns correspond to 0, 1, and 2 Na ions per formula unit, respectively. Occupied states are shaded light gray. Reprinted with permission from [13]. Copyright 2021 American Chemical Society.

Similarly in $Co^{III}[Fe^{III}(CN)_6]$, both the conduction- and valence-band states arise from spin-down, iron t_{2g} orbitals. For the reduced material, $NaCo^{III}[Fe^{II}(CN)_6]$, both Co- and Fe-sites are in the same fully filled t_{2g}^6 electronic configuration; hence, it is not spin-polarized. Valence-band states originate from the iron t_{2g} orbitals and the conduction-band states arise from cobalt e_g orbitals (and some cyanide states). The spin transition of the cobalt on reduction to $Na_2Co^{II}[Fe^{II}(CN)_6]$ changes the electronic structure substantially. The valence-band states stem from degenerate spin-up and spin-down iron t_{2g} orbitals. The valence band originate from spin-down cobalt t_{2g} orbitals.

In eight of the nine compounds either the valence-band or conduction-band states (or both) arise from t_{2g} orbitals of the carbon-coordinated iron atom. For all three fully oxidized materials ($x = 0$), both the valence and conduction bands stem from the carbon-coordinated iron. This suggests that the carbon-coordinated iron participates significantly in the conduction of charge-carrying electrons and holes through the metal hexacyanoferrate lattice, especially for battery electrodes in the fully charged state. Sluggish kinetics caused by low electronic or ionic conductivity have been suggested as the cause of low Coulombic efficiency, especially in manganese hexacyanoferrate [22]. Research efforts to increase conductivity have focused on doping the nitrogen-coordinated element [16]. However, if the low Coulombic efficiency is caused by lower conductivity in the fully oxidized lattice, then these results suggest that experimental work must refocus on doping the carbon-coordinated iron to improve cycle lives of PBA batteries.

All nine materials have band gaps with values, as calculated with the HSE functional, shown in Table 3.2. The gaps range from 1.90 eV to 4.94 eV. Even the smallest band gap is too large for appreciable populations of thermally generated carriers at room temperature. The calculated band gap for Prussian blue, $NaFe^{III}[Fe^{II}(CN)_6]$, is 1.90 eV, versus an experimental value of 1.75 eV [23]. The material $NaCo[Fe(CN)_6]$

Table 3.2: Band gaps calculated using the HSE functional. Reprinted with permission from [13]. Copyright 2021 American Chemical Society.

	M[Fe(CN)$_6$]	NaM[Fe(CN)$_6$]	Na$_2M$[Fe(CN)$_6$]
Mn	2.46	2.88	4.94
Fe	1.96	1.90	3.33
Co	3.00	3.33*	3.80

* direct band gap

has a direct band gap; the rest have indirect band gaps.

The PDOS as calculated with the PBE functional, shown in Figure 3.6, differ substantially from the HSE-level PDOS. Note that the PBE-level PDOS do *not* correspond to the PBE-predicted ground spin configuration; rather, they correspond to the spin configuration as predicted using the HSE functional (that is, (ls, hs) except for Co[Fe(CN)$_6$] and NaCo[Fe(CN)$_6$]) so as to make a fair comparison. The first and most important difference is that the PBE functional predicts that six of nine compounds, Mn[Fe(CN)$_6$], NaMn[Fe(CN)$_6$], Fe[Fe(CN)$_6$], Na$_2$Fe[Fe(CN)$_6$], Co[Fe(CN)$_6$], and Na$_2$Co[Fe(CN)$_6$], are half-metals. As half-metals, those compounds have partially occupied states at the Fermi level in exactly one spin channel. Partial occupation at the Fermi level is a hallmark of metals, and so the PBE functional predicts metallic electronic conduction in one spin channel. For those six compounds the spin-down (minority-spin) channel is metallic. For the other three compounds, one, NaFe[Fe(CN)$_6$], is a zero-gap semiconductor and the gaps for the remaining two compounds are much smaller than the gaps as predicted by the HSE functional.

3.4 Charge-carrier effective masses and charge distributions

This section proceeds to an actual calculation of the effective masses of the charge carriers in this system. The location of the valence-band tops (VBTs) and conduction-band bottoms (CBBs) in reciprocal space are tabulated. A slice of the 3-dimensional

dispersion relation (that is, the relationship between band energy, ϵ_ν and crystal momentum, $\hbar\mathbf{k}$) is then plotted; these energy isosurfaces at ± 10 meV the VBT and CBB, respectively, give a sense of how dispersive the bands are and the directionality of the dispersion. Finally, the band-decomposed charge densities are projected onto atomic orbitals and rendered.

The effective mass of an electron is defined as the second derivative of the electron energy with respect to the wavevector $\mathbf{k}$ about the minimum according to

$$m_{ij}^* = \hbar^2(\partial^2\epsilon/\partial k_i \partial k_j)^{-1},$$

in which i and j are the indices for the three crystallographic directions, ϵ is the energy eigenvalue, $\hbar$ is the reduced Planck's constant, and m_{ij}^* is the (i, j) component of the effective-mass tensor [24]. The partial derivatives are calculated numerically using a first-order, finite-difference approximation, and diagonalization of the effective-mass tensors gives the effective masses along the three principal axes.

Figures 3.7 through 3.9 are slices of the compounds' energy-wavevector dispersion relations. Each surface is the set of all $\mathbf{k}$ points in the first Brillouin zone with energy corresponding to 10 meV below the valence-band top (left plot) or 10 meV above the conduction-band bottom (right plot). They have several general features important to evaluating and comparing effective masses. First, the center of each isosurface is the $\mathbf{k}$ point at which the derivatives are evaluated. These are summarized in Tables 3.4 and 3.4. For example, the Γ point is the center for the conduction-band bottoms in $Mn[Fe(CN)_6]$, $NaMn[Fe(CN)_6]$, $Na_2Mn[Fe(CN)_6]$, $Fe[Fe(CN)_6]$, and $Co[Fe(CN)_6]$ and for the valence-band tops in $Na_2Fe[Fe(CN)_6]$ and $Na_2Co[Fe(CN)_6]$. Larger isosurfaces are less dispersive, so they correspond to heavier effective masses. Compare the conduction bands in $Mn[Fe(CN)_6]$ and $NaMn[Fe(CN)_6]$; the latter has a larger isosurface and a heavier electron effective mass. Finally, the shape of the isosurface indicates the directionality of the effective masses. A spherical energy

Table 3.3: Wavevectors of the valence-band tops. Reprinted with permission from [13]. Copyright 2021 American Chemical Society.

	k_x / $2\pi/a$	k_y / $2\pi/a$	k_z / $2\pi/a$
$Mn[Fe(CN)_6]$	-0.98	0.00	0.00
$NaMn[Fe(CN)_6]$	-0.46	0.46	-0.50
$Na_2Mn[Fe(CN)_6]$	-0.04	-0.04	0.98
$Fe[Fe(CN)_6]$	-1.02	0.00	0.00
$NaFe[Fe(CN)_6]$	0.00	0.00	1.02
$Na_2Fe[Fe(CN)_6]$	0.00	0.00	0.00
$Co[Fe(CN)_6]$	-1.06	0.00	0.00
$NaCo[Fe(CN)_6]$	0.00	0.00	1.06
$Na_2Co[Fe(CN)_6]$	0.00	0.00	0.00

surface corresponds to an isotropic effective mass while an ellipsoidal surface indicates a degree of anisotropy.

The results shown in Figures 3.7 through 3.9 are useful first in confirming that the valence-band tops and conduction-band bottoms are well separated from other points in the first Brillouin zone. This is significant because degenerate band extrema can both contribute to electron or hole transport. So, if there are degenerate extrema the effective masses at both points should be calculated. However, the extrema for these nine compounds are all well separated as shown by Figures 3.7 through 3.9. These results are significant as a qualitative demonstration that the valence and conduction bands are not very dispersive in these PBA materials. This high degree of delocalization of electronic states in reciprocal space implies a high degree of localization of electronic states (and thus electron density) in real space. This is especially insightful as complementary evidence to the data shown in Figure 3.10 and discussed in the context of PBAs as ionic crystals below.

The isotropic average effective mass ($m^* = (\frac{1}{3}\Sigma_i m_i^{*-1})^{-1}$) for the compounds are given in Table 3.5. The hole effective masses range from $2.06\,m_e$ in $NaCo[Fe(CN)_6]$ to $3.62\,m_e$ in $Na_2Mn[Fe(CN)_6]$ with a median value of $2.60\,m_e$ for all nine compounds. (The unit m_e is the electron rest mass.) The electron effective masses range from

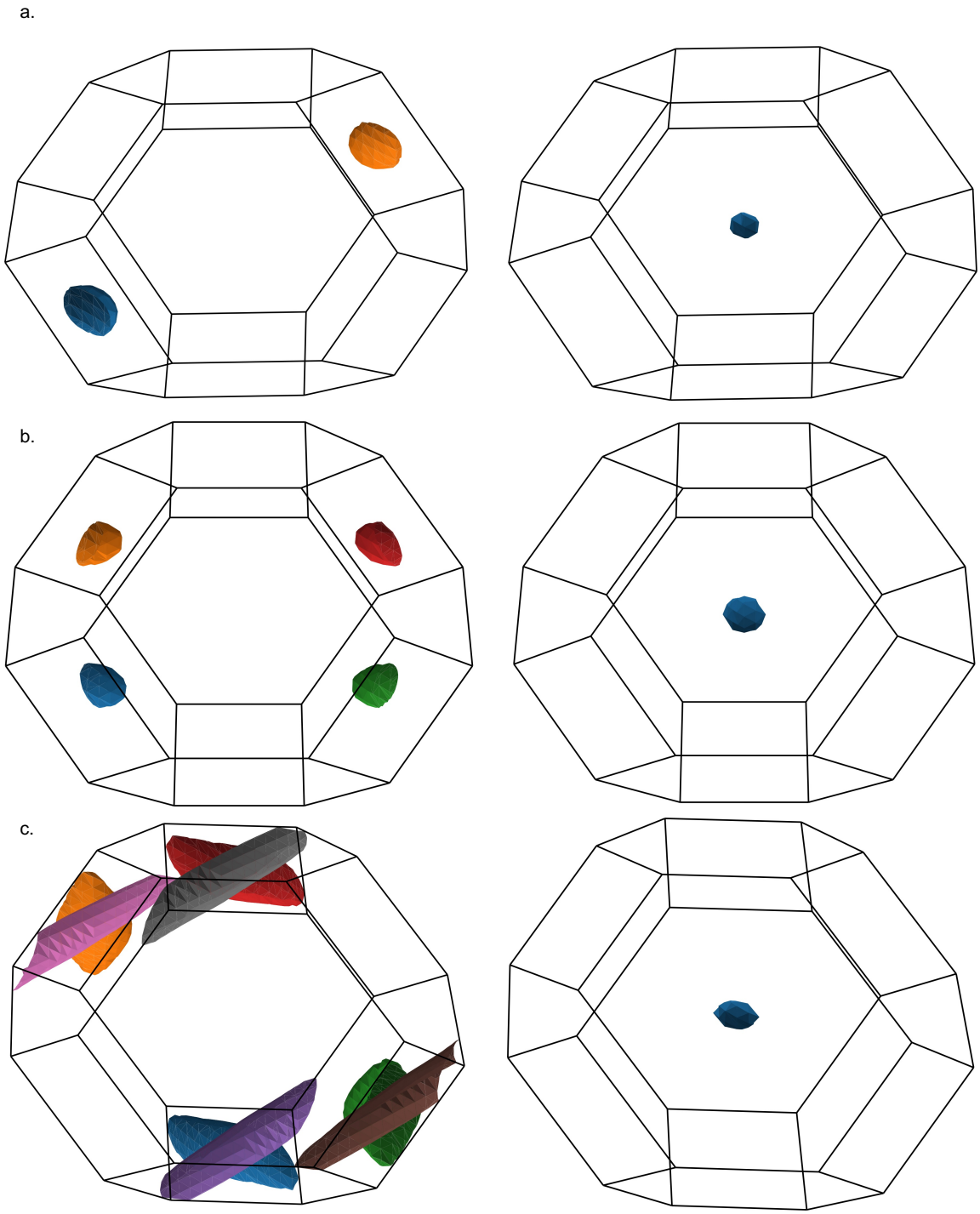

Figure 3.7: Energy isosurfaces for $Na_xMn[Fe(CN)_6]$. The energy isosurfaces in the first Brillouin zone at 10 meV below the valence-band top (left) and 10 meV above the conduction-band bottom (right) for (a) $Na_0Mn[Fe(CN)_6]$, (b) $Na_1Mn[Fe(CN)_6]$, and (c) $Na_2Mn[Fe(CN)_6]$. Reprinted with permission from [13]. Copyright 2021 American Chemical Society.

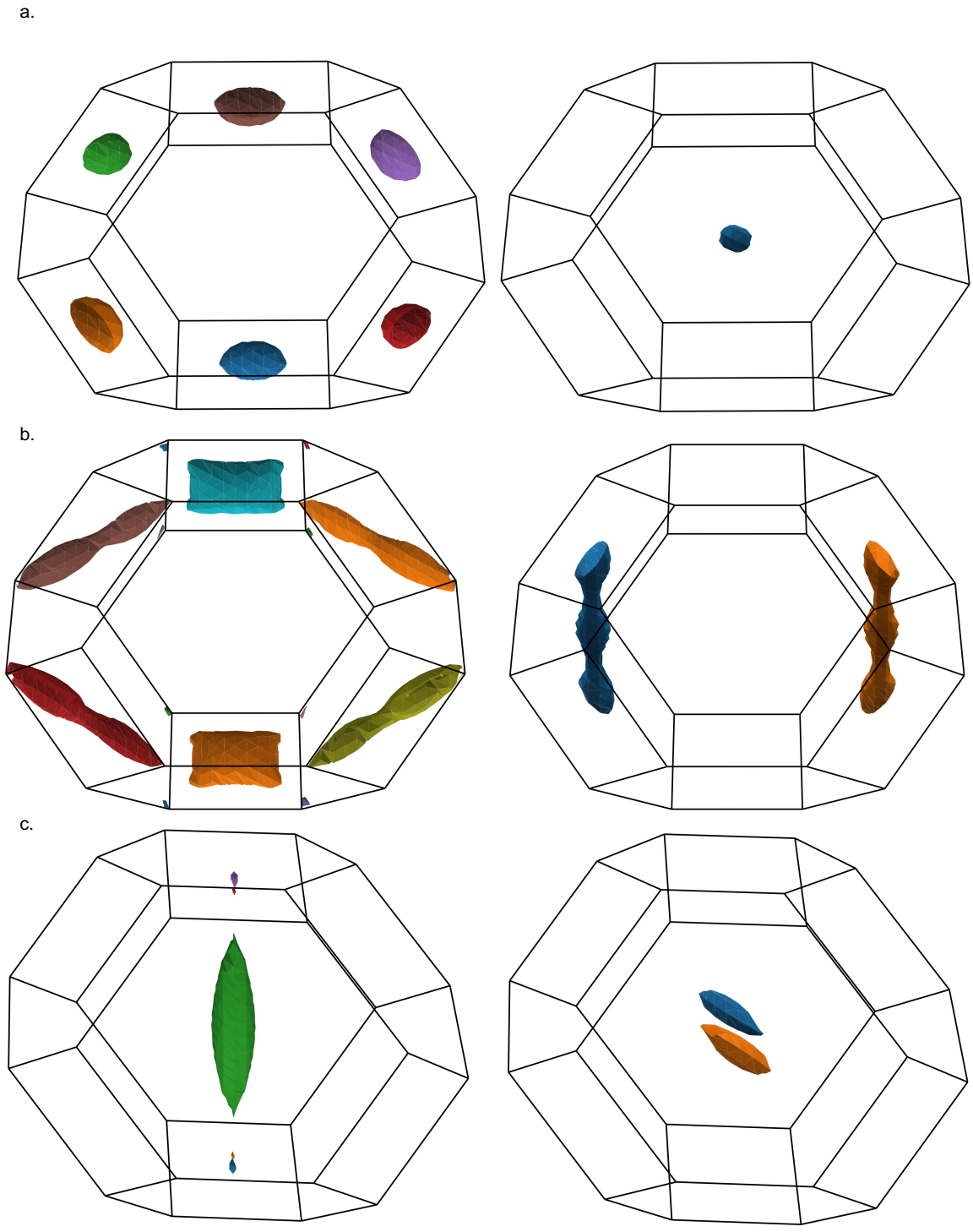

Figure 3.8: Energy isosurfaces for $Na_xFe[Fe(CN)_6]$. The energy isosurfaces in the first Brillouin zone at 10 meV below the valence-band top (left) and 10 meV above the conduction-band bottom (right) for (a) $Na_0Fe[Fe(CN)_6]$, (b) $Na_1Fe[Fe(CN)_6]$, and (c) $Na_2Fe[Fe(CN)_6]$. Reprinted with permission from [13]. Copyright 2021 American Chemical Society.

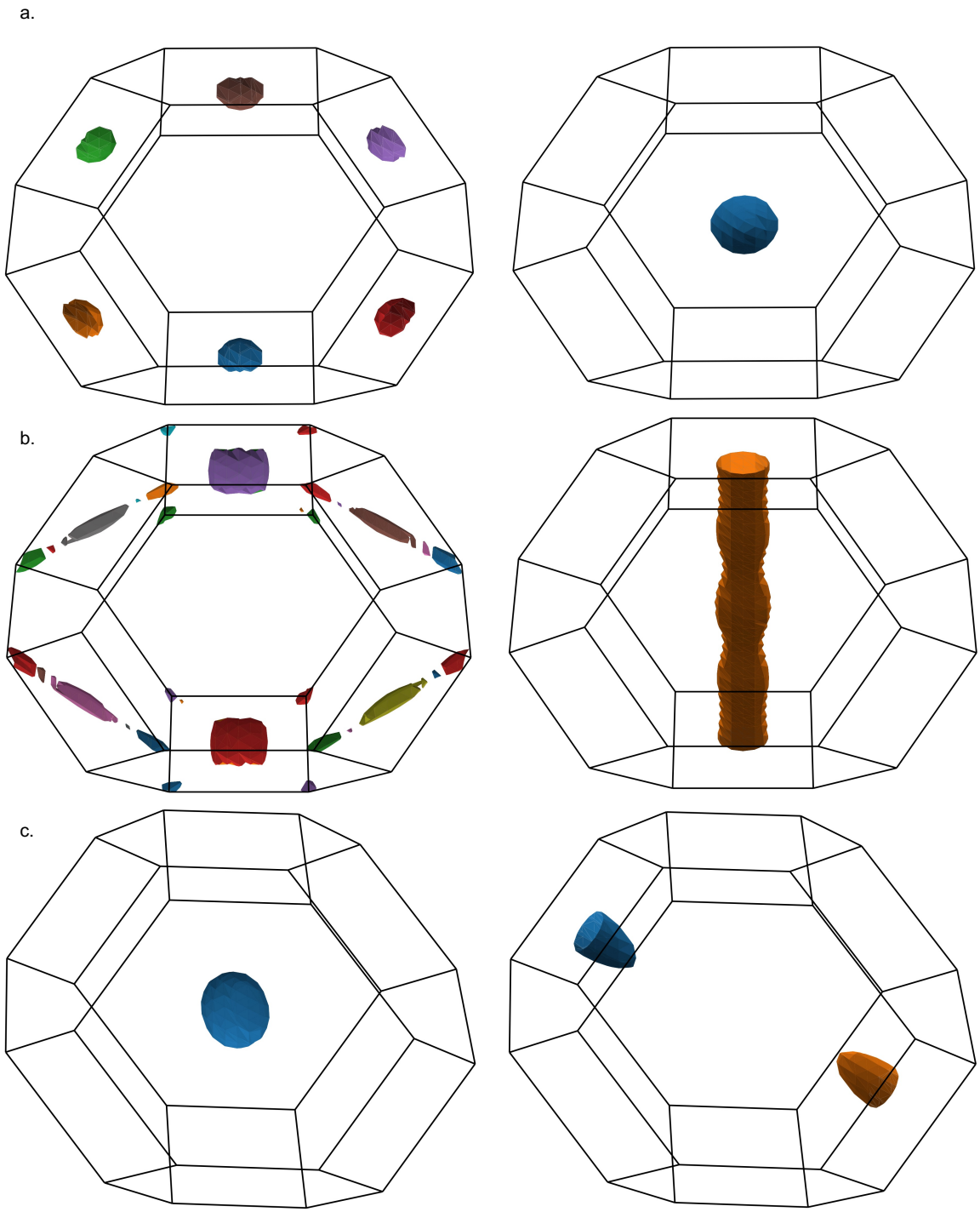

Figure 3.9: Energy isosurfaces for $Na_xCo[Fe(CN)_6]$. The energy isosurfaces in the first Brillouin zone at 10 meV below the valence-band top (left) and 10 meV above the conduction-band bottom (right) for (a) $Na_0Co[Fe(CN)_6]$, (b) $Na_1Co[Fe(CN)_6]$, and (c) $Na_2Co[Fe(CN)_6]$. Reprinted with permission from [13]. Copyright 2021 American Chemical Society.

Table 3.4: Wavevectors of the conduction-band bottoms. Reprinted with permission from [13]. Copyright 2021 American Chemical Society.

	k_x / $2\pi/a$	k_y / $2\pi/a$	k_z / $2\pi/a$
$Mn[Fe(CN)_6]$	0.00	0.00	0.00
$NaMn[Fe(CN)_6]$	0.00	0.00	0.00
$Na_2Mn[Fe(CN)_6]$	0.00	0.00	0.00
$Fe[Fe(CN)_6]$	0.00	0.00	0.00
$NaFe[Fe(CN)_6]$	-0.50	0.50	0.00
$Na_2Fe[Fe(CN)_6]$	0.50	0.50	0.46
$Co[Fe(CN)_6]$	0.00	0.00	0.00
$NaCo[Fe(CN)_6]$	0.00	0.00	1.06
$Na_2Co[Fe(CN)_6]$	-0.46	0.50	-0.50

Table 3.5: Charge-carrier effective masses, in units of the electron rest mass. Reprinted with permission from [13]. Copyright 2021 American Chemical Society.

	Na_0		Na_1		Na_2	
	m^*_{hole}	m^*_{electron}	m^*_{hole}	m^*_{electron}	m^*_{hole}	m^*_{electron}
$Mn[Fe(CN)_6]$	2.82	0.87	2.28	1.41	3.62	1.39
$Fe[Fe(CN)_6]$	2.60	0.73	2.44	2.15	3.00	1.94
$Co[Fe(CN)_6]$	2.20	4.95	2.06	2.88	2.92	3.04

$0.73\,m_e$ in $Fe[Fe(CN)_6]$ to $4.95\,m_e$ in $Co[Fe(CN)_6]$ with a median value of $1.94\,m_e$ for all nine compounds.

The effective masses are very high due to the fact that these compounds are ionic crystals, as shown in the band-decomposed charge densities for the valence and conduction bands of Figure 3.10. Eight of the nine compounds have significant valence-band charge density on the carbon-coordinated iron atom, and six of nine compounds have significant conduction-band charge density on the carbon-coordinated iron atom. This is in agreement with the PDOS data, and underscores the need for investigation of the effect of doping at this site for tuning PBA electronic conductivity. Also of note is that the valence band in Prussian blue, $NaFe[Fe(CN)_6]$, is localized on the carbon-coordinated iron while the conduction band is localized on the nitrogen-coordinated iron. This is consistent with experimental observation of charge transfer

between the two iron atoms on excitation of a valence electron to the conduction band [23]. In general, the charge density is highly localized on the transition-metal ions. Together, the high effective masses and the ionic character of the electronic structure imply that small-polaron hopping is likely an important mechanism for charge conduction in these compounds. First-principles studies have shown the importance of small-polaron hopping for electronic conductivity in battery materials including lithium iron phosphate [25] and the (manganese, cobalt) oxide family [26]. Tennakone and coworkers used small-polaron hopping to interpret experimental data on the complicated relationship between crystalline water, temperature, and electronic conductivity in Prussian blue ($NaFe[Fe(CN)_6]$) [8]. These theoretical results rationalize Tennakone and coworkers' application of the small-polaron-hopping mechanism to understand their data; these results also call for future work to model and understand polarons in PBAs in greater detail.

3.5 Conclusions

In this chapter, I modeled three highly promising sodium-ion cathodes in each of three oxidation states with a hybrid functional to better understand their electronic conductivity and electron-transport properties.

First, the crystal structures of all nine compounds are relaxed and compared using the PBE and HSE functionals in two difference spin configurations: (low spin, low spin) and (low spin, high spin). The total energies as calculated using the two functionals are compared, and it is found that the HSE functional reproduces the experimentally observed ground state for all nine compounds. The ground state is (low spin, high spin) for all compounds except $Co[Fe(CN)_6]$ and $NaCo[Fe(CN)_6]$ for which it is (low spin, low spin). In contrast, the PBE functional fails badly, predicting that the (low spin, low spin) is lower in energy for all but one compound. Crystallographically, the cubic-to-rhombohedral and cubic-to-tetragonal phase changes are

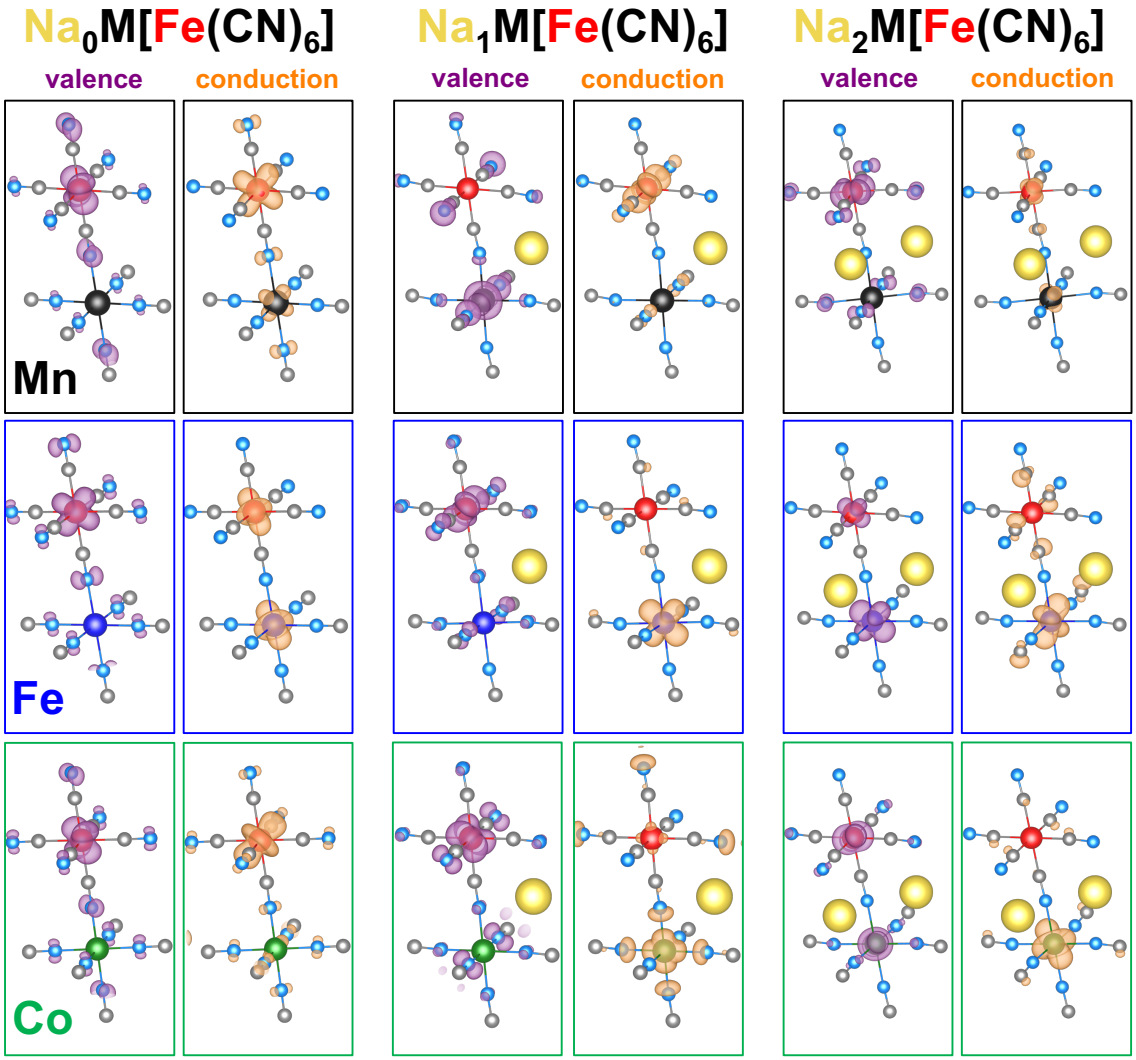

Figure 3.10: Band-decomposed charge densities. For each compound, the band-decomposed charge-density isosurface is plotted for the valence band (purple, left) and the conduction-band (orange, right). The manganese, iron, and cobalt compounds are in the top, middle, and bottom rows, respectively. The number of sodium ions (gold) per formula unit are 0 (fully oxidized), 1, and 2 (fully reduced) from left to right. Reprinted with permission from [13]. Copyright 2021 American Chemical Society.

reproduced by the model.

The PDOS make it clear that all these compounds exhibit an electronic band gap with wide separation in energy between the valence band and the conduction band, ranging from 1.90 eV to 4.94 eV. This is the first calculation of the gap for most of these compounds. The PDOS and band-decomposed charge densities further reveal the importance of the carbon-coordinated iron, which gives rise to conduction- and valence-bands states in many cases, confirming this as a promising site for substitutional doping to design more or less electronically conductive PBAs.

The charge-carrier effective masses are calculated, with median values of 2.60 m_e for holes and 1.94 m_e for electrons. These very high effective masses, along with the highly ionic character of the compounds, suggest that small-polaron hopping is likely an important mechanism for electron transport. Future work will center around modeling polarons in PBAs in greater detail.

This is the first work to explore electron transport in PBAs computationally, and it contributes to the understanding of PBA electronic conductivity, a critically important material property for batteries, electrocatalysts, and more. These calculations predict a charge-transfer-mediated spin transition for several compounds, which in several instances agrees with extant experimental observation. I confirm that all studied compounds exhibit an electronic band gap. I identify the importance of the carbon-coordinated iron to electronic conductivity, despite experimental focus of doping only at the nitrogen-coordinated site. Finally, I report charge-carrier effective masses in a PBA for the first time. These results are important contributions to the study of PBA electronic conductivity and first-principles modeling, and this work lays the theoretical groundwork to incorporate electronic conductivity into the repertoire of tunable PBA properties.

Computational details

All calculations were carried out using DFT as implemented in the Vienna ab initio Simulation Package (VASP) [27, 28]. A Γ-centered $4 \times 4 \times 4$ **k**-point grid and a planewave kinetic-energy cutoff of 520 eV were used. Electronic and ionic convergence criteria were 10^{-5} eV and 0.05 eV Å^{-1}, respectively. Atomic positions and lattice parameters were relaxed for all compounds with both the PBE and HSE functionals separately. The initial geometry for all relaxations was $Fm\overline{3}m$ with lattice parameter 10.4 Å, with small perturbations introduced to the atomic positions and lattice parameters to allow the model to access lower symmetries. (The lattice parameters of the compounds studied have been measured experimentally and are within about 3% of 10.4 Å [29]. The initial lattice parameter was uniform across all 9 compounds, so more significant digits were not used.) For the HSE functional, I used the HSE06 functional [11, 12], with the standard screening parameter of 0.2 Å^{-1} and a mixing of 25% Fock exchange with 75% PBE exchange. The X-ray diffraction reflections were calculated using an incident photon wavelength of $\lambda = 1.5406$ Å in the "**V**isualization for **E**lectronic and **St**ructural **A**nalysis" (VESTA) software [30, 31] and the diffractograms were plotted using the Lorentzian function with $\gamma = 0.01°$. The effective masses were calculated using a first-order finite-difference approximation of the second partial derivative of the energies at 18 zero-weight **k** points about the band extremum with a discretization of the local reciprocal space of $0.01 \cdot 2\pi/a$. Band-decomposed charge densities were calculated using the band and **k** point that were used for the effective-mass calculations.

References

[1] L. Wang, J. Song, R. Qiao, L. A. Wray, M. A. Hossain, Y. D. Chuang, W. Yang, Y. Lu, D. Evans, J. J. Lee, S. Vail, X. Zhao, M. Nishijima, S. Kakimoto, and

J. B. Goodenough, "Rhombohedral Prussian white as cathode for rechargeable sodium-ion batteries," *Journal of the American Chemical Society*, vol. 137, no. 7, pp. 2548–2554, 2015.

[2] J. Song, L. Wang, Y. Lu, J. Liu, B. Guo, P. Xiao, J. J. Lee, X. Q. Yang, G. Henkelman, and J. B. Goodenough, "Removal of interstitial H_2O in hexacyanometallates for a superior cathode of a sodium-ion battery," *Journal of the American Chemical Society*, vol. 137, no. 7, pp. 2658–2664, 2015.

[3] X. Wu, C. Wu, C. Wei, L. Hu, J. Qian, Y. Cao, X. Ai, J. Wang, and H. Yang, "Highly Crystallized $Na_2CoFe(CN)_6$ with Suppressed Lattice Defects as Superior Cathode Material for Sodium-Ion Batteries," *ACS Applied Materials and Interfaces*, vol. 8, no. 8, pp. 5393–5399, 2016.

[4] M. Pasta, R. Y. Wang, R. Ruffo, R. Qiao, H.-W. Lee, B. Shyam, M. Guo, Y. Wang, L. A. Wray, W. Yang, M. F. Toney, and Y. Cui, "Manganese–cobalt hexacyanoferrate cathodes for sodium-ion batteries," *Journal of Materials Chemistry A*, vol. 4, no. 11, pp. 4211–4223, 2016.

[5] F. Scholz and A. Dostal, "The formal potentials of solid metal hexacyanometalates," *Angewandte Chemie International Edition in English*, vol. 34, no. 23-24, pp. 2685–2687, 1996.

[6] C. Wang, D. Chang, Q. Gao, C. Liu, Q. Wang, X. Huang, and Y. Jia, "Large and tunable negative thermal expansion induced by a synergistic effect in $M^{II}_2[M^{IV}(CN)_6]$ Prussian blue analogues," *Physical Chemistry Chemical Physics*, pp. 18655–18662, 2020.

[7] A. Xidis and V. D. Neff, "On the Electronic Conduction in Dry Thin Films of Prussian Blue, Prussian Yellow, and Everitt's Salt," *Journal of the Electrochemistry Society*, vol. 138, no. 12, pp. 3637–3642, 1991.

[8] K. Tennakone and W. G. D. Dharmaratne, "Experimental and theoretical study of electronic conduction in H_2O-doped Prussian blue," *Journal of Physics C Solid State*, vol. 16, no. 29, pp. 5633–5639, 1983.

[9] A. Shrivastava and K. C. Smith, "Electron Conduction in Nanoparticle Agglomerates Limits Apparent Na^+ Diffusion in Prussian Blue Analogue Porous Electrodes," *Journal of the Electrochemistry Society*, vol. 165, no. 9, pp. A1777–A1787, 2018.

[10] J. P. Perdew, K. Burke, and M. Ernzerhof, "Generalized Gradient Approximation Made Simple," *Physical Review Letters*, vol. 77, no. 18, pp. 3865–3868, 1996.

[11] J. Heyd, G. E. Scuseria, and M. Ernzerhof, "Hybrid functionals based on a screened Coulomb potential," *Journal of Chemical Physics*, vol. 118, no. 18, pp. 8207–8215, 2003.

[12] A. V. Krukau, O. A. Vydrov, A. F. Izmaylov, and G. E. Scuseria, "Influence of the exchange screening parameter on the performance of screened hybrid functionals," *The Journal of chemical physics*, vol. 125, no. 22, p. 224106, 2006.

[13] K. Hurlbutt, F. Giustino, M. Pasta, and G. Volonakis, "Electronic structure and electron-transport properties of three metal hexacyanoferrates," *Chemistry of Materials*, vol. 33, no. 17, pp. 7067–7074, 2021.

[14] H. Tokoro, S. I. Ohkoshi, T. Matsuda, and K. Hashimoto, "A large thermal hysteresis loop produced by a charge-transfer phase transition in a rubidium manganese hexacyanoferrate," *Inorganic Chemistry*, vol. 43, no. 17, pp. 5231–5236, 2004.

[15] X. Bie, K. Kubota, T. Hosaka, K. Chihara, and S. Komaba, "A novel K-ion battery: hexacyanoferrate(II)/graphite cell," *Journal of Materials Chemistry A*, vol. 5, no. 9, pp. 4325–4330, 2017.

[16] L. Jiang, Y. Lu, C. Zhao, L. Liu, J. Zhang, Q. Zhang, X. Shen, J. Zhao, X. Yu, H. Li, X. Huang, L. Chen, and Y.-S. Hu, "Building aqueous K-ion batteries for energy storage," *Nature Energy*, vol. 4, no. 6, pp. 495–503, 2019.

[17] Y. Kurihara, H. Funashima, M. Ishida, N. Hamada, T. Matsuda, K. Igarashi, H. Tanida, T. Uruga, and Y. Moritomo, "Electronic structure of hole-doped transition metal cyanides," *Journal of the Physical Society of Japan*, vol. 79, no. 4, pp. 1–7, 2010.

[18] M. Cammarata, S. Zerdane, L. Balducci, G. Azzolina, S. Mazerat, C. Exertier, M. Trabuco, M. Levantino, R. Alonso-Mori, J. M. Glownia, S. Song, L. Catala, T. Mallah, S. F. Matar, and E. Collet, "Charge transfer driven by ultrafast spin transition in a CoFe Prussian blue analogue," *Nature Chemistry*, vol. 13, no. 1, pp. 10–14, 2021.

[19] Y. You, X.-L. Wu, Y.-X. Yin, and Y. G. Guo, "High-quality Prussian blue crystals as superior cathode materials for room-temperature sodium-ion batteries," *Energy and Environmental Science*, vol. 7, no. 5, pp. 1643–1647, 2014.

[20] J. C. Pramudita, S. Schmid, T. Godfrey, T. Whittle, M. Alam, T. Hanley, H. E. Brand, and N. Sharma, "Sodium uptake in cell construction and subsequent in operando electrode behaviour of Prussian blue analogues, $Fe[Fe(CN)_6]_{1-x} \cdot yH_2O$ and $FeCo(CN)_6$," *Physical Chemistry Chemical Physics*, vol. 16, no. 44, pp. 24178–24187, 2014.

[21] Y. Moritomo, Y. Kurihara, T. Matsuda, and J. Kim, "Structural phase diagram of Mn-Fe cyanide against cation concentration," *Journal of the Physical Society of Japan*, vol. 80, no. 10, pp. 8–11, 2011.

[22] M. Fiore, S. Wheeler, K. Hurlbutt, I. Capone, J. Fawdon, R. Ruffo, and M. Pasta, "Paving the Way Toward Highly Efficient High-Energy Potassium-Ion Batteries

with Ionic-Liquid Electrolytes," *Chemistry of Materials*, vol. 32, pp. 7653–7661, 2020.

[23] M. B. Robin, "The Color and Electronic Configurations of Prussian Blue," *Inorganic Chemistry*, vol. 1, no. 2, pp. 337–342, 1962.

[24] M. R. Filip, C. Verdi, and F. Giustino, "GW Band Structures and Carrier Effective Masses of $CH_3NH_3PbI_3$ and Hypothetical Perovskites of the Type $APbI_3 : A = NH_4, PH_4, AsH_4,$ and SbH_4," *Journal of Physical Chemistry C*, vol. 119, no. 45, pp. 25209–25219, 2015.

[25] C. A. Fisher, V. M. Prieto, and M. S. Islam, "Lithium battery materials $LiMPO_4$ (M = Mn, Fe, Co, and Ni): Insights into defect association, transport mechanisms, and doping behavior," *Chemistry of Materials.*, vol. 20, no. 18, pp. 5907–5915, 2008.

[26] Z. Q. Wang, Y. C. Chen, and C. Y. Ouyang, "Polaron states and migration in F-doped Li_2MnO_3," *Physical Letters A*, vol. 378, no. 32-33, pp. 2449–2452, 2014.

[27] G. Kresse, J. Furthmüller, and J. Hafner, "Theory of the crystal structures of selenium and tellurium: The effect of generalized-gradient corrections to the local-density approximation," *Physical Review B*, vol. 50, no. 18, pp. 13181–13185, 1994.

[28] G. Kresse and J. Furthmüller, "Efficiency of ab-initio total energy calculations for metals and semiconductors using a plane-wave basis set," *Computational Materials Science*, vol. 6, no. 1, pp. 15–50, 1996.

[29] Y. Lu, L. Wang, J. Cheng, and J. B. Goodenough, "Prussian blue: a new framework of electrode materials for sodium batteries," *Chemical Communications*, vol. 48, no. 52, p. 6544, 2012.

[30] K. Momma and F. Izumi, "VESTA: A three-dimensional visualization system for electronic and structural analysis," *Journal of Applied Crystallography*, vol. 41, no. 3, pp. 653–658, 2008.

[31] K. Momma and F. Izumi, "VESTA 3 for three-dimensional visualization of crystal, volumetric and morphology data," *Journal of Applied Crystallography*, vol. 44, no. 6, pp. 1272–1276, 2011.

Chapter 4

Origin of the high specific capacity in sodium manganese hexacyanomanganate

Abstract

Sodium manganese hexacyanomanganate, $Na_xMn[Mn(CN)_6]$, has been studied experimentally as an active material in rechargeable batteries. It has a reversible specific capacity of 209 mA h g^{-1}—substantially higher than the theoretical specific capacity of 172 mA h g^{-1} expected for insertion of two sodium ions. It has been hypothesized that this compound is uniquely able to insert a third sodium ion. However, the plausibility of this mechanism has remained ambiguous. Here, I use density-functional theory (DFT) with a hybrid functional to calculate the formation energies of various oxidation states and magnetic phases of the $Na_xMn[Mn(CN)_6]$ system. I confirm that the compound $Na_3Mn[Mn(CN)_6]$ is, indeed, thermodynamically stable. It contains manganese(I) and the sodium ions occupy the interfacial position of the lattice subcubes. I also provide strong evidence that the phase of the fully oxidized compound is charge-disproportionated $Mn^{II}[Mn^{IV}(CN)_6]$. I proceed to show that crystalline water increases reduction potential and that the hydrated compounds have theoretical crystal geometries and reduction potentials that closely match experiment. This work clarifies the charge-storage mechanism in a well-known but less-understood PBA.

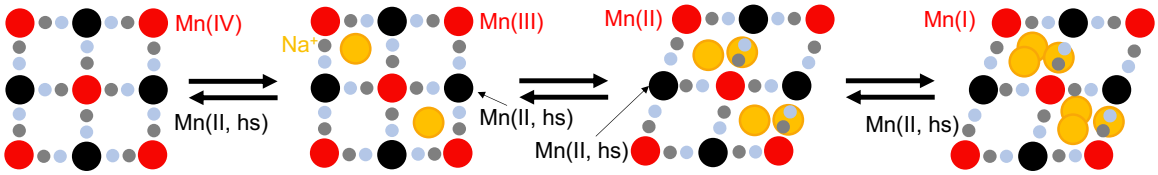

Figure 4.1: Electrochemical relationship among compounds examined. Schematic of the reversible insertion of three sodium ions (per formula unit) into the open-framework $Mn[Mn(CN)_6]$. Red atoms are carbon-coordinated manganese, black atoms are nitrogen-coordinated manganese, gray are carbon, light blue are nitrogen, gold are sodium.

4.1 An unexpected and unexplained specific capacity

Sodium manganese hexacyanomanganate, $Na_xMn[Mn(CN)_6]$, is a PBA of particular interest, because in 2014 Pasta and coworkers [1] observed a reversible specific capacity in sodium manganese hexacyanomanganate of 209 mA h g^{-1}. This is the highest-ever recorded specific capacity in a PBA. It is also 22% higher than the theoretical specific capacity that would be expected from the reversible (de)insertion of two sodium ions per formula unit. Furthermore, they observed three distinct voltage plateaus, at 3.5, 2.7, and 1.8 V versus the Na^+/Na redox couple. This is unusual for a PBA. The authors hypothesized that the extra capacity came from the insertion of a third sodium ion with the reduction of the carbon-coordinated manganese to manganese(I). The study included high-quality synchrotron X-ray diffraction (XRD) data, but the authors were unable to refine the structure sufficiently to determine conclusively the positions or number of the sodium ions. Work from Wessells and coworkers in 2018 [2] provided good X-ray spectroscopic evidence for the formation of monovalent manganese. The hypothetical relationship between the different oxidation states is shown schematically in Figure 4.1.

Here I investigate the material theoretically using density-functional theory (DFT) and a hybrid functional. First, I consider a pseudo-binary mixture of sodium atoms

with manganese hexacyanomanganate (empty of any interstitial sodium atoms). Many different, plausible magnetic moments and sodium-ion arrangements are considered. The lattice parameters and atom positions are fully relaxed and the total energy calculated. From this, the formation energies for the different phases are plotted and the convex hull is constructed to determine whether the hypothetical compound $Na_3Mn[Mn(CN)_6]$ is thermodynamically stable against separation into the $x = 2$ phase and sodium metal. I discuss the crystal structures of the simulated compounds and compare them to the experimental synchrotron X-ray diffractograms.

I then examine the compounds' electronic structure through their projected densities of states (PDOS). The atoms the orbitals of which give rise to the valence and conduction bands are identified. These data are compared to the atom-projected magnetic moments of the phases to determine the oxidation states of each compound. This determines on which manganese ion (if either) each reduction event is localized and whether monovalent manganese forms.

Finally, I investigate the effect of crystalline water in $Na_xMn[Mn(CN)_6] \cdot wH_2O$. The monohydrate and dihydrate of each oxidation state (using the ground-state magnetic moment from the dehydrated compound) are fully relaxed. Their crystal structures are compared to the experimental diffractograms. A phase diagram in (water activity, voltage) space is constructed from the grand potential, and the reduction potentials of the system are compared for water-poor and water-rich environments. Finally, an isoelectronic analog is briefly considered.

This is the first thorough theoretical investigation of the manganese hexacyanomanganate system, and it answers several interesting scientific questions about this technologically important battery-electrode material.

4.2 Convex hull of formation energies

In this section, I consider a pseudo-binary mixture of sodium atoms with the empty manganese hexacyanomanganate lattice (that is, the lattice containing no inserted sodium atoms), that can be written as

$$\mathrm{Mn[Mn(CN)_6]}{+}x\mathrm{Na} \rightarrow \mathrm{Na}_x\mathrm{Mn[Mn(CN)_6]} \tag{4.1}$$

in which x is the number of sodium atoms per formula unit and sodium is in some reference state—here, that is bcc sodium metal. The formation energy for such a mixture is given by [3, 4]

$$E_\mathrm{f}(x,S) = \frac{E(\mathrm{Na}_x\mathrm{Mn}^{\mathrm{S_N}}[\mathrm{Mn}^{\mathrm{S_C}}(\mathrm{CN})_6]) - E(\mathrm{Mn[Mn(CN)_6]}) - xE(\mathrm{Na})}{1+x} \tag{4.2}$$

Here, $S = S_C + S_N$ is the total magnetic moment of the unit cell. While the hexacyanoferrate PBAs can be modelled by assuming a ferromagnetic ordering between the carbon-coordinated iron and the nitrogen-coordinated ion, the hexacyanomanganates can have more exotic magnetic phases [5]. Various magnetic moments arise from several phenomena. First, spin configurations of the two ions in the structure can differ leading to magnetic moment; this was dealt with at length in Chapter 3. Also, different oxidation states are plausible a priori; for instance, in the ($x = 1$) phase, both oxidation states ($\mathrm{Mn}_\mathrm{C}^\mathrm{III}, \mathrm{Mn}_\mathrm{N}^\mathrm{II}$) and ($\mathrm{Mn}_\mathrm{C}^\mathrm{II}, \mathrm{Mn}_\mathrm{N}^\mathrm{III}$) might occur. (Throughout this chapter, $\mathrm{Mn_C}$ and $\mathrm{Mn_N}$ refer to the carbon-coordinated and nitrogen-coordinated manganese ions, respectively.) And charge disportionation should be considered, since it is is often observed in compounds containing high-spin manganese(III) [6]. Finally and for completeness, the atomic magnetic moments on the manganese ions can be either aligned or anti-aligned. These result in a wide variety of electronic configurations, which are tabulated for the oxidation states examined in Tables 4.1 through 4.5. Fortunately, many of these configurations share a total magnetic moment. So the magnetic moment can be fixed, the ground state determined, and the

Table 4.1: Plausible magnetic moments for $Mn[Mn(CN)_6]$

μ/μ_B	Mn_C	Mn_N	alignment
0	t_{2g}^4	t_{2g}^4	anti-aligned
2	t_{2g}^4	$t_{2g}^3 e_g^1$	anti-aligned
	t_{2g}^5	t_{2g}^3	anti-aligned
	t_{2g}^3	t_{2g}^5	anti-aligned
	t_{2g}^3	$t_{2g}^3 e_g^2$	anti-aligned
4	t_{2g}^4	t_{2g}^4	aligned
	t_{2g}^5	t_{2g}^3	aligned
	t_{2g}^3	t_{2g}^5	aligned
6	t_{2g}^4	$t_{2g}^3 e_g^1$	aligned
8	t_{2g}^3	$t_{2g}^3 e_g^2$	aligned

Table 4.2: Plausible magnetic moments for $NaMn[Mn(CN)_6]$

μ/μ_B	Mn_C	Mn_N	alignment
1	t_{2g}^4	t_{2g}^5	anti-aligned
	t_{2g}^5	t_{2g}^4	anti-aligned
3	t_{2g}^4	$t_{2g}^3 e_g^2$	anti-aligned
	t_{2g}^5	$t_{2g}^3 e_g^1$	anti-aligned
	t_{2g}^6	t_{2g}^3	n/a
	t_{2g}^4	t_{2g}^5	aligned
	t_{2g}^5	t_{2g}^4	aligned
5	t_{2g}^5	$t_{2g}^3 e_g^1$	aligned
7	t_{2g}^4	$t_{2g}^3 e_g^2$	aligned

actual electronic configuration resolved by examining the atom-projected magnetic moments. The formation energies for the phases are shown in Figure 4.2.

For the fully oxidized compound, $Mn[Mn(CN)_6]$, the two phases with $6\,\mu_B$ and $8\,\mu_B$ (where μ_B is the Bohr magneton) are degenerate and lowest in energy. For the compound $NaMn[Mn(CN)_6]$, the ground-state magnetic moment is $7\,\mu_B$ and is well separated in energy from the other magnetic phases. The compound $Na_2Mn[Mn(CN)_6]$ has a ground-state magnetic moment of $6\,\mu_B$. In this compound, the two sodium ions can occupy either edge-sharing faces of the interstitial subcube or opposite faces of the interstitial subcube. The edge-sharing phase is just 11 meV atom^{-1} lower in energy. The ground-state magnetic moment for the compound $Na_3Mn[Mn(CN)_6]$ is $5\,\mu_B$. For

Table 4.3: Plausible magnetic moments for $Na_2Mn[Mn(CN)_6]$

μ/μ_B	Mn_C	Mn_N	alignment
0	t_{2g}^5	t_{2g}^5	anti-aligned
2	t_{2g}^5	t_{2g}^5	aligned
	t_{2g}^6	t_{2g}^4	n/a
	t_{2g}^4	t_{2g}^6	n/a
	t_{2g}^4	$t_{2g}^4 e_g^2$	anti-aligned
4	t_{2g}^5	$t_{2g}^3 e_g^2$	anti-aligned
	t_{2g}^6	$t_{2g}^3 e_g^1$	n/a
6	t_{2g}^5	$t_{2g}^3 e_g^2$	aligned
	t_{2g}^4	$t_{2g}^4 e_g^2$	aligned

Table 4.4: Plausible magnetic moments for $Na_3Mn[Mn(CN)_6]$

μ/μ_B	Mn_C	Mn_N	alignment
1	t_{2g}^6	t_{2g}^5	n/a
	t_{2g}^5	t_{2g}^6	n/a
	t_{2g}^4	$t_{2g}^6 e_g^1$	anti-aligned
	t_{2g}^4	$t_{2g}^5 e_g^2$	anti-aligned
3	t_{2g}^5	$t_{2g}^4 e_g^2$	anti-aligned
	t_{2g}^4	$t_{2g}^6 e_g^1$	aligned
5	t_{2g}^6	$t_{2g}^3 e_g^2$	n/a
	t_{2g}^5	$t_{2g}^4 e_g^2$	aligned
	t_{2g}^4	$t_{2g}^5 e_g^2$	aligned

Table 4.5: Plausible magnetic moments for $Na_4Mn[Mn(CN)_6]$

μ/μ_B	Mn_C	Mn_N	alignment
0	t_{2g}^6	t_{2g}^6	n/a
	t_{2g}^5	$t_{2g}^6 e_g^1$	anti-aligned
	$t_{2g}^6 e_g^1$	t_{2g}^5	anti-aligned
2	t_{2g}^5	$t_{2g}^5 e_g^2$	anti-aligned
	t_{2g}^5	$t_{2g}^6 e_g^1$	aligned
	$t_{2g}^6 e_g^1$	t_{2g}^5	aligned
4	t_{2g}^6	$t_{2g}^4 e_g^2$	n/a
	$t_{2g}^6 e_g^1$	$t_{2g}^3 e_g^2$	anti-aligned
	t_{2g}^5	$t_{2g}^5 e_g^2$	aligned
6	$t_{2g}^6 e_g^1$	$t_{2g}^3 e_g^2$	aligned

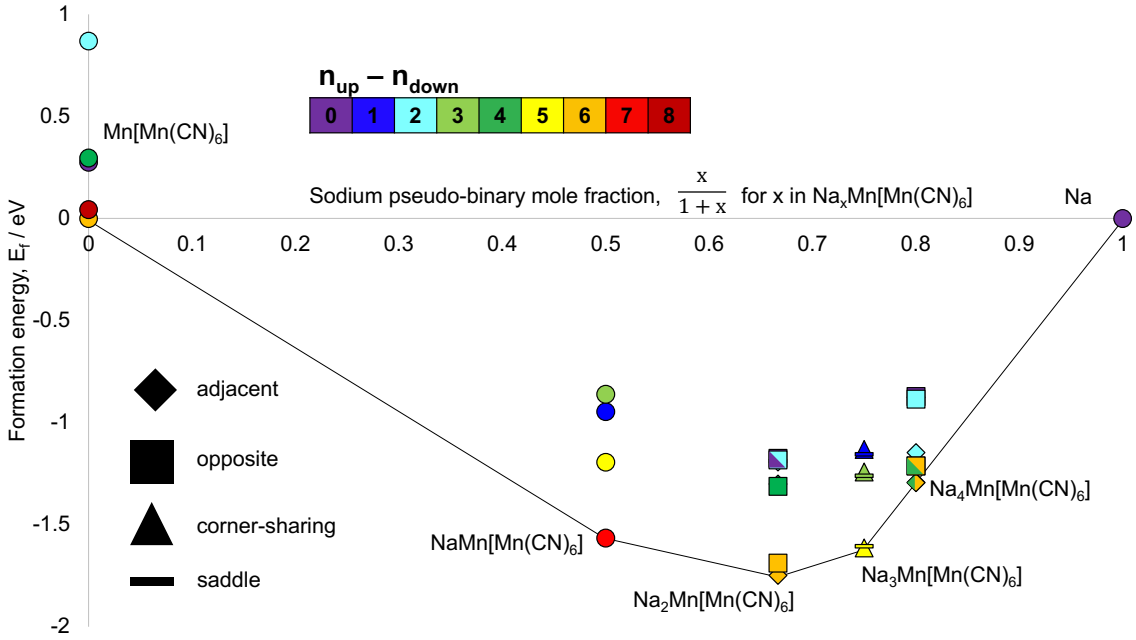

Figure 4.2: Formation energies for the $Na_xMn[Mn(CN)_6]$ system. The color of the data points signifies the total magnetic moment of the unit cell (in units of the Bohr magneton), which is equal to the difference between the number of majority- and minority-spin electrons. The convex hull is connected by the black line.

this compound, the three sodium ions can occupy either three faces of the interstitial subcube that share a corner or three faces in a "saddle" arrangement. These two phases are also essentially degenerate in energy (the corner-sharing arrangement is 2 meV atom^{-1} lower in energy). For $Na_4Mn[Mn(CN)_6]$, the two magnetic phases $\mu = 6\,\mu_B$ and $\mu = 4\,\mu_B$ are degenerate. (Note that the labels "adjacent" and "opposite" in this compound refer to the arrangement of subcube-faces that **do not** contain a sodium atom.) The adjacent arrangement of the empty faces is slightly lower in energy.

The compound $Na_3Mn[Mn(CN)_6]$ is part of the convex hull of formation energies for the pseudo-binary mixture of sodium with manganese hexacyanomanganate, so the experimental observation of the insertion of three sodium ions into the lattice is, indeed, thermodynamically reasonable.

The compound is stable relative to separation into $Na_2Mn[Mn(CN)_6]$ and sodium

metal. Other decomposition pathways at room temperature are unlikely. First, the sample from Pasta and coworkers was cycled reversibly. Second, the low-potential behavior of a closely related composition, sodium manganese hexacyanochromate ($Na_xMn[Cr(CN)_6]$), has previously been explored experimentally [7]. The lattice was found to be stable below the minimum potential (about 1.21 V versus Na^+/Na) that these calculations predict is necessary to insert the third sodium ion. Third, closely related PBA compositions have been found to be thermally stable up to 200 °C or higher [8].

Interestingly, $Na_4Mn[Mn(CN)_6]$ lies almost exactly on the convex hull. This indicates that insertion of a fourth sodium ion may be possible, but the reduction potential would be so close to metallic sodium as to make experimental confirmation challenging.

The chemical potentials of the various phases are plotted as a function of sodium chemical potential (referred to the chemical potential of solid sodium metal) in Figure 4.3. The chemical potential for a phase $Na_xMn[Mn(CN)_6]$ is given by

$$\mu_{Na_xMn[Mn(CN)_6]}(\mu_{Na}, x) = \mu_{Mn[Mn(CN)_6]} - x\mu_{Na} \tag{4.3}$$

in which $\mu_{Mn[Mn(CN)_6]}$ is the chemical potential of the lattice empty of any sodium ions and μ_{Na} is the chemical potential of sodium.

4.3 Crystal structures and sodium-ion positions

In this section, the ground-state crystal structures and the simulated diffraction patterns are compared to experiment. The positions of the the sodium ions are determined.

The phases' relaxed crystal structures are shown in Figure 4.4, and their simulated X-ray diffractograms are shown in Figure 4.5 along with the experimental synchrotron XRD data collected by Pasta and coworkers [1]. For the fully oxidized $Mn[Mn(CN)_6]$,

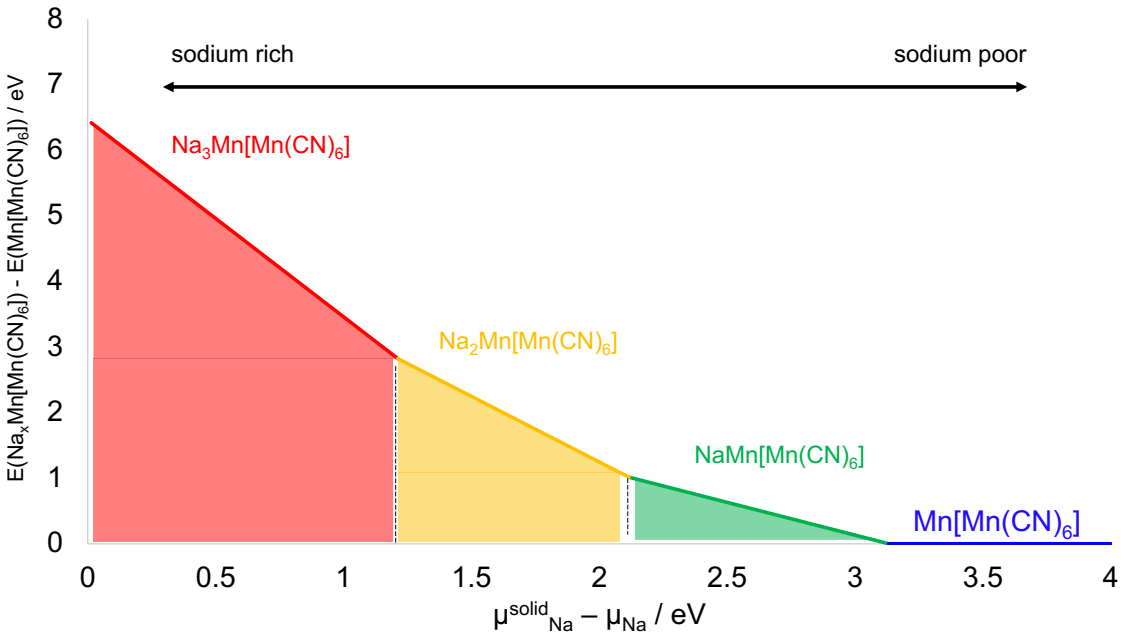

Figure 4.3: Chemical potentials for various oxidation states. The chemical potential (μ(x) of the phase $Na_xMn[Mn(CN)_6]$ is given by $\mu(x) = \mu(Na_xMn[Mn(CN)_6]) - \mu_{Na} - \mu(Mn[Mn(CN)_6])$. This is plotted as a function of the chemical potential of sodium, μ_{Na} (with a reference chemical potential, μ^0_{Na}). The stable phase at a given μ_{Na} is that which minimizes the chemical potential. The compound $Na_3Mn[Mn(CN)_6]$ is thermodynamically stable between about 1.2 and 0 V (versus Na^+/Na). Note that $Na_4Mn[Mn(CN)_6]$ becomes lower in energy almost exactly at 0 eV versus sodium metal.

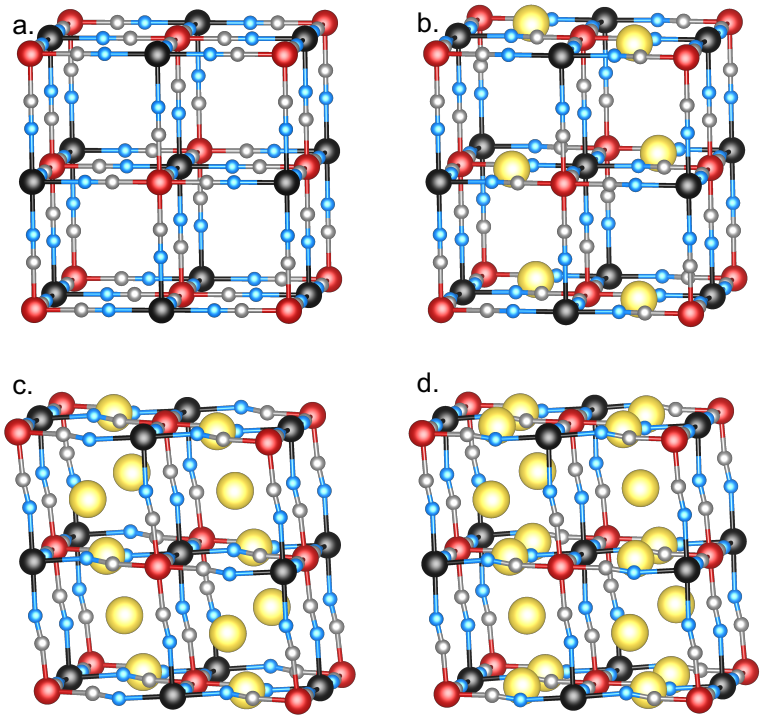

Figure 4.4: Ground-state crystal structures. Throughout, the carbon-coordinated manganese, nitrogen-coordinated manganese, carbon, nitrogen, and sodium atoms are shown in red, black, gray, light blue, and gold, respectively. The structures contain (a) $x = 0$, (b) $x = 1$, (c) $x = 2$ ("adjacent"), and (d) $x = 3$ ("saddle"), sodium ions per formula unit. Sodium ions occupy the faces separating neighboring subcubes. See Table 4.6 for associated lattice parameters.

the diffraction pattern for the $\mu = 8\,\mu_B$ phase is shown. This phase is face-centred cubic (space group $Fm\bar{3}m$) with a lattice parameter of 10.734 Å. The most intense peaks arise from the (101) reflection at 4.42° and the (202) reflection at 8.84°. (All patterns are simulated for an incident wavelength of $\lambda = 0.413737$ Å.) The $\mu = 6\,\mu_B$ phase for this compound has a tetragonal crystal structure with lattice parameters $a = 10.2$ Å and $c/a = 1.06$. The cubic crystal structure for $\mu = 8\,\mu_B$ is in excellent agreement with synchrotron XRD data. Figure 4.6 for the crystal structure and simulated XRD pattern of the $\mu = 6\,\mu_B$ phase.)

In the simulated pattern for the compound $NaMn[Mn(CN)_6]$, the most intense peaks arise from the (011) and (110) reflections at 4.42° and 4.44°, respectively. These are followed in intensity by the (022) and (220) reflections at 8.85° and 8.88°,

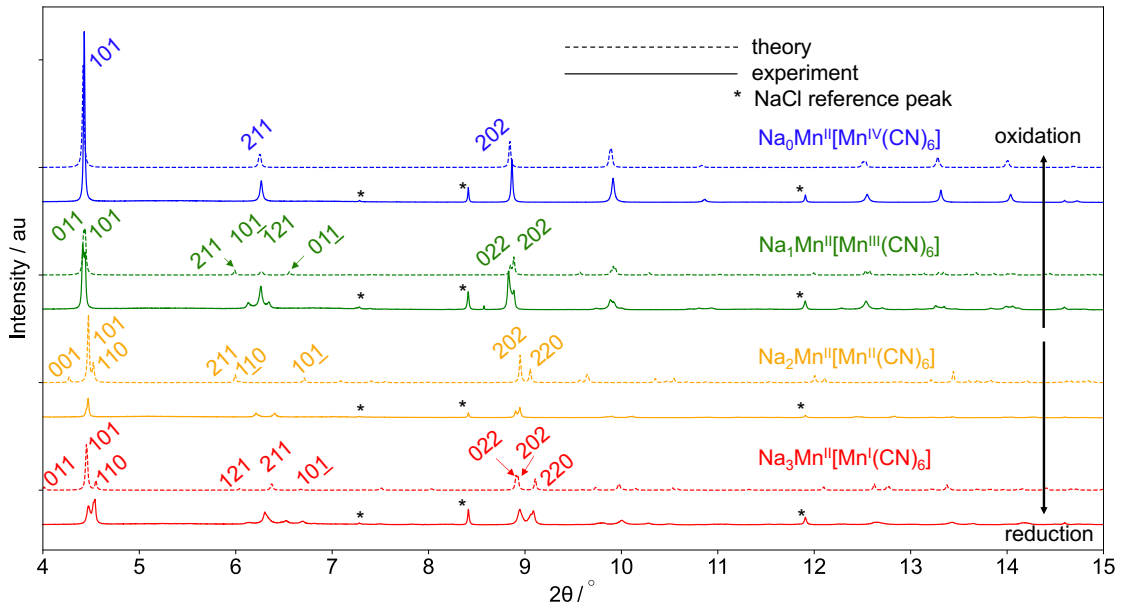

Figure 4.5: Simulated diffractograms and peak indices. The simulated (dashed line) and experimental (solid line, collected by Pasta and coworkers [1]) patterns are plotted for the four compounds $Mn[Mn(CN)_6]$, $NaMn[Mn(CN)_6]$, $Na_2Mn[Mn(CN)_6]$, and $Na_3Mn[Mn(CN)_6]$. Peak indices are included for the simulated patterns and the asterisk indicates sodium chloride reference peaks in the experimental data. The corresponding crystal structures are shown at the right.

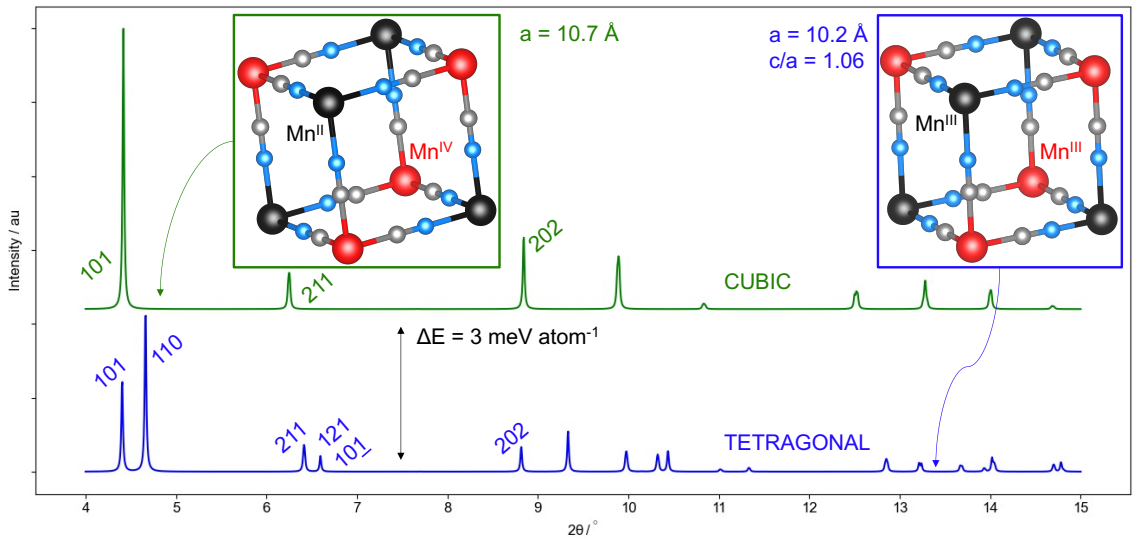

Figure 4.6: Crystal structures for two magnetic phases of $Mn[Mn(CN)_6]$. The $\mu = 6\mu_B$ phase (blue) is tetragonal due to a Jahn–Teller distortion arising from the high-spin, nitrogen-coordinated manganese(III). The $\mu = 8\ \mu_B$ phase is cubic. Disproportionation results in manganese(II) and manganese(IV), removing the Jahn–Teller distortion.

Table 4.6: Comparison of experimental and computational lattice parameters.

	Experimental		Computational		
	a / Å	$b = c$ / Å	a / Å	b / Å	c / Å
$Mn[Mn(CN)_6]$	10.706		10.736	10.732	
$NaMn[Mn(CN)_6]$	10.688	10.750	10.728	10.726	
$Na_2Mn[Mn(CN)_6]$	10.658	10.616	10.607	10.703	
$Na_3Mn[Mn(CN)_6]$	10.459	10.905	10.710	10.633	10.475

respectively. This, too, is in excellent agreement with the synchrotron XRD data.

The simulated pattern for $Na_2Mn[Mn(CN)_6]$ (adjacent arrangement of sodium ions) is also very similar to experiment. The doublet peak consisting of the (101) and (110) reflections is aligned with an experimental doublet with peaks centered at about 4.45° and 4.47°. Similarly, the simulated (202) and (220) reflections are close to two experimental peaks at about 9°. The main difference is the presence of the (001) reflection at 4.27° in the simulated pattern. This reflection arises from long-range ordering of sodium ions, an unphysical feature of modeling a single unit cell with periodic boundary conditions. Also, the separation between the (211) and $(10\bar{1})$ reflections is wider in the computational data (0.715°) compared to the experimental data (about 0.25°).

For $Na_3Mn[Mn(CN)_6]$ (saddle arrangement of sodium ions), the simulated data also broadly match the empirical data. The model has three reflections, (011), (101), and (110), which match an experimental triplet at 4.47°, 4.52°, and 4.54°. The simulated (022), (202), and (220) reflections also correspond closely to another experimental triplet with peaks at 8.95°, 9.07°, and 9.09°. Table 4.6 is a summary of the computed lattice parameters.

4.4 Electronic structures and oxidation states

The projected densities of states (PDOS) and electronic configurations consistent with the atom-projected magnetic moments for the four compounds are shown in Figure 4.7. For the fully oxidized compound, $Mn[Mn(CN)_6]$, the $\mu = 8\,\mu_B$ phase has

atom-projected magnetic moments of $\mu_{\mathrm{Mn_C}} = 3.023\,\mu_\mathrm{B}$ and $\mu_{\mathrm{Mn_N}} = 4.567\,\mu_\mathrm{B}$. This is consistent with an electronic configuration of ($\mathrm{Mn_C}(t_{2g}^3)$, $\mathrm{Mn_N}(t_{2g}^3 e_g^2)$). In this phase, the nitrogen-coordinated manganese is high spin and the two manganese ions are spin aligned. The two manganese ions are in oxidation states ($\mathrm{Mn_C}$(IV), $\mathrm{Mn_N}$(II)), so this phase is charge disproportionated. This is in agreement with experiment [9]. The PDOS shows that the conduction-band states arise from spin-down, t_{2g} orbitals on the carbon-coordinated manganese. The electronic configuration for the nearly degenerate $\mu = 6\,\mu_\mathrm{B}$ is ($\mathrm{Mn_C}(t_{2g}^4)$, $\mathrm{Mn_N}(t_{2g}^3 e_g^1)$). This non-disproportionated phase, ($\mathrm{Mn_C}$(III), $\mathrm{Mn_N}$(III)), has a singly occupied e_g orbital which gives rise to a Jahn–Teller distortion and the tetragonal geometry discussed above.

On reduction to the compound $\mathrm{NaMn[Mn(CN)_6]}$, the spin-down t_{2g} orbitals become partially occupied; both the valence- and conduction-bands arise from spin-down, t_{2g} orbitals on the carbon-coordinated manganese. The atom-projected magnetic moments for this $\mu = 7\,\mu_\mathrm{B}$ phase are $\mu_{\mathrm{Mn_C}} = 2.013\,\mu_\mathrm{B}$ and $\mu_{\mathrm{Mn_N}} = 4.572\,\mu_\mathrm{B}$; the orbital occupations are ($\mathrm{Mn_C}(t_{2g}^4)$, $\mathrm{Mn_N}(t_{2g}^3 e_g^2)$). In this phase, the nitrogen-coordinated carbon remains high spin and the two manganese ions remain spin aligned.

Further reduction to the compound $\mathrm{Na_2Mn[Mn(CN)_6]}$ adds an electron to the a spin-down, carbon-coordinated-manganese t_{2g} orbital, resulting in increased density of states in the valence band arising from these orbitals. The conduction band still originates from these same, carbon-coordinated-manganese, spin-down t_{2g} orbitals (albeit with lower density of states). The atom-projected magnetic moments are $\mu_{\mathrm{Mn_C}} = 1.075\,\mu_\mathrm{B}$ and $\mu_{\mathrm{Mn_N}} = 4.567\,\mu_\mathrm{B}$ and the electronic configuration is ($\mathrm{Mn_C}(t_{2g}^5)$, $\mathrm{Mn_N}(t_{2g}^3 e_g^2)$). The nitrogen-coordinated manganese atom is still in a high spin configuration and the manganese ions are still spin aligned.

Reduction to the $\mathrm{Na_3Mn[Mn(CN)_6]}$ fully occupies the t_{2g} orbitals on the carbon-coordinated manganese atom, so the valence band arises from these orbitals. The

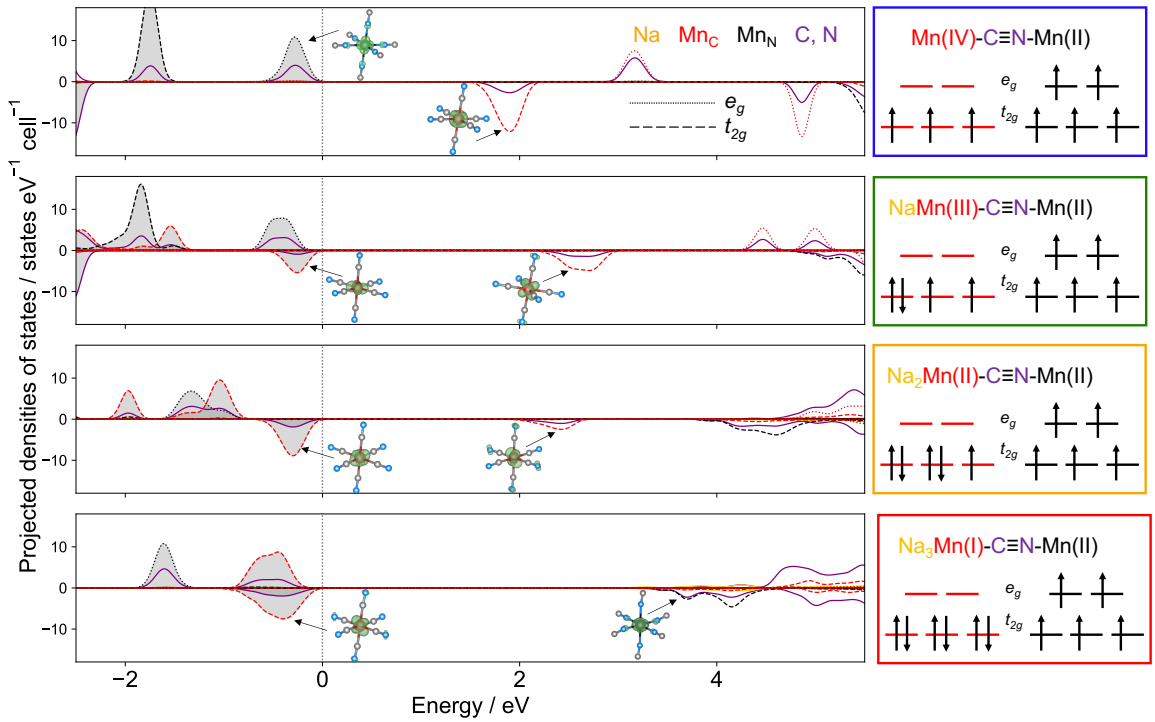

Figure 4.7: Electronic structures for $Na_xMn[Mn(CN)_6]$. Projected densities of states (PDOS), band-decomposed charge densities, and electronic configurations are shown for phases with 0, 1, 2, and 3 sodium ions per formula unit from top to bottom. In the PDOS, red, black, purple, and gold lines refer to states arising from orbitals on the carbon-coordinated manganese, nitrogen-coordinated manganese, cyanide ligands, and sodium, respectively. Solid, dashed, and dotted lines refer to states arising from (s and p), t_{2g}, and e_g orbitals, respectively. The charge-density isosurfaces are for the valence-band and conduction-band states.

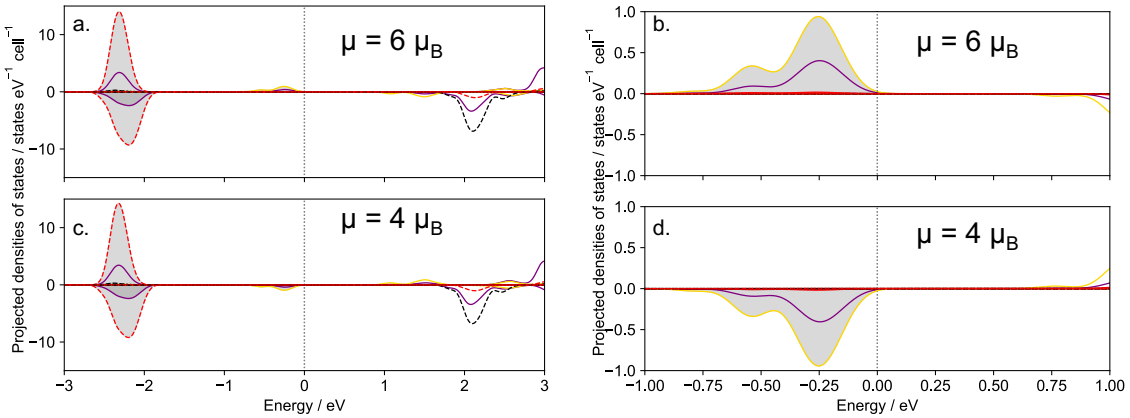

Figure 4.8: Projected density of states for $Na_4Mn[Mn(CN)_6]$. Red, black, purple, and gold lines refer to states arising from orbitals on the carbon-coordinated manganese atom, nitrogen-coordinated manganese atom, cyanide ligands, and sodium atom(s), respectively. Solid, dashed, and dotted lines refer to states arising from (s and p), t_{2g}, and e_g orbitals, respectively. The $\mu = 6\,\mu_B$ phase (upper plot) and $\mu = 4\,\mu_B$ phase (lower plot) differ only in the spin-orientation of the electron in the sodium-projected valence state.

atom-projected magnetic moments are $\mu_{Mn_C} = 0.094\,\mu_B$ and $\mu_{Mn_N} = 4.561\,\mu_B$. This implies an orbital occupation of ($Mn_C(t_{2g}^6)$, $Mn_N(t_{2g}^3 e_g^2)$) with high-spin nitrogen-coordinated manganese.

Figure 4.8 shows the PDOS for the possibly stable compound $Na_4Mn[Mn(CN)_6]$. Interestingly, its valence-band states arise from sodium orbitals. This indicates that on addition of a fourth sodium ion, the accompanying electron does not reduce either of the lattice manganese ions; rather, it is localized on the sodium atom.

So the high specific capacity in sodium manganese hexacyanomanganate originates, in part, from the fact that $Na_2Mn[Mn(CN)_6]$ has a relatively low-energy conduction-band state arising from an unoccupied t_{2g} orbital on the manganese atom coordinated to carbon. Reduction to $Na_3Mn[Mn(CN)_6]$ results in the particularly stable electronic configuration ($Mn_C(t_{2g}^6)$, $Mn_N(t_{2g}^3 e_g^2)$). The nitrogen-coordinated manganese ion remains manganese(II) over the course of three reduction events from $Mn[Mn(CN)_6]$ to $Na_3Mn[Mn(CN)_6]$. The carbon-coordinated manganese atom is the exclusive redox center in this system. Furthermore, the nitrogen-coordinated man-

ganese is always in a high-spin configuration, and the two manganese ions are always ferromagnetically aligned. (Though in $Na_3Mn^{II}[Mn^{I}(CN)_6]$, the carbon-coordinated manganese atom has a negligible magnetic moment.)

4.5 Effect of composition: crystalline water and isoelectronic lattice ions

This section examines the effect of two changes to composition. First, crystalline water molecules are introduced into the structure and changes to the crystal geometry and energetics are discussed. Second, an isoelectronic composition, sodium iron hexacyanochromate, is examined as a possible composition also capable of inserting a third ion.

Water is taken up into the crystal structure of the PBAs [10, 11]. Aggressive drying techniques are often used when PBA electrodes are being optimized to prevent the reaction of water with the lattice at more extreme potentials [12, 13].

Here the hydrated compounds, $Na_xMn[Mn(CN)_6] \cdot wH_2O$, for $w \in \{1, 2\}$ are considered. The crystal structures after explicit inclusion of the water molecules and full relaxation of the lattice vectors and atom positions are shown in Figure 4.9. (The crystal geometries of the fully dehydrated compounds ($w = 0$) are shown in Figure 4.5 for reference.)

In $Mn[Mn(CN)_6] \cdot 1H_2O$ the water occupies the centers of the subcubes. In the more hydrated phase, $Mn[Mn(CN)_6] \cdot 2H_2O$, the electric dipole moments of the two water molecules are aligned.

In $NaMn[Mn(CN)_6] \cdot 1H_2O$, the water molecule continues to occupy the interstitial position while sodium continues to occupy the interfacial site. The water molecule's electric dipole moment points away from the positively charged sodium ion. (That is, the oxygen atom, with its partial negative charge, is oriented toward the positively charge sodium ions, while the hydrogen atoms, with their partial positive charge, are

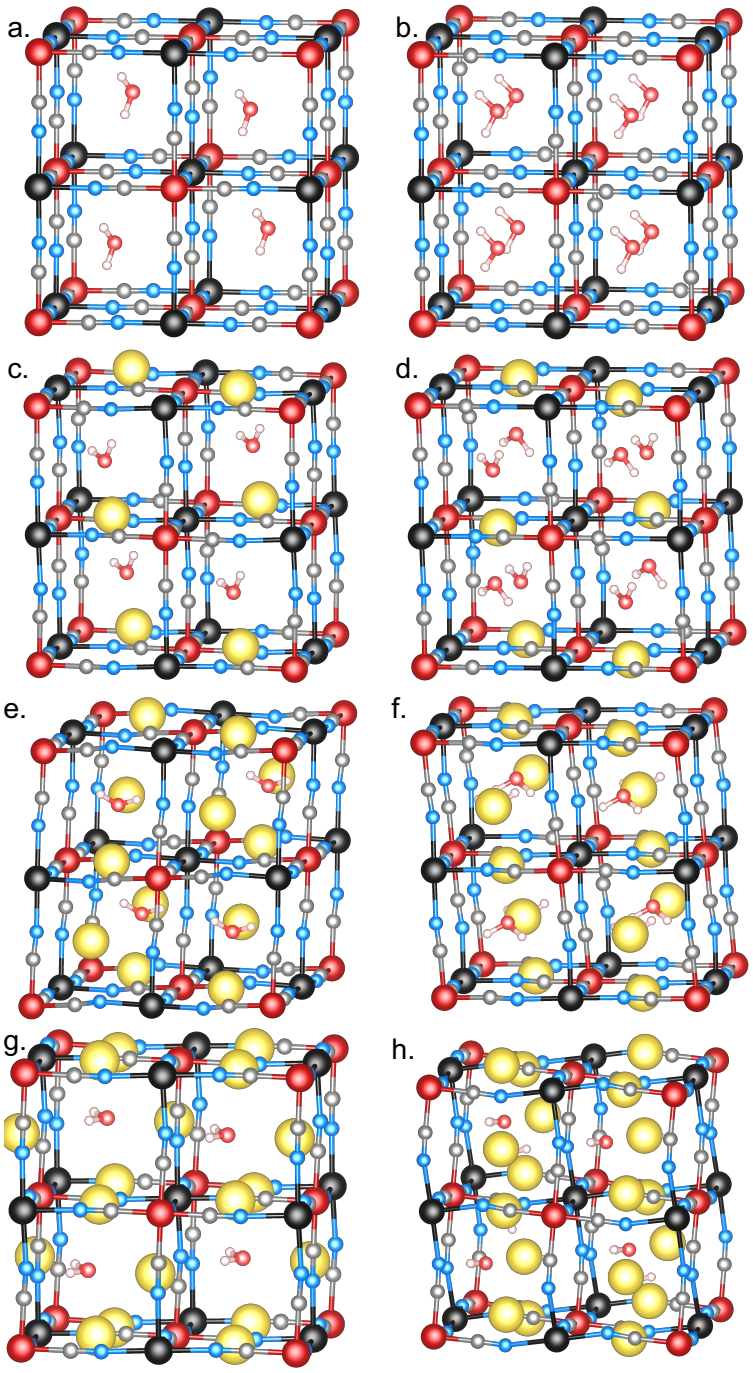

Figure 4.9: Relaxed crystal structures for the $Na_xMn[Mn(CN)_6] \cdot wH_2O$ system. The subplots are (a) $x = 0$, $w = 1$; (b) $x = 0$, $w = 2$; (c) $x = 1$, $w = 1$; (d) $x = 1$, $w = 2$; (e) $x = 2$, $w = 1$, ; (f) $x = 2$, $w = 2$; (g) $x = 3$, $w = 1$; (h) $x = 3$, $w = 2$.

oriented away from the sodium ions.) The O–Na distance is 2.25 Å. In the more hydrated $NaMn[Mn(CN)_6] \cdot 2H_2O$, both O–Na distances are 2.33 Å—slightly larger than in the monohydrate. In this compound the water molecules' electric dipole moments are anti-aligned with respect to their 6 nearest-neighbor water molecules in the adjoining subcubes.

The monohydrate of the more reduced phase, $Na_2Mn[Mn(CN)_6] \cdot 1H_2O$, still has water at the center of the subcube and sodium ions in adjacent faces, forming an Na–O–Na angle of 93°. The two O–Na distances are 2.40 and 2.41 Å. The water molecule's electric dipole moment points about equally away from both sodium ions (more formally, the moment bisects the Na–O–Na angle). Addition of a second water molecule results in an average O–Na distance of 2.47 Å. The water molecules' electric dipoles are anti-aligned with those of their nearest neighbors.

In $Na_3Mn[Mn(CN)_6] \cdot 1H_2O$, the three O–Na distances are 2.56, 2.57, and 2.59 Å for an average of 2.57 Å. The water electric dipole is directed normal to and away from the sodium ion in the middle face of the "saddle" arrangement of the occupied faces (formally, it bisects the angle formed by the three sodium ions). In $Na_3Mn[Mn(CN)_6] \cdot 2H_2O$ the average O–Na distance is 2.33 Å , and the water molecules' electric dipole moments are at approximately 90°.

The effect of the presence of crystalline water on the lattice geometry is best understood by examining the simulated diffraction patters show in Figure 4.10. For $Mn[Mn(CN)_6] \cdot wH_2O$, the addition of one and then two waters breaks the cubic symmetry; the (101) and (110) reflections give rise to two peaks at 4.40° and 4.44° in Figure 4.10. They give rise to only one peak for the dehydrated, cubic compound. The experimental data is well fit by a cubic symmetry, so the dehydrated compound ($w = 0$) matches the empirical data best.

In the next oxidation state, $NaMn[Mn(CN)_6] \cdot wH_2O$, the peaks corresponding to the (211) and $(01\overline{1})$ reflections move progressing closer to the (121) peak by moving

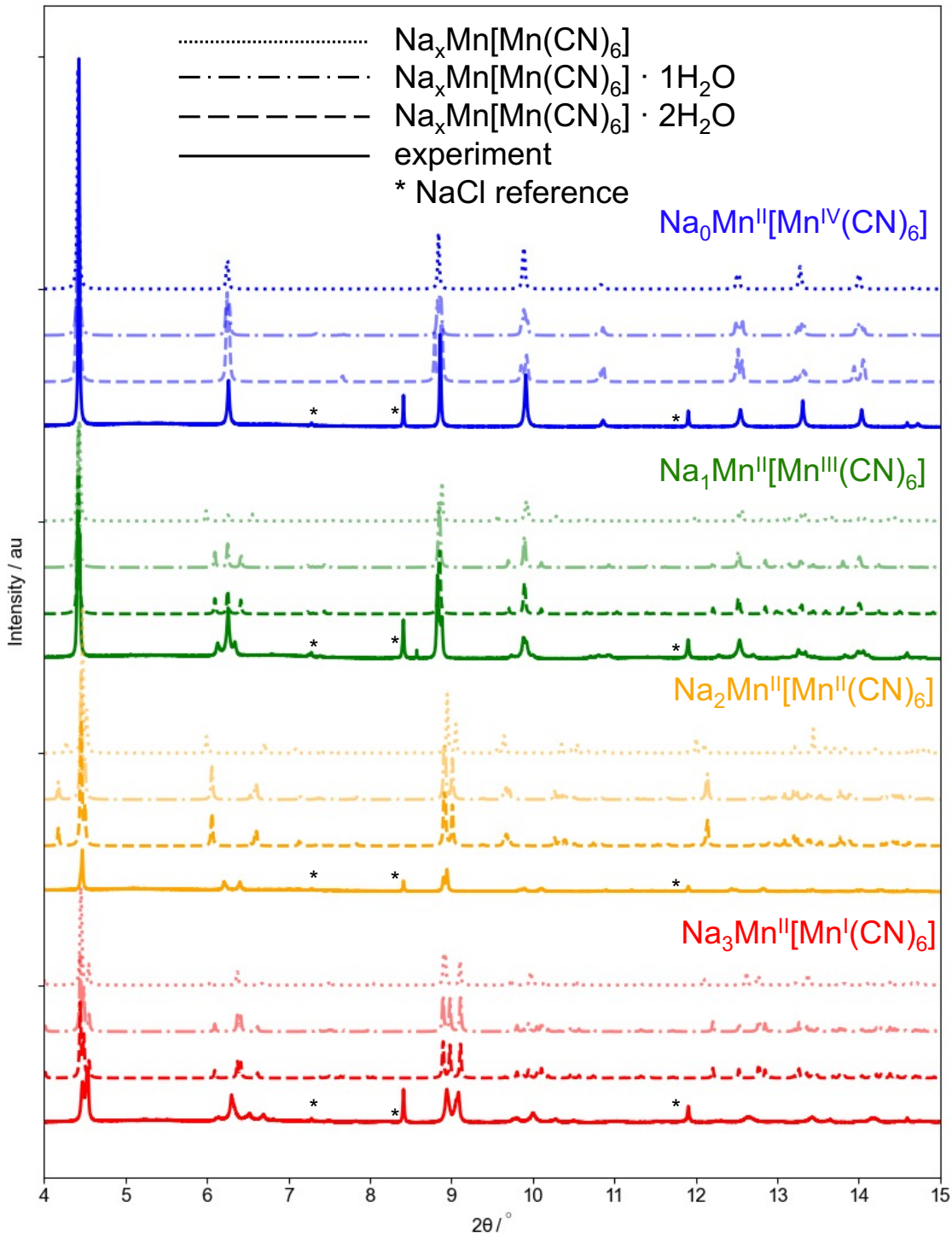

Figure 4.10: Simulated diffractograms for various hydration states. Each oxidation state has one simulated pattern that is darker than the other two hydration states: $Mn[Mn(CN)_6]$, $NaMn[Mn(CN)_6] \cdot 2H_2O$, $Na_2Mn[Mn(CN)_6] \cdot 2H_2O$, and $Na_3Mn[Mn(CN)_6] \cdot 2H_2O$. These are the hydration states that best match experimental reduction potentials.

to higher and lower values of 2θ, respectively. The separation between them begins at 0.57° in the dehydrated ($w = 0$) phase. It decreases to 0.31° in the ($w = 2$) phase, compared to about 0.23° in the experimental diffractogram. So of all the hydration states, $NaMn[Mn(CN)_6] \cdot 2H_2O$ best recreates the experimental diffractogram for the compound containing 1 sodium ion per formula unit.

For two sodium ions, a similar effect is seen. The large separation between the peaks between 6° and 7° decreases as water is added, in improving agreement with experiment. A similar effect is present for the peaks at about 7°. In this oxidation state, too, the diffractogram for the two-water phase is in best agreement with experiment.

Finally, for the compounds $Na_3Mn[Mn(CN)_6] \cdot wH_2O$, one interesting effect of water on the simulated diffractogram is the change in the peaks around 9°. The fully dehydrated pattern has two peaks at about 8.91° and one peak at about 9.11°, whereas the experimental patter has one peak at the first position 2θ and one peak at the second position. Adding water has the effect of separating the two peaks at about 8.91° by pushing one of them toward higher 2θ. While this peak is not positioned as high as about 9.1° (the experimental position) even in the dihydrate phase, the addition of water improves the agreement with experiment. Furthermore, the relative intensities of the peaks at about 4.5° better reflect experiment in the ($w = 2$) state. So the simulated pattern $Na_3Mn[Mn(CN)_6] \cdot 2H_2O$ is also closest to experiment.

So the hydration states in best agreement with experimental synchrotron XRD data are $Mn[Mn(CN)_6]$, $NaMn[Mn(CN)_6] \cdot 2H_2O$, $Na_2Mn[Mn(CN)_6] \cdot 2H_2O$, and $Na_3Mn[Mn(CN)_6] \cdot 2H_2O$. I turn now to examine the energetics of these hydrated phases and the construction of an appropriate phase diagram. To begin, I derive an expression relating the grand potential to the DFT-calculable quantities following the procedure of reference [14].

The ground state for the phase $Na_xMn[Mn(CN)_6] \cdot wH_2O$ is that coordinate, (x, w), which minimizes an appropriate thermodynamic potential. For a battery elec-

trode, the appropriate thermodynamic function is the grand potential, because the electrode can exchange sodium particles with the counter electrode and can exchange water particles with the aqueous or wet-organic electrolyte. The grand potential, Φ, is given by

$$\Phi = U - TS - \Sigma_i \mu_i N_i \tag{4.4}$$

where U is the internal energy, T is the thermodynamic temperature, S is the entropy, μ_i is the chemical potential of the i^{th} species and N_i is the number (or amount) of the i^{th} species. The summation runs over every species, i, present. Separately, the Gibbs energy, G, can written as

$$G = U - TS + pV \tag{4.5}$$

where U, T, and S are as above, p is the pressure, and V is the volume. So then

$$\Phi = G - pV - \Sigma_i \mu_i N_i. \tag{4.6}$$

I assume that any volume difference between the phases is small enough to make any differences in the pV-energy terms negligibly small relative to the G and $\Sigma_i \mu_i N_i$ terms. I sum over the three species: sodium metal, liquid water, and the manganese hexacyanomanganate lattice (empty of sodium or water), and write

$$\Phi = G_{\mathrm{Na}_x\mathrm{Mn[Mn(CN)_6]}\cdot w\mathrm{H_2O}} - \mu_{\mathrm{Mn[Mn(CN)_6]}} - x\mu_{\mathrm{Na}} - w\mu_{\mathrm{H_2O}}. \tag{4.7}$$

I assume that at 0 K the Gibbs energy and the chemical potential of the empty lattice, $\mu_{\mathrm{Mn[Mn(CN)_6]}}$, are well approximated by the DFT total energy. Since the chemical potential of the empty lattice, $\mu_{\mathrm{Mn[Mn(CN)_6]}}$, is a constant I can set it to zero. (Said differently, since it is a constant added to all phases, it cannot affect which phase is the ground state). Finally, recognizing that in equation 4.7 the grand potential for a given (x, w) is a function of both the chemical potential of sodium and the chemical potential of water, I write

$$\Phi(\mu_{\mathrm{Na}}, \mu_{\mathrm{H_2O}}, x, w) = G_{\mathrm{Na}_x\mathrm{Mn[Mn(CN)_6]}\cdot w\mathrm{H_2O}} - x\mu_{\mathrm{Na}} - w\mu_{\mathrm{H_2O}}. \tag{4.8}$$

The chemical potential of water and the chemical potential of sodium can be related to more readily available experimental values according to the following equations. The chemical potential of water, μ_{H_2O}, is

$$\mu_{H_2O} = \mu^0_{H_2O} + k_B T \ln(a_{H_2O}) \tag{4.9}$$

in which $\mu^0_{H_2O}$ is the reference chemical potential for water and a_{H_2O} is the activity of water in a liquid electrolyte. The sodium chemical potential is related to the electric potential (or voltage), V, by

$$V = -\frac{\mu_{Na} - \mu^0_{Na}}{e} \tag{4.10}$$

where μ^0_{Na} is the reference chemical potential of sodium metal and e is the fundamental charge.

Determining the (x, w) value that minimizes the grand potential at various values for the activity of water and the voltage allows for the construction of a phase diagram in (a_{H_2O}, V) space. (This is similar in many ways to a Pourbaix diagram which is a kind of phase diagram for metals and metal oxides in (a_{H^+}, V) space.) The phase diagram for the $Na_xMn[Mn(CN)_6] \cdot wH_2O$ system is shown in Figure 4.11a.

At the lowest chemical potential for water (that is, for the driest electrolyte), the dehydrated ($w = 0$) phase is most stable for all four oxidation states ($x = 0$ to $x = 3$). At the highest chemical potential for water (that is, the wettest electrolyte) the most stable phase has two water molecules per formula unit for $x = 1, 2, 3$. For the $x = 0$ compound, though, the dehydrated compound remains that most stable, and neither $Mn[Mn(CN)_6] \cdot H_2O$ nor $Mn[Mn(CN)_6] \cdot 2H_2O$ appears in the phase diagram. The intermediate hydration states, $NaMn[Mn(CN)_6] \cdot H_2O$, $Na_2Mn[Mn(CN)_6] \cdot H_2O$, and $Na_3Mn[Mn(CN)_6] \cdot H_2O$, are the ground state at intermediate water chemical potentials.

Water has the effect of increasing the reduction potential in closely related PBA compositions [14], and it also increases the reduction potential of this $Na_xMn[Mn(CN)_6]$

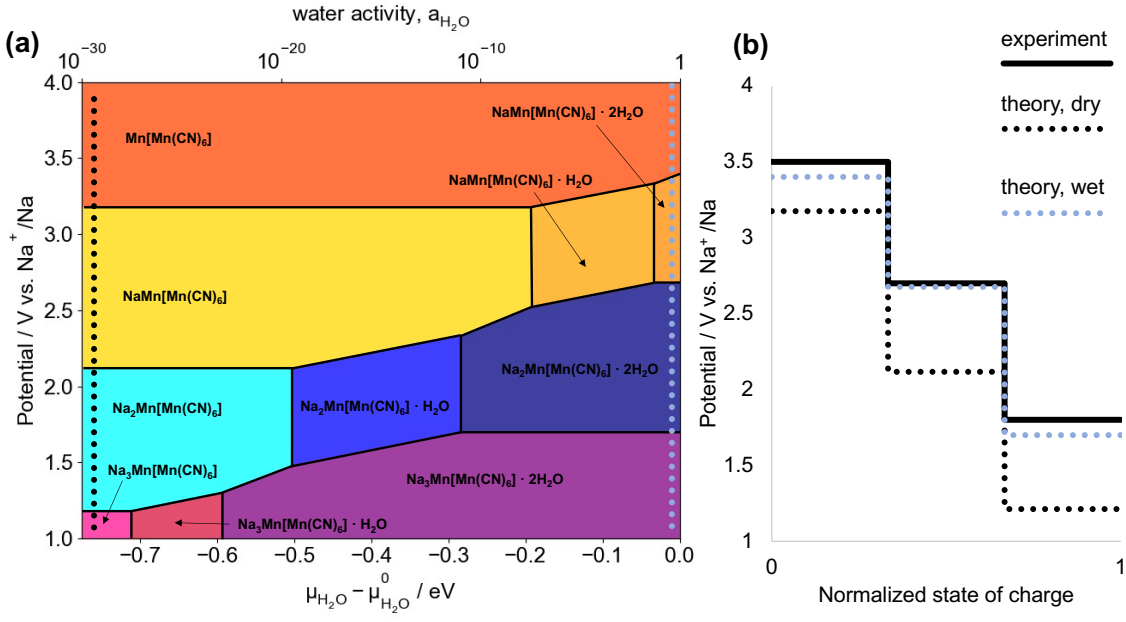

Figure 4.11: Phase diagram and simulated galvanostatic discharge curve. In (a), the stable phase of the $Na_xMn[Mn(CN)_6] \cdot wH_2O$ system is plotted as a function of voltage and chemical potential of water at 300 K. In (b), the simulated galvanostatic discharge curves are plotted for a drier electrolyte (lower chemical potential for water) (black dotted line) and for a wetter electrolyte (higher chemical potential for water) (blue dotted line). The average experimental potential is plotted from Pasta and coworkers for comparison.

$\cdot w\mathrm{H_2O}$ system as shown in Figure 4.11b. The calculated reduction potential for the dehydrated $\mathrm{Mn^{II}[Mn^{IV/III}(CN)_6]}$ couple is 3.13 V versus $\mathrm{Na^+/Na}$; this underestimates the observed average potential of about 3.5 V by 370 mV. The $\mathrm{Mn^{II}[Mn^{III/II}(CN)_6]}$ has a calculated reduction potential of 2.12 V versus $\mathrm{Na^+/Na}$, which is 580 mV below the observed average value of about 2.7 V. Finally, the $\mathrm{Mn^{II}[Mn^{II/I}(CN)_6]}$ couple is computationally at 1.21 V versus $\mathrm{Na^+/Na}$, while the average experimental data is around 1.8 V, or 590 mV higher. However, the reduction potentials for the hydrated materials at higher chemical potential are 3.4, 2.7, and 1.7 V versus $\mathrm{Na^+/Na}$. These are in much better agreement with experiment, underestimating observed values by 100, 0, and 100 mV. To emphasize, the phases in the simulated galvanostatic curve that best match the experimental are $\mathrm{Mn[Mn(CN)_6]}$, $\mathrm{NaMn[Mn(CN)_6]\cdot 2H_2O}$, $\mathrm{Na_2Mn[Mn(CN)_6]\cdot 2H_2O}$, and $\mathrm{Na_3Mn[Mn(CN)_6]\cdot 2H_2O}$. And these are the same phases that best match the crystallographic data discussed above.

At finite temperature, the effect of the configuration entropy, S_{config}, of water on the Gibbs energy of a phase, $G_{\mathrm{Na}_x\mathrm{Mn[Mn(CN)_6]}\cdot w\mathrm{H_2O}}$ can be included by subtracting the term TS_{config} from the DFT total energy. Since the configuration entropy is non-negative, this term can lower the grand potential for a hydrated phase according to equation 4.8. The configuration entropy is given by

$$S_{\mathrm{config}} = k_{\mathrm{B}} \ln(\Omega) \tag{4.11}$$

in which Ω is the number of arrangements for the water molecule. For $w = 1$, the single water molecule can occupy one of two subcube centers in the simulation cell. This gives a configuration entropy of $S_{\mathrm{config}} = k_{\mathrm{B}} \ln(2) = 5.97 \times 10^{-5}\,\mathrm{eV\,K^{-1}}$. At 300 K, this lowers the grand potential of the $w = 1$ phases by 17.9 meV. Incorporating this effect into the phase diagram in Figure 4.11 has the effect of slightly increasing the areas of the $w = 1$ phases.

In the $w = 0$ case, there is only one "arrangement", so $\Omega = 1$ and $S_{\mathrm{config}} = 0$. For

the $w = 2$ case, both available sites (that is, the subcube centers) are occupied by water molecules, so $\Omega = 1$ and $S_{\text{config}} = 0$ in this case as well.

Finally, this chapter ends with a discussion of an interesting analog to manganese hexacyanomanganate: iron hexacyanochromate, $Fe[Cr(CN)_6]$. Because the compound $Mn^{II}[Mn^{IV}(CN)_6]$ is disproportionated, it is isoelectronic to $Fe^{III}[Cr^{III}(CN)_6]$. In both compounds the carbon-coordinated ion is in a t_{2g}^3 configuration and the nitrogen-coordinated ion is in a $t_{2g}^3 e_g^2$ configuration. Iron hexacyanochromate, then, is a promising hypothetical candidate for also observing the reversible insertion of three sodium ions and three reduction events at the carbon-coordinated chromium. A model of the reduced compound, $NaFe[Cr(CN)_6]$, though, predicts reduction at the nitrogen-coordinated iron. The subsequent two reductions happen at the carbon-coordinated chromium and, indeed, the compound $Na_3Fe[Cr(CN)_6]$ is stable against phase separation into $Na_2Fe[Cr(CN)_6]$ and sodium metal, as shown in the blue data points in Figure 4.12. However, the whole sodium iron hexacyanochromate system is only metastable relative to sodium chromium hexacyanoferrate, $Na_xCr[Fe(CN)_6]$. That is, $Fe[Cr(CN)_6]$ is susceptible to ligand isomerization in which the cyanide bonds rotate so that the iron becomes carbon-coordinated and chromium becomes nitrogen-coordinated. And, as Figure 4.12 shows, the convex hull of formation energies is formed by $Cr[Fe(CN)_6]$, $NaCr[Fe(CN)_6]$, $Na_2Cr[Fe(CN)_6]$, and sodium metal; the three-sodium phase lies above the convex hull for this system. Ligand isomerization has been observed in this [15] and similar analogs previously. However, the reaction can take more than an hour at room temperature, and the kinetics of the process are poorly understood. It may be possible to prepare $Fe[Cr(CN)_6]$ and cycle it reversibly to demonstrate the insertion of three sodium ions before it decomposes.

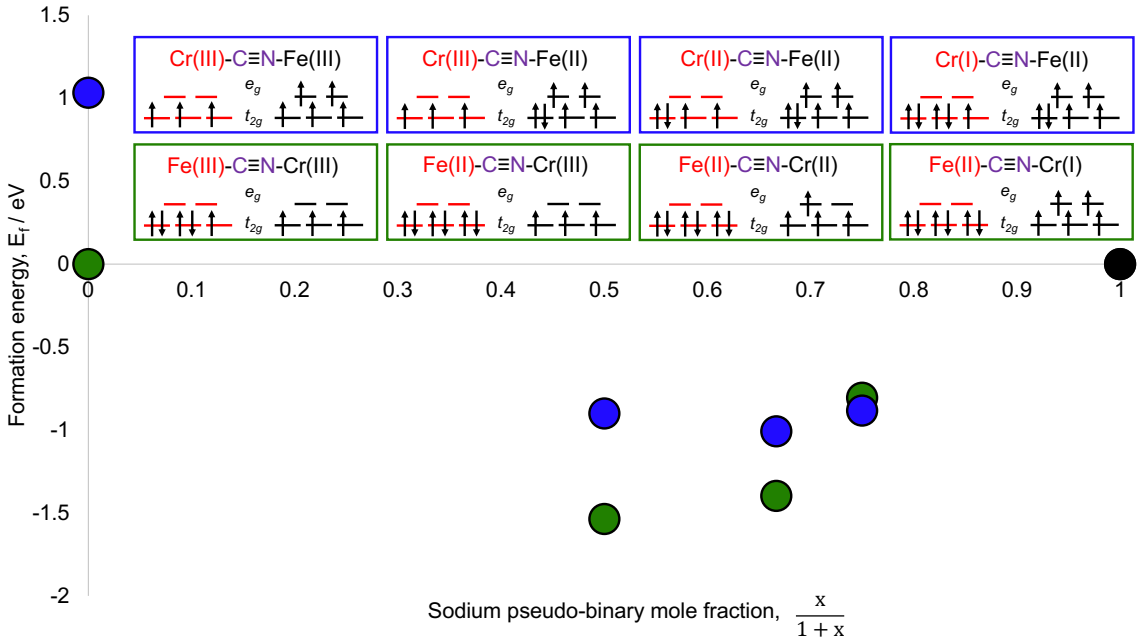

Figure 4.12: Formation energies for the $NaCrFe(CN)_6$ system. At the top are shown the electronic, orbital configurations for the compounds. Iron hexacyanochromate is shown in blue and chromium hexacyanoferrate is shown in green. Below the formation energies for the compounds are plotted.

4.6 Conclusions

In this chapter, I examined the PBA sodium manganese hexacyanomanganate to understand the technologically important origin of the material's unexpectedly high specific capacity using DFT with a hybrid functional. First, the formation energies of various plausible magnetic phases and sodium-ion arrangements of a pseudo-binary mixture of sodium and $Mn[Mn(CN)_6]$ were calculated for the first time. The compound $Na_3Mn[Mn(CN)_6]$ is part of the convex hull of formation energies, indicating that the insertion of a third sodium ion into the structure is thermodynamically stable against phase separation into sodium metal and $Na_2Mn[Mn(CN)_6]$. Interestingly, the compound $Na_4Mn[Mn(CN)_6]$ lies essentially on the convex hull, indicating that careful experimentation may allow one to observe a fourth sodium-ion-insertion event.

The simulated diffraction patterns for the various phases are in very good agreement with synchrotron XRD data. For $Mn[Mn(CN)_6]$, the structure corresponding to

the ground-state magnetic moment of $\mu = 6\,\mu_B$ is tetragonal because of a Jahn–Teller distortion induced by the presence of high-spin manganese(III). The crystal structure of the $\mu = 8\,\mu_B$ phase is cubic, in excellent agreement with experiment. This indicated that the fully oxidized material is charge disproportionated into carbon-coordinated manganese(IV) and nitrogen-coordinated manganese(II). This is the first theoretical evidence for charge disproportionation in this particular composition. In $Na_3Mn[Mn(CN)_6]$, the sodium ions do not compete with each other for occupation of the interstice, of which there are only 2 per formula unit; rather, they occupy the face of the subcube, of which there are 6 per formula unit.

The compounds' PDOS are consistent with the atom-projected magnetic moments. They indicate that the compounds' oxidation states are $Mn^{II}[Mn^{IV}(CN)_6]$, $NaMn^{II}[Mn^{III}(CN)_6]$, $Na_2Mn^{II}[Mn^{II}(CN)_6]$, and finally $Na_3Mn^{II}[Mn^{I}(CN)_6]$. That is, all reduction events happen at the carbon-coordinated manganese atom. And the thermodynamic stability of the compound $Na_3Mn^{II}[Mn^{I}(CN)_6]$ is due in part to its particularly stable electronic configuration $t_{2g}^6 e_g^5$. This is the first modeling from first principles to support the identification of monovalent manganese in this compound.

The presence of crystalline water leads to lattice geometries that are in even better agreement with experimental data. Energetically, the grand potential for this system is derived. A phase diagram of oxidation states and degree of hydration in (water activity, voltage) space is constructed. Water has the effect of increasing the material's reduction potentials. Including water in the model puts the calculated voltage in much better agreement with experiment. Finally, an isoelectronic system, iron hexacyanochromate is examined. While this compound can theoretically also insert a third sodium ion, it is susceptible to isomerization into chromium hexacyanoferrate.

This theoretical work settles the questions of whether the insertion of a third sodium ion into a PBA lattice is even possible, and whether that is the likely origin of the high capacity in sodium manganese hexacyanomanganate. The answer to both

is yes.

Two interesting experiments are suggested immediately by this work. First, a sample of manganese hexacyanomanganate should be driven, carefully, to as close to the potential of sodium metal as possible, to see if a fourth ion will enter the structure. Second, the isoelectronic iron hexacyanochromate system should be prepared and studied to examine the importance of electronic structure and electronic configuration to the PBA high specific capacity.

One question that remains is why the experimentally observed specific capacity, 209 mA h g^{-1}, is lower than the theoretical value for the as-synthesized 229 mA h g^{-1}, a difference of 9%. The physio-chemical characterization of the as-synthesized material and the good agreement between theory and experiment seem to exclude the presence of hexacyanometallate vacancies as a justification for this discrepancy. A more plausible explanation is that the specific capacity is limited by the electrode's kinetics. Komaba and coworkers reported the beneficial effect of vacancies on potassium-ion conduction in potassium manganese hexacyanoferrate, highlighting the limited diffusivity in the vacancy-free material [16]. Future theoretical work can examine the activation energy for ion movement through the lattice using, for instance, the nudged elastic band method. This work provides a convincing explanation for the origin of the highest-ever observed reversible specific capacity in a PBA and is an important contribution to the theory of PBA electrodes.

Computational details

I performed all DFT calculations using the Vienna ab initio Simulation Package (VASP) [17, 18]. I used a Γ-centered $4 \times 4 \times 4$ **k**-point grid and a planewave kinetic-energy cutoff of 520 eV. The convergence criteria were 10^{-5} eV and 0.05 eV $Å^{-1}$ for electronic and ionic convergence, respectively. Full geometric relaxation was performed on all materials first within the generalized-gradient approximation using the

Perdew–Burke–Ernzerhof (PBE) functional [19] and then with the non-local, hybrid Heyd–Scuseria–Ernzerhof (HSE06) functional [20, 21]. For the HSE06 functional, I used the standard screening parameter of 0.2 $Å^{-1}$ and a mixing of 25% Fock exchange with 75% PBE exchange [21]. For the structures that contain water, water molecules were included explicitly in the model and full relaxation of the lattice vectors and atom positions (including water) were performed again using the HSE functional. The X-ray diffraction reflections were calculated using an incident photon wavelength of $\lambda = 0.413737$ Å in the "**V**isualization for **E**lectronic and **St**ructural **A**nalysis" (VESTA) [22, 23] and the diffractograms were plotted using the Lorentzian function with $\gamma = 0.01°$.

References

[1] H.-W. Lee, R. Y. Wang, M. Pasta, S. Woo Lee, N. Liu, and Y. Cui, "Manganese hexacyanomanganate open framework as a high-capacity positive electrode material for sodium-ion batteries," *Nature Communications*, vol. 5, pp. 1–6, 2014.

[2] A. Firouzi, R. Qiao, S. Motallebi, C. W. Valencia, H. S. Israel, M. Fujimoto, L. A. Wray, Y.-D. Chuang, W. Yang, and C. D. Wessells, "Monovalent manganese based anodes and co-solvent electrolyte for stable low-cost high-rate sodium-ion batteries," *Nature Communications*, vol. 9, no. 1, pp. 1–10, 2018.

[3] P. Xiao, J. Song, L. Wang, J. B. Goodenough, and G. Henkelman, "Theoretical study of the structural evolution of a $Na_2FeMn(CN)_6$ cathode upon Na intercalation," *Chemistry of Materials.*, vol. 27, no. 10, pp. 3763–3768, 2015.

[4] M. Mayo, K. J. Griffith, C. J. Pickard, and A. J. Morris, "Ab Initio Study of Phosphorus Anodes for Lithium- and Sodium-Ion Batteries," *Chemistry of Materials*, vol. 28, no. 7, pp. 2011–2021, 2016.

[5] R. A. Davidson and J. S. Miller, "Pressure Dependence of the Magnetic Ordering Temperature (T_C) for the $Na_2Mn[Mn(CN)_6]$ Noncubic Prussian Blue Analogue," *Inorganic Chemistry*, vol. 60, no. 17, pp. 12766–12771, 2021.

[6] G. L. Miessler, P. J. Fischer, and D. A. Tarr, *Inorganic Chemistry*. Pearson, 2014.

[7] S. Wheeler, I. Capone, S. Day, C. Tang, and M. Pasta, "Low-potential prussian blue analogues for sodium-ion batteries: manganese hexacyanochromate," *Chemistry of Materials*, vol. 31, no. 7, pp. 2619–2626, 2019.

[8] D. Parajuli, H. Tanaka, K. Sakurai, Y. Hakuta, and T. Kawamoto, "Thermal decomposition behavior of Prussian blue in various conditions," *Materials*, vol. 14, no. 5, pp. 1–17, 2021.

[9] R. Klenze, B. Kanellakopulos, G. Trageser, and H. H. Eysel, "Manganese hexacyanomanganate: Magnetic interactions via cyanide in a mixed valence Prussian blue type compound," *The Journal of Chemical Physics*, vol. 72, no. 11, pp. 5819–5828, 1980.

[10] G. W. Beall, W. O. Milligan, J. Korp, and I. Bernal, "Crystal structure of $Mn_3[Co(CN)_6]_2 \cdot 12H_2O$ and $Cd_3[Co(CN)_6]_2 \cdot 12H_2O$ by Neutron and X-Ray Diffraction," *Inorganic Chemistry*, vol. 16, no. 11, pp. 2715–2718, 1977.

[11] F. Herren, A. Ludi, P. Fischer, and W. Halg, "Neutron Diffraction Study of Prussian Blue, $Fe_4[Fe(CN)_6]_3 \cdot xH_2O$ Location of Water Molecules and Long-Range Magnetic Order," *Inorganic Chemistry*, vol. 19, no. 4, pp. 956–959, 1980.

[12] L. Wang, J. Song, R. Qiao, L. A. Wray, M. A. Hossain, Y. D. Chuang, W. Yang, Y. Lu, D. Evans, J. J. Lee, S. Vail, X. Zhao, M. Nishijima, S. Kakimoto, and J. B. Goodenough, "Rhombohedral Prussian white as cathode for rechargeable

sodium-ion batteries," *Journal of the American Chemical Society*, vol. 137, no. 7, pp. 2548–2554, 2015.

[13] J. Song, L. Wang, Y. Lu, J. Liu, B. Guo, P. Xiao, J. J. Lee, X. Q. Yang, G. Henkelman, and J. B. Goodenough, "Removal of interstitial H_2O in hexacyanometallates for a superior cathode of a sodium-ion battery," *Journal of the American Chemical Society*, vol. 137, no. 7, pp. 2658–2664, 2015.

[14] X. Guo, Z. Wang, Z. Deng, X. Li, B. Wang, X. Chen, and S. P. Ong, "Water contributes to higher energy density and cycling stability of prussian blue analogue cathodes for aqueous sodium-ion batteries," *Chemistry of Materials*, vol. 31, no. 15, pp. 5933–5942, 2019.

[15] A. Dostal, U. Schröder, and F. Scholz, "Electrochemistry of Chromium(II) Hexacyanochromate(III) and Electrochemically Induced Isomerization of Solid Iron(II) Hexacyanochromate(III) Mechanically Immobilized on the Surface of a Graphite Electrode," *Inorganic Chemistry*, vol. 34, no. 7, pp. 1711–1717, 1995.

[16] T. Hosaka, T. Fukabori, H. Kojima, K. Kubota, and S. Komaba, "Effect of Particle Size and Anion Vacancy on Electrochemical Potassium Ion Insertion into Potassium Manganese Hexacyanoferrates," *ChemSusChem*, vol. 14, no. 4, pp. 1166–1175, 2021.

[17] G. Kresse, J. Furthmüller, and J. Hafner, "Theory of the crystal structures of selenium and tellurium: The effect of generalized-gradient corrections to the local-density approximation," *Physical Review B*, vol. 50, no. 18, pp. 13181–13185, 1994.

[18] G. Kresse and J. Furthmüller, "Efficiency of ab-initio total energy calculations for metals and semiconductors using a plane-wave basis set," *Computational Materials Science*, vol. 6, no. 1, pp. 15–50, 1996.

[19] J. P. Perdew, K. Burke, and M. Ernzerhof, "Generalized Gradient Approximation Made Simple," *Physical Review Letters*, vol. 77, no. 18, pp. 3865–3868, 1996.

[20] J. Heyd, G. E. Scuseria, and M. Ernzerhof, "Hybrid functionals based on a screened Coulomb potential," *Journal of Chemical Physics*, vol. 118, no. 18, pp. 8207–8215, 2003.

[21] A. V. Krukau, O. A. Vydrov, A. F. Izmaylov, and G. E. Scuseria, "Influence of the exchange screening parameter on the performance of screened hybrid functionals," *The Journal of chemical physics*, vol. 125, no. 22, p. 224106, 2006.

[22] K. Momma and F. Izumi, "VESTA: A three-dimensional visualization system for electronic and structural analysis," *Journal of Applied Crystallography*, vol. 41, no. 3, pp. 653–658, 2008.

[23] K. Momma and F. Izumi, "VESTA 3 for three-dimensional visualization of crystal, volumetric and morphology data," *Journal of Applied Crystallography*, vol. 44, no. 6, pp. 1272–1276, 2011.

Chapter 5

Properties of vacancy-free chromium hexacyanochromate

Abstract

Chromium hexacyanochromate, $A_x\mathrm{Cr}[\mathrm{Cr}(\mathrm{CN})_6]$, is a Prussian blue analog that has significant promise as an anode in next-generation batteries and as a magnetic material with a high ordering temperature. Both uses require minimal vacancies. However, synthesis of a defect-free sample continues to elude experimentalists. In this work, the materials properties of four alkali-metal chromium hexacyanochromates are predicted from first principles. The DFT+U formalism is used. The two chromium ions in unique crystal fields are parameterized with different U values, but these are constant among the three oxidation states examined. The reduction potentials of the compounds increase with inserting-ion radius from -1.6 to -0.6 V versus the SHE. The ion-hopping activation energies range from 0.14 eV for sodium to 1.83 eV for cesium. The compound $\mathrm{Cr}[\mathrm{Cr}(\mathrm{CN})_6]$ is confirmed to be antiferromagnetic with $J_1 = -22$ meV, and $A_2\mathrm{Cr}^{\mathrm{III}}[\mathrm{Cr}^{\mathrm{I}}(\mathrm{CN})_6]$ is predicted to be charge disproportionated. Finally, a vacancy itself is simulated and the deep-level traps that result in the electronic structure are studied. This work is the first thorough, computational, and electrochemical investigation into this PBA system. It presents testable predictions for ongoing experimental efforts to synthesize the defect-free phase of this promising

material.

5.1 An anode and a magnet

Chromium hexacyanochromate, $A_x\mathrm{Cr}[\mathrm{Cr}(\mathrm{CN})_6]$, is a promising anode for the next generation of batteries. The carbon-coordinated chromium has a low reduction potential of about -0.6 to -0.8 V versus the standard hydrogen electrode for the insertion of sodium [1–3] and potassium [3, 4]. The system is also an important platform for studying magnetism in materials [5–7]. The compound $\mathrm{Cr}[\mathrm{Cr}(\mathrm{CN})_6]$ is an antiferromagnet; that is, the magnetic moment on each carbon-coordinated chromium ion is anti-aligned with the moments on the six nearest-neighbor nitrogen-coordinated chromium ions. Certain stoichiometries have demonstrated an ordering temperature as high as 270 K [8].

The usefulness of this system as an anode or as a magnet depends on preparing material with as few vacancies as possible. In PBA batteries, vacancies decrease the specific capacity. In PBA magnets, vacancies decrease the number of anti-aligned spin centers, lowering the ordering temperature.

While there have been experimental claims of the preparation of chromium hexacyanochromate without defects [9], the data are ambiguous. Specific capacities are below the theoretical value of about 170 mA h g^{-1}, and saturation magnetizations are nonzero. Both are very possibly due to non-stoichiometry of the hexacyanochromate. This chapter is motivated, in part, by the need for theoretical prediction of some properties of this system for comparison to previous reports and ongoing experimental efforts.

In this chapter, I use DFT+U to predict the materials properties for defect-free alkali-metal chromium hexacyanochromates, shown schematically in Figure 5.1. The need for supercells, containing up to 112 atoms and over 500 bands, to calculate

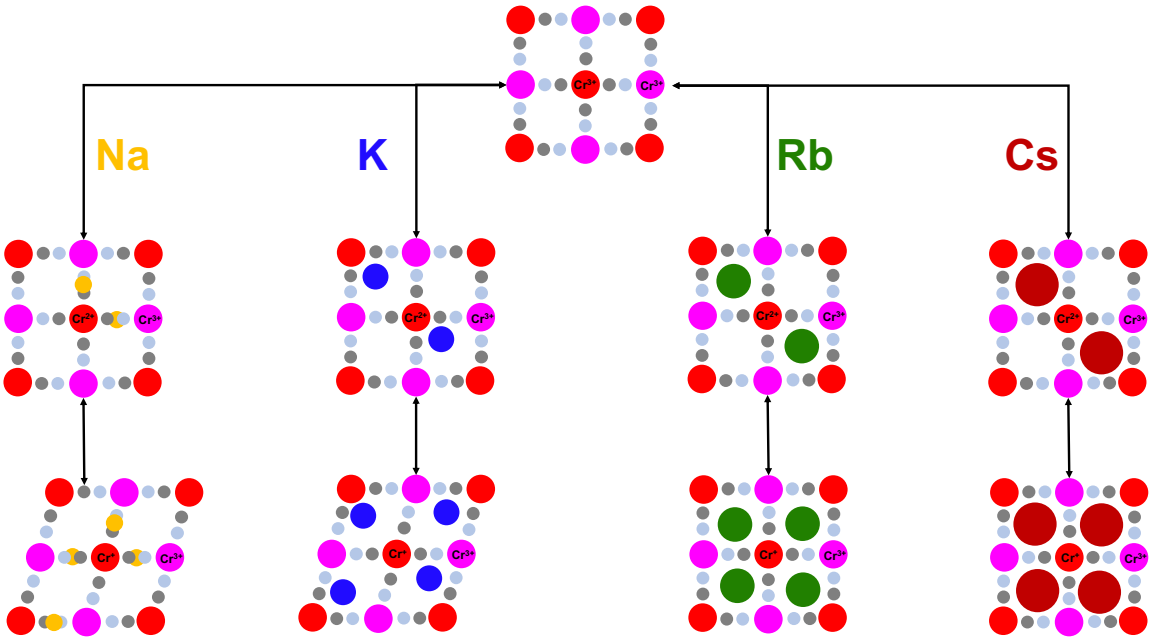

Figure 5.1: Schematic of alkali-metal chromium hexacyanochromates. Carbon-coordinated chromium, nitrogen-coordinated chromium, carbon, and nitrogen atoms are shown in red, pink, gray, and light blue, respectively. Sodium, potassium, rubidium, and cesium atoms are shown in gold, blue, green, and dark red, respectively. At the top is the fully oxidized phase. The middle row is the intermediate oxidation state containing one alkali-metal ion and mixed-valent (Cr(II), Cr(III)). The bottom row is the fully reduced phase with two alkali-metal ions per formula unit and charge-disproportionated (Cr(I), Cr(III)). Note that the sodium ions are not in the cyanide bond; they are out of the plane of the cyanide bond in the center of the subcube face.

properties like vacancies, activation energy for ion hopping, and magnetic exchange-coupling coefficients makes DFT+U preferable to hybrid functionals. Multiple inserting elements are investigated because various alkali-metal PBAs are of scientific and technological importance per se [10] and because synthetic efforts in our laboratory at this time involve different alkali metals. This is also why the study is confined to the dehydrated phases - instability of the precursors in water precludes aqueous syntheses.

First I parameterize the Hubbard U values for the carbon- and nitrogen-coordinated chromium ions, ($U_{\mathrm{Cr_C}}$, $U_{\mathrm{Cr_N}}$), by comparing the unit-cell volumes and reduction potentials to the values predicted by the HSE functional for $\mathrm{K}_x\mathrm{Cr[Cr(CN)_6]}$. I then

proceed to contrast the physiochemical and electrochemical properties of four alkali-metal chromium hexacyanochromates (sodium, potassium, rubidium, and cesium), calculating their volumes, reduction potentials, and activation energies for ion hopping. I then proceed to compare the compounds' electronic and magnetic properties like atomic charges and magnetic moments, infrared (IR)-spectroscopy absorption frequencies, and the direct magnetic exchange-coupling coefficient, J_1. Finally, I simulate a vacancy itself and analyze its crystal and electronic structures.

This work includes the first prediction of chromium hexacyanochromate's reduction potential for the insertion of the second alkali-metal ion; activation energy for ion-hopping; IR absorption frequencies as a function of oxidation state; and the crystal and electronic structures of a vacancy. These results are important complementary evidence in support of ongoing experimental attempts to synthesize and confirm defect-free chromium hexacyanochromate. This is critical new insight into this technologically promising and scientifically intriguing system.

5.2 Parameterization of the Hubbard U values

In this section, the Hubbard U values for the two chromium ions, $U_{\mathrm{Cr_C}}$ and $U_{\mathrm{Cr_N}}$ are parameterized within the model system potassium chromium hexacyanochromate. The U value for an ion is dependent on its crystal environment and is not generally portable between DFT implementations [11]. Potassium is chosen because of the technological relevance of potassium-ion batteries and because it has been a common and convenient inserting ion for experimental studies of this system. Two properties, unit-cell volume and reduction potential versus potassium metal, are calculated with the HSE functional and by DFT+U for 121 values of ($U_{\mathrm{Cr_C}}$, $U_{\mathrm{Cr_N}}$) for a single formula unit. The results are used to identity the ($U_{\mathrm{Cr_C}}$, $U_{\mathrm{Cr_N}}$) that best matches the HSE-calculated values.

5.2.1 HSE-level prediction for the potassium analog

The compound $Cr[Cr(CN)_6]$ is cubic with a unit-cell volume of 282 Å^3. The atom-projected magnetic moment on the carbon-coordinated chromium ion is -2.845 μ_B and the moment on the nitrogen-coordinated chromium is 2.842 μ_B. This is consistent with an oxidation state of (Cr_C(III), Cr_N(III)) with anti-ferromagnetic ordering between the two chromium ions. The compound $KCr[Cr(CN)_6]$ has a unit-cell volume of 278 Å^3. The magnetic moments are -1.825 and 2.822 μ_B for the carbon- and nitrogen-coordinated chromium ions, respectively. This indicates the first reduction event occurs at the carbon-coordinated chromium and the oxidation state is (Cr_C(II), Cr_N(III)) with ferrimagnetic alignment. The reduction potential for the reaction $Cr[Cr(CN)_6] + K \rightarrow KCr[Cr(CN)_6]$ is 1.875 V versus K^+/K (that is, versus potassium metal). Finally, the compound $K_2Cr[Cr(CN)_6]$ has a unit-cell volume of 271 Å^3. The atom-projected magnetic moments of -0.716 and 2.766 μ_B for the carbon- and nitrogen-coordinated chromium ions, respectively. This suggests that the second reduction event also occurs at the carbon-coordinated chromium ion, and the oxidation states for this phase are (Cr_C(I), Cr_N(III)). That is, the fully reduced phase is expected to be charge disproportionated. It is also ferrimagnetic. The reduction potential for $KCr[Cr(CN)_6] + K \rightarrow K_2Cr[Cr(CN)_6]$ is 1.602 V versus K^+/K.

5.2.2 Parameterizing based on volume

The volumes of the unit cells for the three compounds to DFT+U are plotted in Figure 5.2 versus the two U parameters, (U_{Cr_C}, U_{Cr_N}). Both U values cover the closed region $[0, 5]$ eV with a discretization of 0.5 eV, giving a total of 121 query points in the search space. The values plotted are the fractional difference between the DFT+U-calculated volume, V_{DFT+U}, and the HSE-computed value, V_{HSE}, as

$$v = \frac{V_{DFT+U} - V_{HSE}}{V_{HSE}}. \tag{5.1}$$

For $Cr[Cr(CN)_6]$, the volume depends only on the value of the sum of the U values, as $U_{Cr_C} + U_{Cr_N}$. The line $U_{Cr_C} + U_{Cr_N} = 2.5$ eV matches the HSE-calculated volume most closely. For $U_{Cr_C} + U_{Cr_N} < 2.5$ eV, the DFT+U-calculated result underestimates the HSE-calculated value, while for $U_{Cr_C} + U_{Cr_N} > 2.5$ eV it overestimates it. For the compound $KCr[Cr(CN)_6]$, the dependence on U is slightly more complicated. This compound still has the best agreement with HSE along the line of constant $U_{Cr_C} + U_{Cr_N} = 2.5$ eV. A second effect is overlaid, though. For $U_{Cr_C} - U_{Cr_N} > 2.0$ eV in the region $U_{Cr_C} = [3.0, 5.0]$ eV, DFT+U more severely overestimates the volume. This is caused by a change in the calculated oxidation state. Inside this region, the DFT+U-calculated oxidation state is (Cr_C(III), Cr_N(II)) (as opposed to Cr_C(II), Cr_N(III) as calculated outside the region and by the HSE functional). This oxidation state leads to a larger lattice parameter and volume. In the compound $K_2Cr[Cr(CN)_6]$, the effect of U is similar to the effect in $KCr[Cr(CN)_6]$. The best agreement with HSE occurs along a line of constant $U_{Cr_C} + U_{Cr_N}$. Here the line is shifted somewhat toward the origin, to between $U_{Cr_C} + U_{Cr_N} = 1.0$ and $U_{Cr_C} + U_{Cr_N} = 2.0$ eV. However, the volume change changes less rapidly with U in this compound. That is, the agreement between DFT+U and HSE falls off slower with $U_{Cr_C} + U_{Cr_N}$ in this compound. The compound also has a secondary region similar to $KCr[Cr(CN)_6]$, but it is shifted to the region $U_{Cr_C} - U_{Cr_N} > 4.0$ eV for $U_{Cr_C} = [4.0, 5.0]$ eV. This region also corresponds to different oxidation states. Both (Cr_C(II), Cr_N(II)) and even (Cr_C(III), Cr_N(I)) are observed here.

5.2.3 Parameterizing based on reduction potential

The reduction potentials for the electrochemical reaction for the compounds with potassium are plotted in Figure 5.3. The U space is the same and the value plotted is

$$\epsilon = \frac{E_{\mathrm{DFT+U}} - E_{\mathrm{HSE}}}{E_{\mathrm{HSE}}}. \tag{5.2}$$

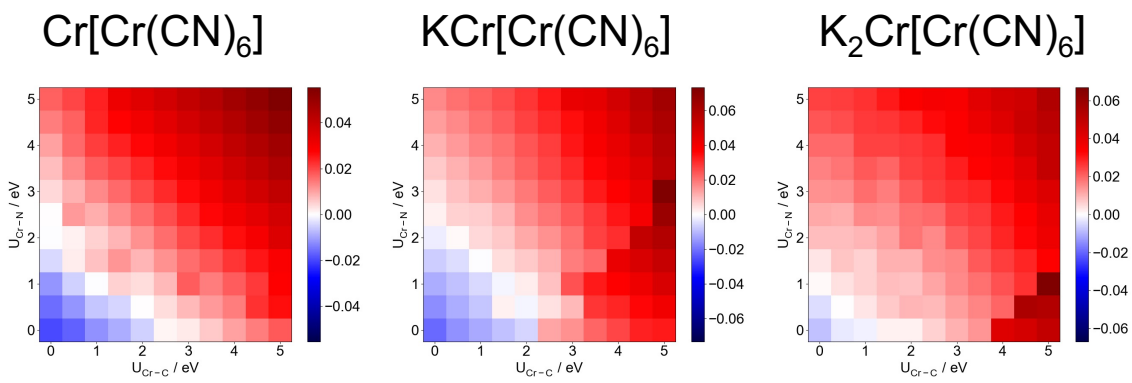

Figure 5.2: Unit-cell volumes of $K_xCr[Cr(CN)_6]$ as a function of Hubbard U. The values plotted represent a fractional difference from the volumes calculated using the HSE functional.

Note that there are only two subplots in Figure 5.3 because the reduction potential depends on the energies of pairs of compounds. For the reaction $Cr[Cr(CN)_6] \rightarrow KCr[Cr(CN)_6]$, the best agreement between DFT+U and HSE occurs along the line $U_{\mathrm{Cr_C}} = 2.0$ eV. For $U_{\mathrm{Cr_C}} < 2.0$ eV, DFT+U overestimates the reduction potential and underestimates it for $U_{\mathrm{Cr_C}} > 2.0$ eV. Also, the region ($U_{\mathrm{Cr_C}} - U_{\mathrm{Cr_N}} > 2.0$ eV for $U_{\mathrm{Cr_C}} = [3.0, 5.0]$ eV) of increased volume in $KCr[Cr(CN)_6]$ also has a lower reduction potential. For the reaction $KCr[Cr(CN)_6] \rightarrow K_2Cr[Cr(CN)_6]$, the best agreement between DFT+U and HSE occurs near the lines $U_{\mathrm{Cr_C}} = 1.0$ eV and $U_{\mathrm{Cr_C}} = 1.5$ eV. The region with the elevated volume for $K_2Cr[Cr(CN)_6]$ in Figure 5.2 has lower reduction potentials here.

The rest of the calculations in this chapter use DFT+U with values ($U_{\mathrm{Cr_C}} = 2.0$, $U_{\mathrm{Cr_N}} = 0.5$) eV as an optimal parameterization based on comparison with the HSE-level results. While those values are specific to the implementation used to calculate them, they show that this system does require unique U values for the same element because they are in different crystal environments. However, the U values are independent of oxidation state (for at least the three oxidation states studied here), making it possible to model different oxidation states and thus calculate reduction potentials.

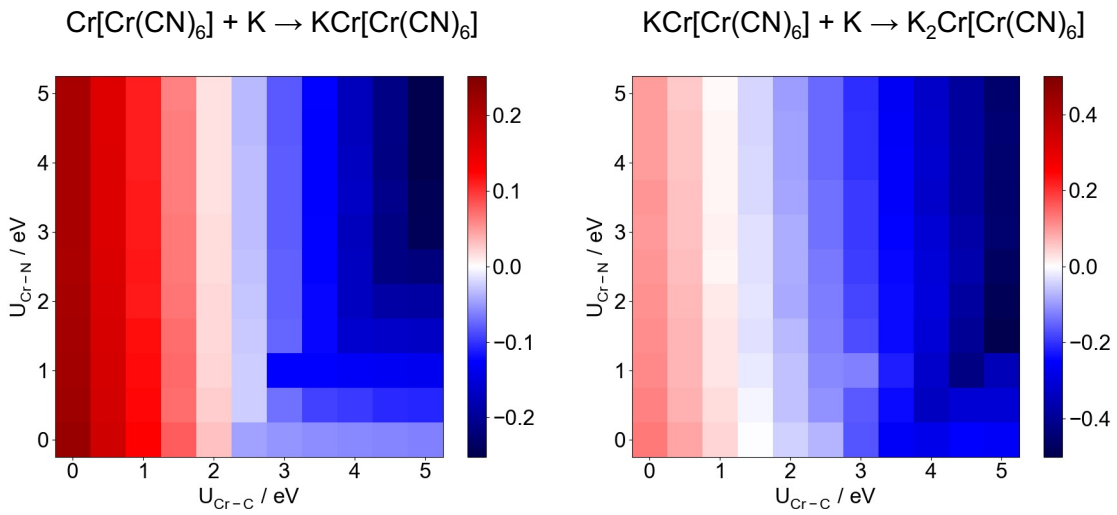

Figure 5.3: Reduction potentials of $K_xCr[Cr(CN)_6]$ as a function of Hubbard U. The values plotted represent a fractional difference from the reduction potentials calculated using the HSE functional.

5.3 Physio- and electrochemical properties

This section deals with the physiochemical and electrochemical properties of three oxidation states of four alkali-metal chromium hexacyanochromates: sodium, potassium, rubidium, and cesium; that is $A_xCr[Cr(CN)_6]$ for $A \in \{\text{Na, K, Rb, Cs}\}$ and $x \in \{0, 1, 2\}$. Since the $x = 0$ phase is free of any inserting ion, a total of 9 compounds are considered. The effects of the inserting ions on the crystal structure, volume, reduction potential, and activation energy are compared and contrasted.

5.3.1 Volume and crystal structure

The volumes of the compounds are plotted in Figure 5.4 versus number of inserting ions per formula unit. The empty lattice has a volume of 282 Å^3. The volumes of the sodiated compounds then decrease to 278 and 274 Å^3 for the $x = 1$ and $x = 2$ phases, respectively. The potassiated compounds contract to 278 and then 274 Å^3, while the rubidiated compounds go to 278 and then 273 Å^3. Finally, the cesiated decrease in volume to 279 and then to 276 Å^3. First, the magnitude of the volume charge should

be noted; it is less than a 3% change in the volume for all materials on reduction, or a change of less than 1% change to the lattice parameter. This is in good agreement with the general trend in the PBAs that they have very small volume changes as they are oxidized or reduced [12]. Second, the volume *decreases* as more inserting ions are added, regardless of the element being inserted. This is perhaps counterintuitive, and, indeed, many important electrode materials like NMC expand as they are lithiated [13, 14]. In the PBAs, though, contraction on reduction is a well-documented phenomenon [15]. The cause is the added electron density in the hexacyanometallate complex. In this case, the extra electrons in the hexacyanochromate add electron density to the Cr–C bond. Finally, the differences between the volume for the sodium, potassium, and rubidium analogs are negligible. However, the compounds $CsCr[Cr(CN)_6]$ and $Cs_2Cr[Cr(CN)_6]$ have significantly higher volumes. Cesiating the lattice still causes it to contract, but the cesium has such a large ionic radius that the lattice cannot contract as much due to steric hindrance.

5.3.2 Reduction potentials

To compare the reduction potentials of the various alkali-metal chromium hexacyanochromates, it is useful to reference them to the same standard potential. The standard hydrogen electrode (SHE) is convenient for this purpose. This standard is based on the half-reaction

$$2H^+(aq) + 2e^- \rightarrow H_2(g). \tag{5.3}$$

The alkali metals sodium, potassium, rubidium, and cesium have reduction potentials (for the half-reaction $A^+ + e^- \rightarrow A(s)$) of -2.71, -2.93, -2.98, and -2.92 V versus the SHE, respectively. If V_A is the voltage of the alkali-metal chromium hexacyanochromate versus the alkali metal (as calculated from DFT) and $E^0_{r,A}$ is the reduction potential of the alkali metal versus the SHE (taken from reference [16]), then the po-

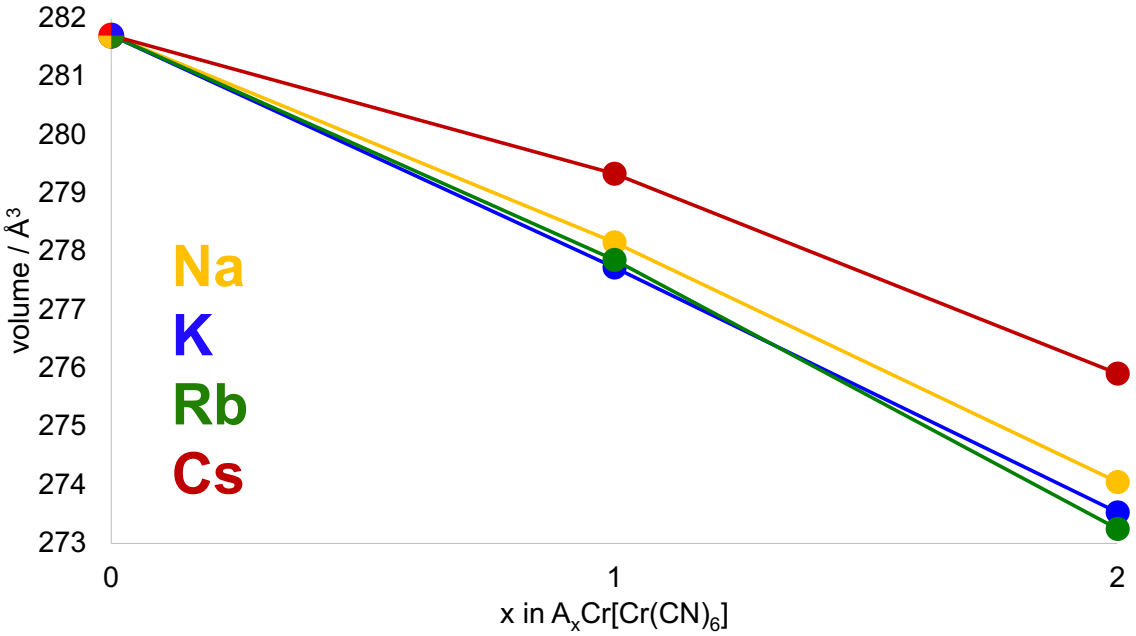

Figure 5.4: Unit-cell volumes as a function of oxidation state. The volumes of the 9 compounds are plotted against number of alkali-metal ions per formula unit. Data for the sodium, potassium, rubidium, and cesium analogs are plotted in gold, blue, green, and dark red, respectively.

tential of the alkali-metal chromium hexacyanochromate versus the SHE is $V_A + E^0_{\mathrm{r},A}$. These potentials, versus the SHE, are plotted in Figure 5.5.

The two reactions for $\mathrm{Na}_x\mathrm{Cr}[\mathrm{Cr}(\mathrm{CN})_6] + \mathrm{Na(s)} \rightarrow \mathrm{Na}_{x+1}\mathrm{Cr}[\mathrm{Cr}(\mathrm{CN})_6]$ have potentials of -1.31 and -1.60 V. The potassium compounds reduce at -1.01 and -1.17 V, and the rubidium compounds react at -0.89 and -1.06 V. Finally, insertion of cesium becomes favorable at -0.60 and -0.81 V. These potentials, ranging 1 V from -1.60 up to -0.60 V versus the SHE, are relatively low, and this comports with the interest in this system for application as an anode. Furthermore, the trend that both voltage plateaus increase with the ionic radius of the inserting ion is consistent with experimental and theoretical studies on other PBA compositions [17, 18]. Also, two voltage plateaus exist for all four analogs. That is, insertion of two ions is thermodynamically spontaneous. Finally, I reemphasize that this model does not include water. As seen in Chapter 4, crystalline water can increase the reduction potential

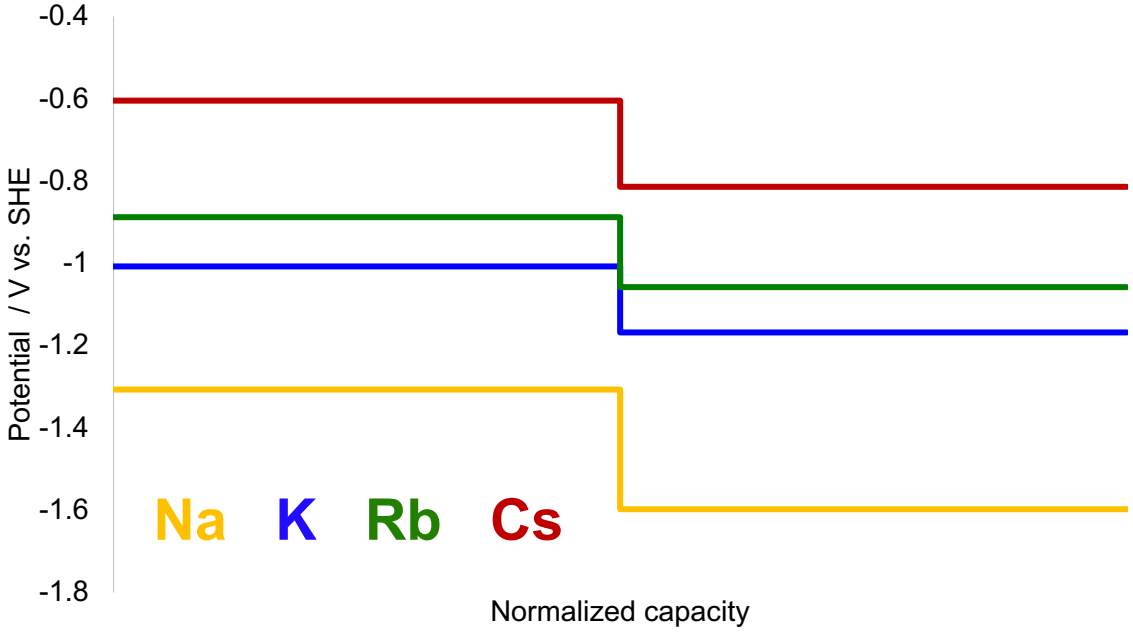

Figure 5.5: Simulated galvanostatic curves for $A_x\mathrm{Cr}[\mathrm{Cr}(\mathrm{CN})_6]$. The reduction potential for sodium (gold), potassium (blue), rubidium (green), and cesium (dark red) chromium hexacyanoferrates are plotted versus normalized capacity in simulated galvanostatic curves.

by several hundred millivolts. So it would be valuable for future work to explore the role of water in this system.

5.3.3 Activation energy for ion movement

Kinetically, the compounds' electrochemistry is strongly influenced by the diffusivity and ionic conductivity of the alkali-metal ions through the lattice. The activation energy for these processes is the maximum along the minimum-energy path (MEP) between two stationary points on the potential-energy surface [19]. The energy as a function of position is shown in Figure 5.6. The activation energies for sodium, potassium, rubidium, and cesium in chromium hexacyanochromate are 0.14, 0.52, 1.04, and 1.83 eV, respectively. For comparison, Van der Ven and coworkers [20] calculated the activation energy for lithium movement through various olivines and found values that ranged from 0.11 to 0.36 eV in $\mathrm{Li}_x\mathrm{CoPO}_4$. The prediction of a low activation energy for sodium is unsurprising given the exceedingly high rate capabilities in PBA

sodium-ion cathodes [21]. The ionic conductivity in the chromium hexacyanochromate system has never been experimentally characterized, but the model suggests that it, too, is quite high. The prediction of the jump up to 0.52 eV for potassium would also agree with the current understanding of potassium kinetics; a combination of poor ionic and electronic transport has been suggested as the cause of lower-than-expected capacities in some potassium-ion electrodes [22]. Finally, ion transport becomes very difficult and all-but-impossible for rubidium and cesium, respectively, in the defect-free lattice.

The MEPs for the ions are also shown in Figure 5.6. The path for cesium is straightforward; the ion begins in the center of the subcube, moves through the center of the interfacial square, and proceeds to the center of the next subcube. Rubidium is similar, but its starting and ending equilibrium positions are slightly off the exact center of the subcube toward a corner. Potassium continues the trend, with its starting and ending positions even closer to the corner (compared to rubidium). The MEP for sodium is quite different. Its equilibrium position is the center of the subcube face, and its path "bounces" to the center of the edge-sharing face (a local minimum), then bouncing again to the center of the face opposite the starting face. It avoids the center of the subcube entirely.

The motion also has a polaronic character, which is best illustrated by the potassium analog. The potassium ion is displaced to a position only 3.80 Å away from a corner of the subcube occupied by a carbon-coordinated chromium. (The subcube center is 5.00 Å away from the corners.) And the atomic magnetic moments indicate that the electron added by the inserting potassium ion is highly localized on the same carbon-coordinated ion, making it chromium(II). Its magnetic moment is $-1.66\ \mu_{\mathrm{B}}$, while all other carbon-coordinated chromium atom's maintain magnetic moments between -2.73 and $-2.74\ \mu_{\mathrm{B}}$, the value in the fully depotassiated compound. At the same time, the six $\mathrm{Cr}^{\mathrm{II}}_{\mathrm{C}} - \mathrm{C}$ bonds contract by about 1% compared

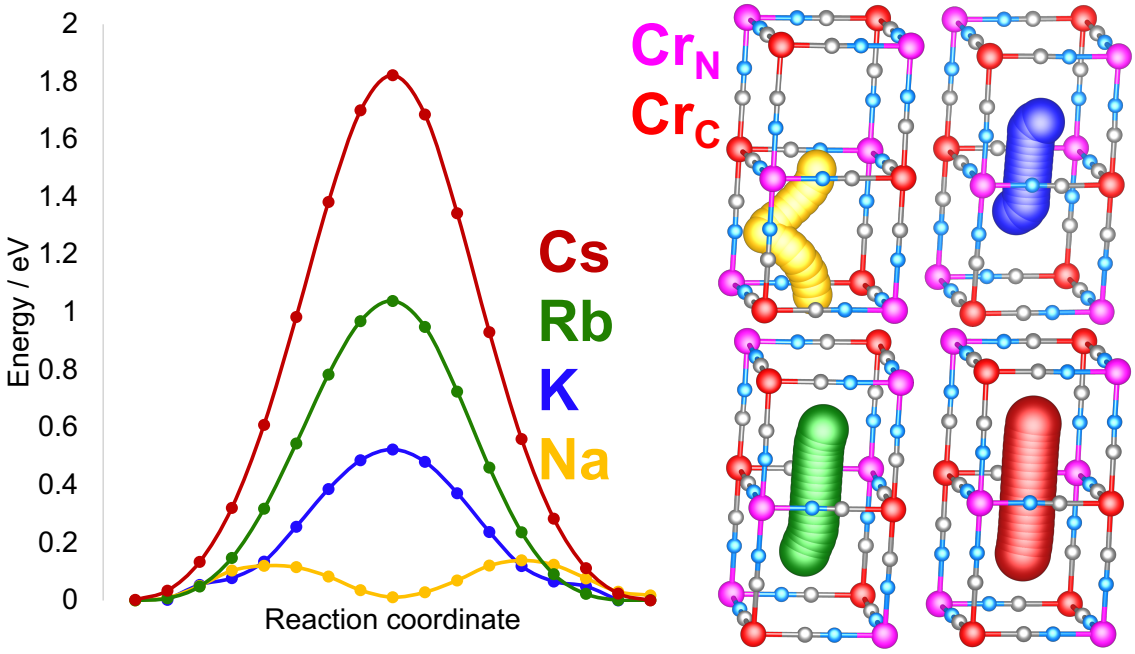

Figure 5.6: Activation energies and paths for ion movement. At the left, the energy versus reaction coordinate is plotted for the movement of sodium (gold), potassium (blue), rubidium (green), and cesium (darker red) ions through the chromium hexacyanoferrate lattice. At the right, the minimum-energy path is shown. Lighter-red ions are carbon-coordinated chromium and pink ions are nitrogen-coordinated chromium.

Table 5.1: Properties of the small polaron. This table lists certain properties of the 8 chromium ions that form the subcube containing the potassium ion in a 2 × 2 × 2 supercell simulation. The atomic magnetic moment (μ), distance from each chromium ion to the potassium ion (M–K), and distance from the chromium ion to the cyanide ligand (either carbon or nitrogen, M–L). The small polaron is localized at $\mathrm{Cr_{C,1}}$, highlighted in red.

M	$\mu_\mathrm{M}/\mu_\mathrm{B}$	M-K / Å	M-L / Å
$\mathrm{Cr_{C,1}}$	−1.66	3.80	2.02
$\mathrm{Cr_{C,2}}$	−2.73	4.50	2.05
$\mathrm{Cr_{C,3}}$	−2.74	4.98	2.05
$\mathrm{Cr_{C,4}}$	−2.74	5.00	2.05
$\mathrm{Cr_{N,1}}$	+2.67	5.30	1.99
$\mathrm{Cr_{N,2}}$	+2.65	4.63	1.99
$\mathrm{Cr_{N,3}}$	+2.65	4.14	2.00
$\mathrm{Cr_{N,4}}$	+2.64	4.18	2.00

to the other $\mathrm{Cr^{III}_C} - \mathrm{C}$ bonds. This localized electron and lattice distortion is a small polaron, and its properties are summarized in Table 5.1. And it has to hop with the potassium ion. In the transition state, the extra charge density is shared by the two carbon-coordinated chromium ions in the square face (for atomic magnetic moments of −2.34 and −2.35 μ_B). After the potassium moves through the face, the polaron reforms in the adjacent subcube.

This section has examined the physiochemical and electrochemical properties of chromium hexacyanochromate as a function of inserting ion and oxidation state. Several important trends are predicted that have been observed in other PBA compositions. These include decrease of the unit-cell volume as the number of insertion ions increases, but small volume changes overall and increase of both reduction potential and activation-energy for ion hopping with ionic radius of the inserting ion.

5.4 Magnetic and electronic properties

This section explores magnetic and electronic properties. It begins by discussing the charge and magnetic moment attributed to each chromium ion in the compounds.

Next, the magnetic exchange-coupling coefficient is introduced and calculated for the fully oxidized compound $Cr[Cr(CN)_6]$. The simulated IR spectra are then plotted and their salient features are discussed.

5.4.1 Lattice ions' atomic charges and magnetic moments

The charge and magnetic moment arising from the each chromium ion as a function of oxidation state are plotted in Figure 5.7. Of note is how similar the charge and magnetic-moments plots are for all the compounds. This is a consequence of the highly ionic nature of PBAs; when the lattice is reduced by any alkali-metal, an electron is donated completely from the reducing atom to the crystal lattice, where the electron becomes highly localized on one of the ions (see also Chapter 3). So, the electronic structure is not strongly a function of the element inserted, in contrast to the physiochemistry and electrochemistry discussed above.

Note that, in the following discussion, the charge added to the lattice ion on reduction is less than 1 because the Wigner-Seitz radius for the chromium ions excludes some charge density. There is no unambiguous choice of Wigner-Seitz radii for a multi-element simulation, and the projection of the density matrix will necessarily exclude or double-count some volume. As will be seen, though the charge added on reduction is less than 1, it is constant for the two reduction events. These same considerations hold for the magnetization and spin density.

The two chromium atoms have approximately equal charge in the fully oxidized state, consistent with the oxidation state $Cr^{III}[Cr^{III}(CN)_6]$. On reduction to the $A_1Cr[Cr(CN)_6]$ phase, the number of electrons on the carbon-coordinated chromium ion increases by an average value of 0.275 e^-, while the change in the charge on the nitrogen-coordinated chromium is negligible. The oxidation state for these four compounds is the mixed-valent $A_1Cr^{III}[Cr^{II}(CN)_6]$. Reduction to $A_2Cr[Cr(CN)_6]$ sees the charge on the carbon-coordinated chromium increase again and by the same amount,

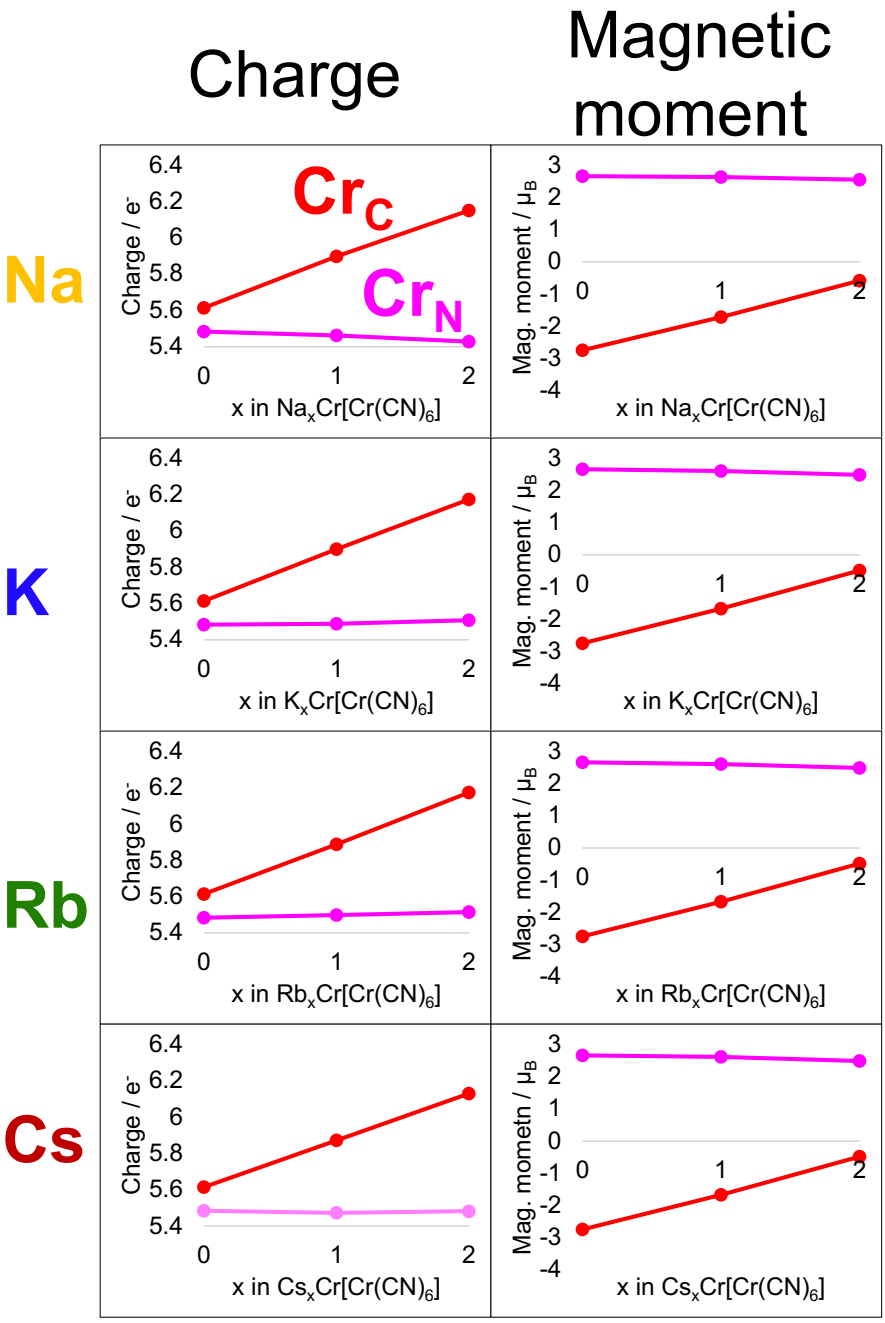

Figure 5.7: Charges and magnetic moments. The charges and magnetic moments localized on the chromium ions are plotted versus number of inserted alkali ions for $A_x\mathrm{Cr}[\mathrm{Cr}(\mathrm{CN})_6]$. Sodium, potassium, rubidium, and cesium chromium hexacyanochromates are plotted from top to bottom. The charges, in units of the fundamental charge, are shown on the left and the magnetic moments, in units of the Bohr magneton, are shown on the right. The red data points are for the carbon-coordinated chromium and the pink lines are for the nitrogen-coordinated chromium.

0.268 e^-. Again, the charge on the nitrogen-coordinated ion is nearly constant. This indicates that the compounds' oxidation state is the charge-disproportionated $A_2Cr^{III}[Cr^{I}(CN)_6]$.

The ions' magnetic moments agree with these oxidation-state assignments and give further information about orbital occupations and spin configurations. In the fully oxidized state $Cr^{III}[Cr^{III}(CN)_6]$, the chromium ions have magnetic moments of about +3 and −3. This is consistent with an electronic configuration of anti-aligned ($Cr_C(t_{2g}^3)$, $Cr_N(t_{2g}^3)$). Importantly, the total magnetic moment for the cell is 0, so the model predicts a zero remnant magnetization in the material. In $A_1Cr^{III}[Cr^{II}(CN)_6]$, the magnetic moment on the carbon-coordinated chromium increases by 1.06 μ_B while the nitrogen-coordinated chromium's magnetic moment does not change. This means that the added electron occupies a spin-up t_{2g} orbital on the carbon-coordinated chromium, as anti-aligned ($Cr_C(t_{2g}^4)$, $Cr_N(t_{2g}^3)$). Addition of the second electron to give $A_2Cr^{III}[Cr^{I}(CN)_6]$ again increases the magnetic moment of the nitrogen-coordinated ion by 1.17 μ_B. The magnetic moment of the nitrogen-coordinated ion does not change. So the electronic configuration is anti-aligned ($Cr_C(t_{2g}^5)$, $Cr_N(t_{2g}^3)$).

5.4.2 Magnetic direct exchange-coupling coefficient, J_1

The energetic interaction between the magnetic centers in a material is characterized by the Heisenberg Hamiltonian [23]

$$\hat{H} = -\sum_{\langle ij \rangle} J_{ij} \mathbf{e}_i \cdot \mathbf{e}_j \tag{5.4}$$

in which the J_{ij} are the magnetic exchange-coupling coefficients (to be determined), $\mathbf{e_i}$ are the direction vectors for the spin at the i^{th} magnetic center, and the sum is taken over all pairs of centers, ij, once. (If pairs are double counted, a factor of one-half should be included.) This is a kind of cluster expansion over the magnetic ordering [24]. Here, I consider only nearest-neighbor effects because the second-nearest-neighbor lattice ion in a PBA is almost 7.5 Å distant and the orbital overlap

that determines J_{ij} falls off exponentially with distance. The Heisenberg Hamiltonian then reduces to

$$\hat{H} = -J_1 \sum_{\langle ij \rangle} \mathbf{e}_i \cdot \mathbf{e}_j \tag{5.5}$$

in which the sum now runs only over nearest neighbors. This J_1 is called the direct (magnetic) exchange-coupling coefficient.

Taking the total DFT energy of the ground-state, antiferromagnetic ordering of $Cr[Cr(CN)_6]$ and the energy of the excited state with the spin of exactly one chromium atom (in a $2 \times 2 \times 2$ supercell) inverted gives two relations from 5.5,

$$E_{\mathrm{AFM}} = E_0 + 6J_1 \tag{5.6}$$

and

$$E_{\mathrm{FM}} = E_0 - 6J_1. \tag{5.7}$$

Subtracting these gives

$$\Delta E = E_{\mathrm{AFM}} - E_{\mathrm{FM}} = 12J_1. \tag{5.8}$$

From this, the direct magnetic exchange-coupling coefficient is $J_1 = -22$ meV in $Cr[Cr(CN)_6]$. That the compound is antiferromagnetic is apparent from the fact that $J_1 < 0$. For context, NiO is a high-temperature antiferromagnet and its coupling coefficient has been measured experimentally to be -19 meV [25]. (Note that next-nearest-neighbor interactions dominate in this material, so $J_2 = -19$ meV.) For NiO, Kotani and van Schilfgaarde calculated a value of -28.3 meV within the LDA and -14.7 meV with the more-advanced quasiparticle self-consistent GW (QSGW) method [26]. Connecting the magnetic exchange-coupling coefficients to properties like magnetic susceptibility or ordering temperature requires the use of some other theory of statistical mechanics—like mean-field methods or Monte Carlo simulation—that is beyond the scope of this work. But this work provides the seed parameter for those other theoretical strategies.

(Note that the Hamiltonian in 5.4 is sometimes defined in terms of the spin vector, $\mathbf{S}$, rather than the unit vector aligned with the spin. That is, $\hat{H} = -\sum_{\langle ij \rangle} J_{ij} \mathbf{S}_i \cdot \mathbf{S}_j$. Using that definition and a total electron spin of $\frac{3}{2}$ on Cr(III), $J_1 = -9.7$ meV.)

5.4.3 Simulating the IR spectra

The infrared (IR) spectrum of a PBA is an important tool in characterizing the bonding environment and oxidation state of the lattice ions. Simulating the IR spectrum for a material from first principles relies on density-functional perturbation theory [27, 28] to probe the responsiveness of the normal modes to a perturbative force. By calculating the matrix of second derivatives, known as the Hessian matrix, the frequencies can also be calculated.

The simulated IR spectra are shown in Figure 5.8. In $Cr[Cr(CN)_6]$, the cyanide stretching peak, ν_{CN}, occurs at about 2200 cm^{-1}. For the potassium, rubidium, and cesium analogs, this peak consistently shifts to lower wavenumbers as the oxidation state decreases. For the absorption is at about 2100 cm^{-1}, and for $A_2Cr[Cr(CN)_6]$ it is at about 2000 cm^{-1}. The cyanide stretching frequency decreases with the oxidation state because the added electron density on the carbon-coordinated chromium ion increases the amount of π backbonding between the chromium atom and the cyanide ligand. In π backbonding, some of the carbon atom's electronic density moves into the σ bond with the chromium atom while some of the chromium atom's electronic density feeds into the π^* orbitals of the carbon and nitrogen atoms, weakening their bond [29]. The fact that the shift is constant at about 100 cm^{-1} per electron added is good evidence that both reduction events occur at the carbon-coordinated chromium atom, which moves from chromium(III) to chromium(II) to chromium(I).

The peak for $Na_2Cr[Cr(CN)_6]$ has slightly more complicated behavior. It has two peaks in the cyanide stretching region: one at about 2050 cm^{-1} and another at about 1900 cm^{-1}. It is possible that this is due to the fact that the sodiated compounds,

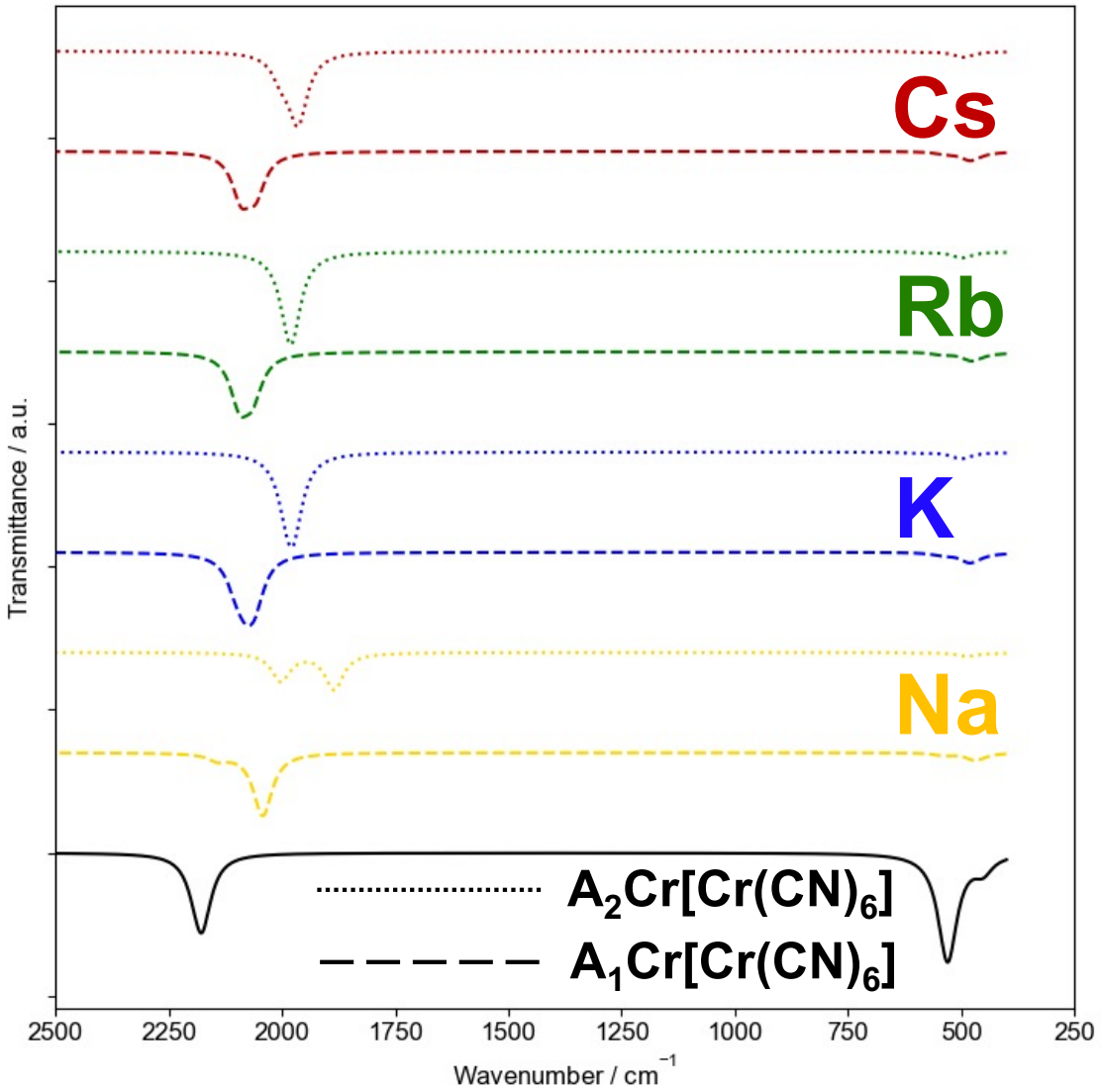

Figure 5.8: Simulated IR spectra. Data for the completely oxidized compound are shown in black. Data for the sodium, potassium, rubidium, and cesium analogs are shown in gold, blue, green, and dark red, respectively. Dashed and dotted lines correspond to 1 and 2 alkali ion(s) per formula unit, respectively.

uniquely, occupy the faces of the subcubes and have much smaller Na–C and Na–N distances than any of the other alkali-metal analogs.

This section details the theoretical electronic and magnetic properties of the $A_x\mathrm{Cr}[\mathrm{Cr}(\mathrm{CN})_6]$. In contrast to the physiochemistry and electrochemistry, the properties in this section vary much less between different alkali-metal analogs. Clear predictions are made for defect-free chromium hexacyanochromate that can be tested using techniques including SQUIDS magnetometry and IR spectroscopy.

5.5 Some comparisons to the defective analog

This final section introduces the simulation of a vacancy itself. This is only possible with the use of a supercell. Here a $2 \times 2 \times 2$ supercell is modeled in which one carbon-coordinated chromium and its six cyanide ligands have been removed. The simulated cell is $\mathrm{Cr}_8[\mathrm{Cr}(\mathrm{CN})_6]_7$, which is more conventionally written $\mathrm{Cr}[\mathrm{Cr}(\mathrm{CN})_6]_{\frac{7}{8}}$ or $\mathrm{Cr}[\mathrm{Cr}(\mathrm{CN})_6]_{0.875}$. The relaxed crystal structure is presented alongside the defect-free supercell for comparison, and differences between the simulated X-ray diffractograms are discussed. Finally, the effect of the defect on the compound's electronic structure is presented through analysis of the DOS and the real-space electronic charge density inside the vacancy.

5.5.1 Effect of vacancy on crystallography

The relaxed crystal structures are shown in Figure 5.9. The major difference introduced by the vacancy is an outward bulging of the six nitrogen-coordinated chromium ions away from the vacancy due to the absence of the cyanide ligand's negative charge density. The bulge changes the N–$\mathrm{Cr_N}$–N bond angle, distorting it from 180.0° to 170.6°. It also increases the $\mathrm{Cr_N}$–$\mathrm{Cr_N}$ distance through the vacancy to 10.50 Å from 10.41 Å. This value is the lattice parameter and it does not change when a vacancy is introduced, meaning the volumes are the same. However, since the mass

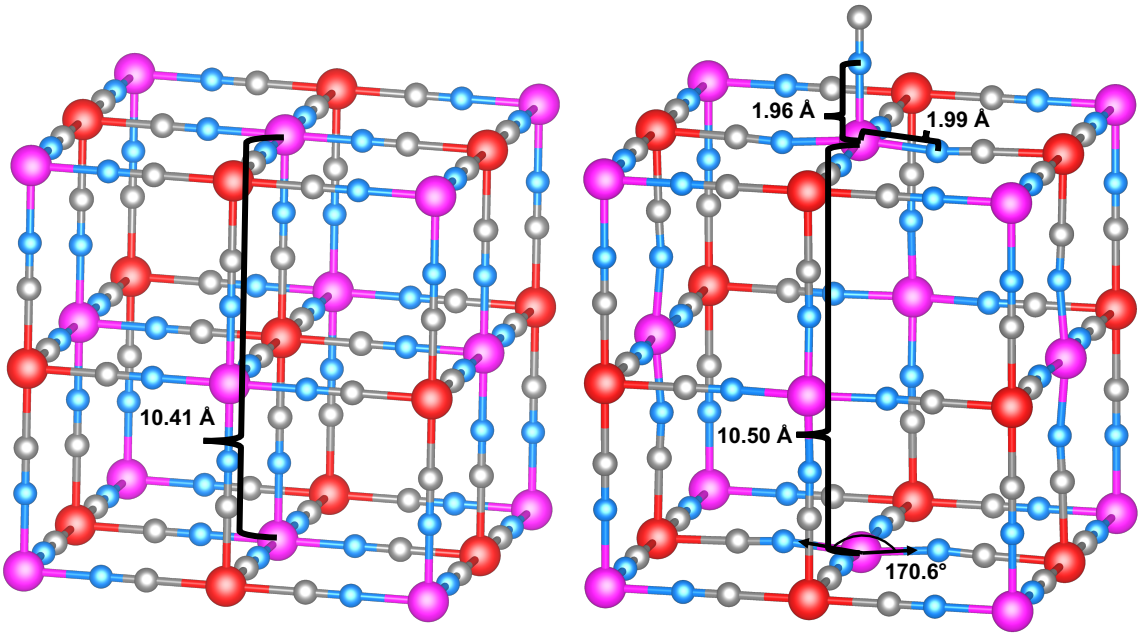

Figure 5.9: Crystal structure of a defective structure. The defect-free compound is shown at the left and the defective compound is shown at the right. The red, pink, gray, and blue atoms represent carbon-coordinated chromium, nitrogen-coordinated, carbon, and nitrogen, respectively. Certain distances and bond angles are marked in black

has decreased, the defective phase has a lower density. Finally, the five Cr_N–N bond lengths are not equal in the defective phase. The four coplanar nitrogen atoms are 1.99 Å away from the undercoordinated chromium ion, while the fifth nitrogen bond is contracted to 1.96 Å, a difference of 1.5%.

The simulated XRD patterns for the two phases are shown in Figure 5.10. The defect-free phase shows the class PBA peaks indicative of the $Fm\bar{3}m$, face-centered cubic crystal structure. The defective phase has a similar pattern. The main difference is the presence of three new peaks of low intensity between about 12 and 16° 2θ. The relative intensities of the peak from the (400) reflection (at about 34°) to the peak from the (420) peak (at about 39°) also change from greater than one to less than one.

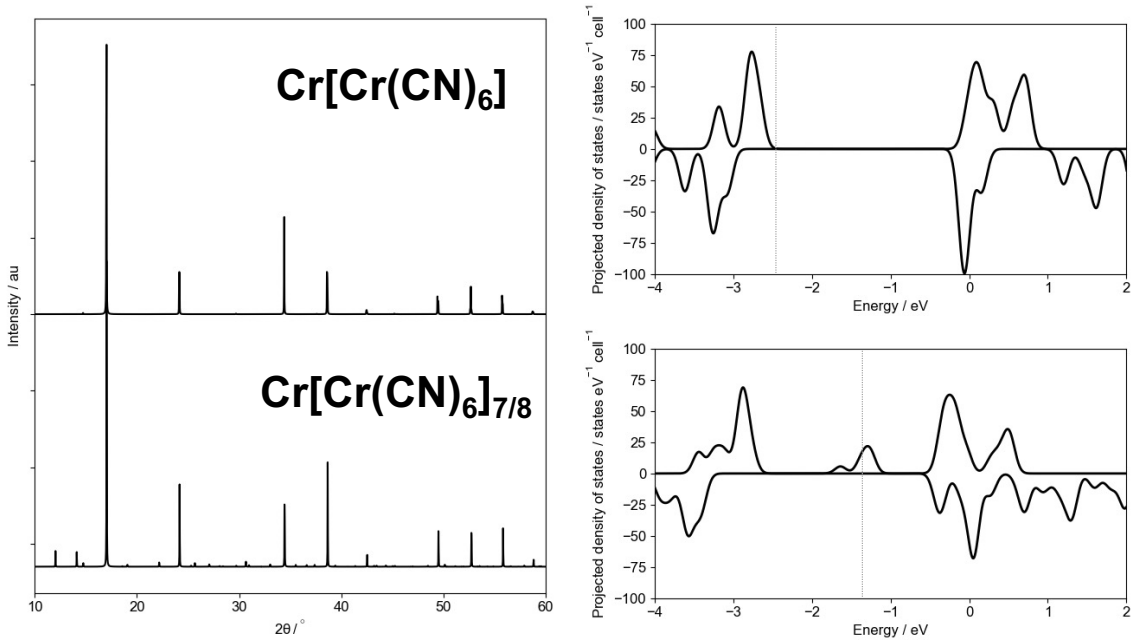

Figure 5.10: Simulated diffractogram and DOS of a defective structure. The plot at the left shows the XRD pattern for defect-free (upper) and defective (lower) compounds. The defect-free compound has the space group $Fm\overline{3}m$. The spin-polarized DOS are shown at the right for the same compounds. The Fermi level is marked by the dotted gray line.

5.5.2 Electronic structure of a defect

Figure 5.10 also shows the DOS for the two compounds. Compared to its effect on the crystal structure, the effect of a vacancy on the electronic compound is quite stark. While the defect-free compound exhibits an electronic band gap with a separation of about 2.5 eV between the valence- and conduction-band states (to reemphasize, these calculations are performed using DFT+U), introducing a vacancy opens states almost exactly in the middle of the band gap. In semiconductor physics, these kinds of states are called deep-level traps or deep traps [30], because they are located deep in the band gap and because it is easy for charge-carrying electrons or holes to become localized in these states and recombine. These states are partially occupied.

The states that form the deep trap are not completely degenerate. That is, there is one small peak at about -1.7 eV and another, larger, peak at about -1.3 eV. The existence of two peaks in the PDOS is reflected in the crystallography, in which the $\mathrm{Cr_N}$–N bond lengths are not all equal. Contraction of one bond length lowers the energy of one of the d_{xy}, d_{xz}, and d_{zy} orbitals and increases the energy of the other two. This is analogous to the change induced by the Jahn–Teller effect.

To understand these deep traps better, the orbitals that give rise to them are rendered in Figure 5.11. The charge density for these states is localized on the nitrogen-coordinated chromium ions. Moreover, the charge density is asymmetrically directed, in real space, toward the vacancy. The charge density around all six chromium ions is equivalent.

These interesting and peculiar changes to the electronic structure can be rationalized as follows. To maintain charge neutrality when one chromium atom and six atoms (each) of carbon and nitrogen are removed from $\mathrm{Cr^{III}_8[Cr^{III}(CN)_6]_8}$, three more electrons have to be accommodated by the ions that remain. (This can be thought of as the $\mathrm{[Cr^{III}(CN)_6]^{3-}}$ complex anion "giving back" its three electrons before being removed as a neutral species.) So those three electrons are highly localized within

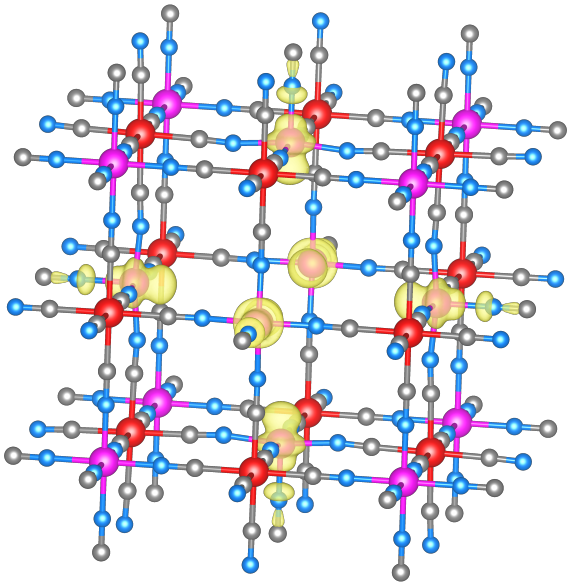

Figure 5.11: Band-decomposed charge density inside a vacancy. The crystal structure of $Cr[Cr(CN)_6]_{0.875}$ is rendered with carbon-coordinated ions in red and nitrogen-coordinated ions in pink. Carbon and nitrogen atoms are light blue and gray, respectively. The vacancy is at the center. The electronic-charge-density isosurface, composed of the bands around the Fermi energy in Figure 5.10, is in yellow. The d orbitals from the undercoordinated chromium ions are directed into the cavity.

the cavity, but they are highly delocalized among the six d orbitals of the undercoordinated chromium ions.

Vacancies are an important and much-studied feature of PBAs. This work modeling $Cr[Cr(CN)_6]_{0.875}$ is the first description, to my knowledge, of how the excess charge is accommodated in PBAs with vacancy defects. Furthermore, this is the first suggestion that deep traps can be engineered into PBAs by controlling their vacancy content.

5.6 Conclusions

In this chapter, the properties of the chromium hexacyanochromate system are predicted from first-principles DFT+U modeling. First, the Hubbard U parameters for the system are parameterized based on the unit-cell volumes and reduction potentials of the $K_xCr[Cr(CN)_6]$ system as calculated using a hybrid functional. Adapting

those U values to three other alkali-metal analogs, important materials properties are calculated.

In terms of the analogs' physio- and electrochemistry, the unit-cell volumes are shown to decrease with decreasing oxidation state for all analogs. Reduction potentials are calculated to be in the range of about -1.6 to -0.6 V versus the SHE, showing that the PBA can insert two alkali ions at low potentials. The potential increases along the series sodium, potassium, rubidium, cesium. The MEPs for the ions' movement through the lattice are shown and the activation energy calculated, ranging from 0.14 eV in fast-moving sodium to 1.83 eV for immobile cesium. The polaronic character of potassium transport is discussed.

Electronic and magnetic properties are calculated, too. These vary less as a function of the inserting ion because the crystal is so ionic, but they are strongly a function of oxidation state. First, it is confirmed that the fully reduced material is charge-disproportionated $A_2\mathrm{Cr^{III}[Cr^{I}(CN)_6]}$, and not chromium(II)-chromium(II). The fully oxidized compound is antiferromagnetic while the more reduced phases are both ferrimagnetic. The antiferromagnetic phase has a direct magnetic exchange-coupling coefficient, J_1, of -22 meV. And in the simulated IR spectrum, the cyanide stretching mode absorbs at about 2200, 2100, and 2000 $\mathrm{cm^{-1}}$ with 0, 1, and 2 inserting ions, respectively.

Finally, the effect of a defect on the crystal and electronic structure is simulated. Behaving like a positively charged particle, the vacancy causes the six surrounding nitrogen-coordinated chromium ions to bulge outward. Those ions' d orbitals extend into the cavity in which three excess electrons are accommodated. This gives rise to deep traps in the compound's electronic structure.

These data suggest strongly that synthesis of a defect-free chromium hexacyanochromate still eludes the community. A second reduction event at the carbon-coordinated chromium is thermodynamically possible for specific capacities of 175, 159, 125, and

102 mA h g^{-1} for the sodium, potassium, rubidium, and cesium analogs, respectively. The ground-state magnetization for the unit cell is exactly 0, implying antiferromagnetic chromium-chromium alignment and zero saturation magnetization.

The most important future work suggested by this study is experimental validation of the predictions by synthesizing the defect-free compound. There are substantial synthetic challenges to this effort that our laboratory is working on now (see [31]).

Probably the most promising computational follow-on work is to explore the structure of vacancies in greater depth and in other PBAs. This will require careful determination of Hubbard U values for other compositions, following the parameterization procedure used here. But engineering water-filled vacancies is particularly important for catalyzing the hydrogen-evolution reaction [32], and experimental study of long-range defect ordering is a fruitful contemporary subfield of research [33].

This work is the most comprehensive theoretical study of the chromium hexacyanochromate PBA to date. It is an important contribution to the design of anode materials for the next generation of electrochemical energy storage.

Computational details

I performed all DFT calculations using the Vienna ab initio Simulation Package (VASP) [34, 35]. A planewave kinetic-energy cutoff of 520 eV was used throughout, and criteria for electronic and ionic convergence were 10^{-5} eV and 0.05 eV $Å^{-1}$, respectively. Simulations of a single formula unit used a Γ-centered $4 \times 4 \times 4$ **k**-point grid, while $2 \times 2 \times 2$ real-space supercells were Γ-point only. Full geometric relaxation with unconstrained total magnetic moments was performed on all materials using the generalized-gradient approximation and the Perdew–Burke–Ernzerhof (PBE) functional [36] with Hubbard U parameters of $U_{\mathrm{Cr_C}} = 2.0$ eV and $U_{\mathrm{Cr_N}} = 0.5$ eV. The HSE-level calculations on $K_xCr[Cr(CN)_6]$ were done with the non-local, hybrid Heyd–Scuseria–Ernzerhof (HSE06) functional [37, 38]. I used the standard screening

parameter of 0.2 $Å^{-1}$ and a mixing of 25% Fock exchange with 75% PBE exchange. The NEB calculations for the ion-hopping activation energies used a spring constant of 5 eV $Å^{-2}$. The IR spectra were also plotted using a Lorentzian function with $\gamma = 25$ cm^{-1}.

References

[1] S. Wheeler, I. Capone, S. Day, C. Tang, and M. Pasta, "Low-potential prussian blue analogues for sodium-ion batteries: manganese hexacyanochromate," *Chemistry of Materials*, vol. 31, no. 7, pp. 2619–2626, 2019.

[2] J. Chen, C. Liu, Z. Yu, J. Qu, C. Wang, L. Lai, L. Wei, and Y. Chen, "High-energy-density aqueous sodium-ion batteries enabled by chromium hexacycnochromate anodes," *Chemical Engineering Journal*, vol. 415, p. 129003, 2021.

[3] F. Scholz and A. Dostal, "The formal potentials of solid metal hexacyanometalates," *Angewandte Chemie International Edition in English*, vol. 34, no. 23-24, pp. 2685–2687, 1996.

[4] K. Nakamoto, R. Sakamoto, Y. Sawada, M. Ito, and S. Okada, "Over 2 V Aqueous Sodium-Ion Battery with Prussian Blue-Type Electrodes," *Small Methods*, vol. 3, no. 4, p. 1800220, 2019.

[5] M. Arai, M. Miyake, and M. Yamada, "Metal(II) hexacyanochromate(III) MCr (M = Co, Cu, Fe) coordination nanoparticles stabilized by alkyl surface coordination ligand: Downsizing effect on their crystal structure and magnetic properties," *Journal of Physical Chemistry C*, vol. 112, no. 6, pp. 1953–1962, 2008.

[6] T. Mallah, S. Thiébaut, M. Verdaguer, and P. Veillet, "High-T_C molecular-based magnets: Ferrimagnetic mixed-valence chromium(III)-chromium(II) cyanides with T_C at 240 and 190 Kelvin," *Science*, vol. 262, no. 5139, pp. 1554–1557, 1993.

[7] S. Ferlay, T. Mallah, R. Ouahès, P. Veillet, and M. Verdaguer, "A room-temperature organometallic magnet based on Prussian blue," *Nature*, vol. 378, no. 6558, pp. 701–703, 1995.

[8] "Electrochemically tunable magnetic phase transition in a high-T_C chromium cyanide thin film, author=Sato, O and Iyoda, T and Fujishima, A and Hashimoto, K, journal=Science, volume=271, number=5245, pages=49–51, year=1996, publisher=American Association for the Advancement of Science,"

[9] W. E. Buschmann, S. C. Paulson, C. M. Wynn, M. A. Girtu, A. J. Epstein, H. S. White, and J. S. Miller, "Reversed (Negative) Magnetization for Electrochemically Deposited High-T_C Thin Films of Chromium Hexacyanide Magnets," *Chemistry of Materials*, vol. 10, no. 5, pp. 1386–1395, 1998.

[10] B. Le Guennic, S. Borshch, and V. Robert, "Prussian blue analogue $CsFe[Cr(CN)_6]$ as a matrix for the Fe(II) spin-crossover," *Inorganic Chemistry*, vol. 46, no. 26, pp. 11106–11111, 2007.

[11] B. Himmetoglu, A. Floris, S. De Gironcoli, and M. Cococcioni, "Hubbard-corrected DFT energy functionals: The LDA+U description of correlated systems," *International Journal of Quantum Chemistry*, vol. 114, no. 1, pp. 14–49, 2014.

[12] C. D. Wessells, R. A. Huggins, and Y. Cui, "Copper hexacyanoferrate battery electrodes with long cycle life and high power," *Nature Communications*, vol. 2, no. 1, pp. 550–555, 2011.

[13] M. M. Thackeray, "Manganese oxides for lithium batteries," *Progress in Solid State Chemistry*, vol. 25, no. 1-2, pp. 1–71, 1997.

[14] C. Doerrer, I. Capone, S. Narayanan, J. Liu, C. R. Grovenor, M. Pasta, and P. S. Grant, "High Energy Density Single-Crystal NMC/Li6PS5Cl Cathodes for All-Solid-State Lithium-Metal Batteries," *ACS Applied Materials and Interfaces*, vol. 13, no. 31, pp. 37809–37815, 2021.

[15] M. Okubo, D. Asakura, Y. Mizuno, J. D. Kim, T. Mizokawa, T. Kudo, and I. Honma, "Switching redox-active sites by valence tautomerism in prussian blue analogues $A_xMn_y[Fe(CN)_6] \cdot nH2O$ (A: K, Rb): Robust frameworks for reversible Li storage," *Journal of Physical Chemistry Letters*, vol. 1, no. 14, pp. 2063–2071, 2010.

[16] W. M. Haynes, ed., *CRC Handbook of Chemistry and Physics*, pp. 5–80—5–89. CRC Press, 2014.

[17] C. D. Wessells, S. V. Peddada, M. T. McDowell, R. A. Huggins, and Y. Cui, "The Effect of Insertion Species on Nanostructured Open Framework Hexacyanoferrate Battery Electrodes," *Journal of The Electrochemical Society*, vol. 159, no. 2, p. A98, 2012.

[18] C. Ling, J. Chen, and F. Mizuno, "First-principles study of alkali and alkaline earth ion intercalation in iron hexacyanoferrate: The important role of ionic radius," *Journal of Physical Chemistry C*, vol. 117, no. 41, pp. 21158–21165, 2013.

[19] G. Henkelman, B. P. Uberuaga, and H. Jónsson, "Climbing image nudged elastic band method for finding saddle points and minimum energy paths," *Journal of Chemical Physics*, vol. 113, no. 22, pp. 9901–9904, 2000.

[20] D. Morgan, A. Van der Ven, and G. Ceder, "Li Conductivity in Li_xMPO_4 (M = Mn, Fe, Co, Ni) Olivine Materials," *Electrochemical and Solid-State Letters*, vol. 7, no. 2, pp. 30–33, 2004.

[21] M. Pasta, C. D. Wessells, R. A. Huggins, and Y. Cui, "A high-rate and long cycle life aqueous electrolyte battery for grid-scale energy storage," *Nature Communications*, vol. 3, no. May, p. 1149, 2012.

[22] T. Hosaka, T. Fukabori, H. Kojima, K. Kubota, and S. Komaba, "Effect of Particle Size and Anion Vacancy on Electrochemical Potassium Ion Insertion into Potassium Manganese Hexacyanoferrates," *ChemSusChem*, vol. 14, no. 4, pp. 1166–1175, 2021.

[23] N. W. Ashcroft and N. D. Mermin, *Solid State Physics*. Holt-Saunders, 1976.

[24] A. Van der Ven, Z. Deng, S. Banerjee, and S. P. Ong, "Rechargeable alkali-ion battery materials: theory and computation," *Chemical Reviews*, vol. 120, no. 14, pp. 6977–7019, 2020.

[25] M. T. Hutchings and E. Samuelsen, "Measurement of spin-wave dispersion in NiO by inelastic neutron scattering and its relation to magnetic properties," *Physical Review B*, vol. 6, no. 9, p. 3447, 1972.

[26] T. Kotani and M. van Schilfgaarde, "Spin wave dispersion based on the quasiparticle self-consistent GW method: NiO, MnO and α-MnAs," *Journal of Physics: Condensed Matter*, vol. 20, no. 29, p. 295214, 2008.

[27] S. Baroni, S. de Gironcoli, and A. Dal Corso, "Phonons and related crystal properties from density-functional perturbation theory," *Physics Letters, Section B: Nuclear, Elementary Particle and High-Energy Physics*, vol. 73, no. 2, pp. 515–562, 2001.

[28] P. Giannozzi and S. Baroni, "Vibrational and dielectric properties of C60 from density-functional perturbation theory," *The Journal of Chemical Physics*, vol. 100, no. 11, pp. 8537–8539, 1994.

[29] G. L. Miessler, P. J. Fischer, and D. A. Tarr, *Inorganic Chemistry*. Pearson, 2014.

[30] M. McCluskey and E. Haller, *Dopants and Defects in Semiconductors*. CRC Press, 2012.

[31] S. Wheeler, *Prussian blue analogue materials for energy storage applications*. PhD thesis, University of Oxford, 2020.

[32] H. Yang, J. Liu, Z. Chen, R. Wang, B. Fei, H. Liu, Y. Guo, and R. Wu, "Unconventional bi-vacancies activating inert Prussian blue analogues nanocubes for efficient hydrogen evolution," *Chemical Engineering Journal*, vol. 420, p. 127671, 2021.

[33] A. Simonov, T. De Baerdemaeker, H. L. Boström, M. L. R. Gómez, H. J. Gray, D. Chernyshov, A. Bosak, H.-B. Bürgi, and A. L. Goodwin, "Hidden diversity of vacancy networks in Prussian blue analogues," *Nature*, vol. 578, no. 7794, pp. 256–260, 2020.

[34] G. Kresse, J. Furthmüller, and J. Hafner, "Theory of the crystal structures of selenium and tellurium: The effect of generalized-gradient corrections to the local-density approximation," *Physical Review B*, vol. 50, no. 18, pp. 13181–13185, 1994.

[35] G. Kresse and J. Furthmüller, "Efficiency of ab-initio total energy calculations for metals and semiconductors using a plane-wave basis set," *Computational Materials Science*, vol. 6, no. 1, pp. 15–50, 1996.

[36] J. P. Perdew, K. Burke, and M. Ernzerhof, "Generalized Gradient Approximation Made Simple," *Physical Review Letters*, vol. 77, no. 18, pp. 3865–3868, 1996.

[37] J. Heyd, G. E. Scuseria, and M. Ernzerhof, "Hybrid functionals based on a screened Coulomb potential," *Journal of Chemical Physics*, vol. 118, no. 18, pp. 8207–8215, 2003.

[38] A. V. Krukau, O. A. Vydrov, A. F. Izmaylov, and G. E. Scuseria, "Influence of the exchange screening parameter on the performance of screened hybrid functionals," *The Journal of chemical physics*, vol. 125, no. 22, p. 224106, 2006.

Chapter 6

Conclusions and future work

6.1 Summary of key findings

This work has been motivated by the need for next-generation electrochemical energy storage and the opportunity that the PBAs have to serve as active materials in (especially) sodium- and potassium-ion batteries. DFT modeling has allowed for new insight into the electronic structure of the PBAs. Throughout, it has been demonstrated that **advanced methods based on spin-polarized DFT succeed in modeling the electronic structure and electrochemical properties of the PBAs**. This concluding chapter summarizes the key findings of this work from the study of the electron-transport properties of three metal-hexacyanoferrate cathodes; from the rationalization of the high specific capacity in sodium manganese hexacyanomanganate; and from the prediction of the properties of the defect-free alkali-metal chromium hexacyanochromates. Finally, three new and important projects are proposed that can follow on directly from this work. These are a study into the kinetics of potassium manganese hexacyanoferrate; the extension of DFT values into a statistical-mechanical study of magnetic-ordering temperature and vacancy ordering; and the detailed simulation of other spectra.

6.1.1 Modeling electron transport in three cathodes

Chapter 3 is motivated by the general lack of understanding around the charge-transport properties of the otherwise-intensely studied sodium-ion-cathode materials: manganese, iron, and cobalt hexacyanoferrate. There, I demonstrate that a hybrid functional reproduces experimentally observed spin configurations and geometric phase changes, while the local PBE functional fails badly. I identify a band gap in all nine compounds; the gaps range from 1.90 eV in $NaFe[Fe(CN)_6]$ up to 4.94 eV in $Na_2Mn[Fe(CN)_6]$. In most of the compounds the electronic band edges originate from carbon-coordinated-iron orbitals as shown by the projected densities of states. This suggests an experimental strategy to dope that ion to tune carrier conductivities. The effective masses are reported, for the first time in any PBA experimentally or computationally, and are found to be very heavy. This is consistent with the band-decomposed charge densities, which show that the charge density of the valence and conduction bands is highly localized on the lattice ion. This study is an important foundation for making electronic conductivity a tunable PBA material property.

6.1.2 Explaining why three sodium ions fit

Sodium manganese hexacyanomanganate, $Na_xMn[Mn(CN)_6]$, has a reversible specific capacity of 209 mA h g^{-1}, which is substantially higher than the theoretical specific capacity of 172 mA h g^{-1} expected for the insertion of two sodium ions per formula unit. In this chapter, I examine the hypothesis that that high capacity and the third voltage plateau arise from the insertion of a third sodium ion from a theoretical perspective. Using a hybrid functional, the formation energies of various oxidation states and magnetic phases of the $Na_xMn[Mn(CN)_6]$ system are calculated. From this, the convex hull of stable phases is constructed. The crystal structures of the modeled compounds are compared to synchrotron XRD data and found to be in ex-

cellent agreement. The compound $Na_3Mn[Mn(CN)_6]$ is, indeed, thermodynamically stable. Examining its electronic structure reveals that it contains manganese(I) (a relatively rare species) and the sodium ions occupy the interfacial position of the lattice subcubes. I also show that the phase of the fully oxidized $Mn[Mn(CN)_6]$ compound is charge disproportionated, containing manganese(II) and manganese(IV), as opposed to the perhaps more expected manganese(III)-manganese(III). I also examine crystalline water and observe that its presence increases the reduction potential of the system. The hydrated compounds have theoretical crystal structures and reduction potentials that closely match experiment. This work clarifies the charge-storage mechanism in a well-known but less-understood PBA.

6.1.3 Predicting properties in a perfect crystal

Chromium hexacyanochromate, $A_xCr[Cr(CN)_6]$, is of great interest as an anode because of its low reduction potential and as a magnet because the chromium ions align antiferromagnetically with a high ordering temperature. In both applications, vacancies need to be minimized, but the synthesis of the defect-free compound is challenging. Chapter 5 uses DFT+U to predict the properties of the defect-free material. I find that the two chromium ions have different Hubbard U values because they are in unique crystal fields, but the values are constant for the three oxidation states examined. Using those U values, I examined four alkali-metal analogs; their reduction potentials increase with ionic radius from -1.6 to -0.6 V versus the SHE. The kinetics are probed with the NEB method and the activation energies for ion movement through the lattice (as well as the MEP) are heavily dependent on the size of the ion, ranging from $E_a = 0.14$ eV for sodium to $E_a = 1.83$ eV for cesium. The atomic projection of the charges and the magnetic moments are reported, which reveal that both reduction events occur at the carbon-coordinated chromium, ultimately forming charge-disproportionated $A_2Cr^{III}[Cr^{I}(CN)_6]$. The fully oxidized $Cr[Cr(CN)_6]$ is con-

firmed to be antiferromagnetic with $J_1 = -22$ meV. The IR absorption frequencies are calculated. Finally, a vacancy itself is simulated and deep-level traps that arise in the electronic structure are noted. This work is by far the most in-depth computational investigation into this PBA system, and it makes predictions that will assist ongoing experimental efforts to synthesize the compound.

6.2 Future projects enabled by this work

6.2.1 Kinetics of potassium manganese hexacyanoferrate

Potassium manganese hexacyanoferrate is one of the most promising cathodes for potassium-ion batteries [1], but it is suspected that its performance is hampered, at least in part, by poor kinetics [2]. From this work, it is clear how to proceed with a careful theoretical consideration of the kinetics in $K_xMn[Fe(CN)_6]$. First, the material's Hubbard U values should be parameterized against HSE-level results or against operando XRD data. Then the formation and transport of polarons can be simulated. As seen in the case of chromium hexacyanochromate, in the movement of a polaron through the lattice, ionic and electronic transport are very closely tied. Ways of deconvoluting the two phenomena should be explored to explore different strategies like doping and vacancy engineering to improve transport. The opportunity to possibly separate the two effects—electronic and ionic—is one of the virtues of theory in this prospective study.

6.2.2 Statistical mechanics of vacancy ordering and magnetic-ordering temperature

As discussed in Chapter 5, the direct magnetic exchange-coupling constant calculated is a seed for other levels of theory to calculate materials properties like magnetic-ordering temperature. An interesting future work would be to engage with these statistical mechanics for chromium hexacyanochromate. The study can easily be ex-

panded to also consider the isoelectronic compounds $A\mathrm{V^{II}[Cr^{III}(CN)_6]}$, $A\mathrm{Cr^{III}[V^{II}(CN)_6]}$, and $A_2\mathrm{V^{II}[V^{II}(CN)_6]}$. Vanadium hexacyanochromate has been prepared and its ordering temperature is even higher than that of chromium hexacyanochromate [3]. The hexacyanovanadates are difficult to prepare, which is another reason to turn to theory. Magnetic ordering is just one kind of ordering about which a cluster-expansion Hamiltonian can be written and finite-temperature Monte Carlo simulations run. These are well reviewed in reference [4]. The thermodynamics of long-range vacancy ordering is an active area of research that would also benefit from this type of study [5].

6.2.3 Simulating more detailed spectra

From one perspective, this work has centered on accurately describing the electronic structure of the PBAs computationally. This allows for the simulation of a much wider variety of spectra than just the IR absorption simulated in Chapter 5. Simulation of ultraviolet-visible (UV-VIS) [6], nuclear magnetic resonance (NMR) [7], and electron-energy-loss spectroscopies (EELS) [8] are all possible with modern methods. Modeling the spectra will increase understanding of the PBAs' electronic structures.

References

[1] S. Dhir, S. Wheeler, I. Capone, and M. Pasta, "Outlook on K-Ion Batteries," *Chem*, vol. 6, no. 10, pp. 2442–2460, 2020.

[2] T. Hosaka, T. Fukabori, H. Kojima, K. Kubota, and S. Komaba, "Effect of Particle Size and Anion Vacancy on Electrochemical Potassium Ion Insertion into Potassium Manganese Hexacyanoferrates," *ChemSusChem*, vol. 14, no. 4, pp. 1166–1175, 2021.

[3] S. Ferlay, T. Mallah, R. Ouahès, P. Veillet, and M. Verdaguer, "A room-temperature organometallic magnet based on Prussian blue," *Nature*, vol. 378, no. 6558, pp. 701–703, 1995.

[4] A. Van der Ven, J. C. Thomas, B. Puchala, and A. R. Natarajan, "First-Principles Statistical Mechanics of Multicomponent Crystals," *Annual Review of Materials Research*, vol. 48, pp. 27–55, 2018.

[5] A. Simonov, T. De Baerdemaeker, H. L. Boström, M. L. R. Gómez, H. J. Gray, D. Chernyshov, A. Bosak, H.-B. Bürgi, and A. L. Goodwin, "Hidden diversity of vacancy networks in Prussian blue analogues," *Nature*, vol. 578, no. 7794, pp. 256–260, 2020.

[6] F. Giustino, *Materials modelling using Density Functional Theory: Properties and Predictions*. Oxford, England: Oxford University Press, 2014.

[7] J. R. Yates, S. E. Dobbins, C. J. Pickard, F. Mauri, P. Y. Ghi, and R. K. Harris, "A combined first principles computational and solid-state NMR study of a molecular crystal: flurbiprofen," *Physical Chemistry Chemical Physics*, vol. 7, no. 7, pp. 1402–1407, 2005.

[8] A. J. Morris, R. J. Nicholls, C. J. Pickard, and J. R. Yates, "OptaDOS: A tool for obtaining density of states, core-level and optical spectra from electronic structure codes," *Computer Physics Communications*, vol. 185, no. 5, pp. 1477–1485, 2014.